NTNU
Norwegian University of
Science and Technology

In-situ μ-CT of well cement exposed to CO_2-saturated water at high pressure and temperature

Ingrid Børve

Master of Science in Physics and Mathematics
Submission date: June 2018
Supervisor: Dag Werner Breiby, IFY
Co-supervisor: Malin Torsæter, SINTEF

Norwegian University of Science and Technology
Department of Physics

Summary

Large-scale implementation of carbon dioxide (CO_2) sequestration in depleted oil and gas reservoirs may potentially mitigate global climate change. However, successful CO_2 storage is contingent on a limited leakage through abandoned wells, which are commonly sealed with Portland cement. Thus, with the purpose of assessing depleted oil and gas reservoirs as sites for CO_2 sequestration, it is of interest to evaluate the degradation of Portland cement when subjected to CO_2 at reservoir conditions.

In this study, in-situ synchrotron micro computed tomography (μ-CT) images of Portland G cement exposed to CO_2-saturated water at high pressure and temperature have been analyzed with the aim of obtaining an enhanced understanding of the cement carbonation process. The cement sample had a through-going cavity that served as an idealized CO_2 leakage pathway during the μ-CT experiment, and alternating nonflow and constant flow conditions of CO_2-saturated water were applied. Automatic procedures have been developed to segment and further analyze the digital three-dimensional images. The results showed that in-situ μ-CT with synchrotron radiation is an experimental technique well-suited for gaining insight into the dynamics of cement carbonation.

The μ-CT images revealed processes occurring in the cement sample in the course of the experiment. Cement reaction zones were seen to develop near CO_2–cement interfaces, and the growth of the reacted cement was found to be faster for CO_2 flow compared to static conditions. Moreover, the results suggest that the growth of reacted cement slows down with time given constant CO_2 conditions. The images showed that crystals of calcium carbonate precipitated in the CO_2 leakage path during the first period of static CO_2 conditions. During time intervals of CO_2 flow, on the other hand, the crystals re-dissolved. The volumetric dissolution rate was approximately linear as function of time for constant CO_2 flow conditions, and it was found to increase when the CO_2 flow rate was raised. Furthermore, the measurements indicate that the cement sample experienced a slight expansion in the course of the experiment.

The obtained results seem promising for the integrity of CO_2 wells in the case of static CO_2 conditions, attributed to the slow cement carbonation and the cavity self-healing observed. However, the results suggest a relatively fast cement degradation and re-opening of cavities for cement exposed to CO_2 at a constant flow rate, which indicates that the sealing ability of wells may become compromised if well cement is exposed to a rapid CO_2 flow over time.

Sammendrag

Storskala lagring av karbondioksid (CO_2) i uttømte olje- og gassfelt kan potensielt redusere globale klimaendringer. Vellykket CO_2-lagring avhenger imidlertid av begrenset lekkasje av CO_2 gjennom forlatte olje- og gassbrønner. Slike brønner forsegles typisk med Portlandsement. Det er derfor av interesse å undersøke hvordan Portlandsement endres når den utsettes for CO_2 ved temperaturer og trykk tilsvarende det som finnes i et reservoar.

I denne oppgaven har tre-dimensjonale bilder fremskaffet ved bruk av in-situ mikro-computertomografi (μ-CT) med synkrotronstråling blitt analyserte. μ-CT-bildene viste en sementprøve av Portland G-sement utsatt for CO_2-mettet vann ved høy temperatur og høyt trykk. Sementprøven hadde et gjennomgående hulrom som fungerte som en idealisert lekkasjebane for CO_2, og løsningen med CO_2-mettet vann var vekselvis stillestående og strømmende med konstant hastighet. μ-CT-bildene har blitt segmenterte og analyserte ved hjelp av automatiske rutiner. Resultatene bekrefter at in-situ μ-CT med bruk av synkrotronstråling er en eksperimentell teknikk som er velegnet for å studere reaksjoner mellom sement og CO_2.

Analysen av μ-CT-bildene viser at reaksjonssoner ble dannet i sementprøven nær kontaktflater mellom sement og CO_2, og at reaksjonssonene vokste raskere når CO_2 strømte gjennom sementen enn under statiske forhold. Resultatene innebærer også at volumøkningen av reagert sement ble redusert med tiden gitt konstante strømningsforhold. Videre ble det avdekt at kalsiumkarbonat ble utfelt i lekkasjebanen i løpet av den første perioden med stillestående CO_2. I perioder hvor CO_2-mettet vann strømte gjennom lekkasjebanen, derimot, ble volumet av kalsiumkarbonat redusert. Ved konstante strømningsforhold var volumreduksjonen som funksjon av tid tilnærmet lineær. Krystallene ble hurtigere oppløst ved økt strømningsrate. Videre indikerer analysen at sementprøven utvidet seg i løpet av eksperimentet.

Resultatene er lovende for integriteten til brønner som utsettes for stillestående CO_2, men de antyder at forseglingsevnen til CO_2-brønner kan svekkes dersom Portlandsement utsettes for høye strømningsrater over tid.

Preface

This thesis is submitted as the conclusion of a five year master's degree program in Applied physics and Mathematics at the Norwegian University of Science and Technology (NTNU). The work presented has been conducted in collaboration with SINTEF Industry, as part of the project *Closing the gaps in CO_2 well plugging*, which is funded by the Research Council of Norway and has grant number 243765.

In this project, in-situ micro computed tomography (μ-CT) images have been analyzed with the aim of investigating the effect of CO_2 on well cement. The μ-CT experiment was carried out at the European Synchrotron Radiation Facility (ESRF) in May 2017 as a collaboration between researchers at the following institutions: Norwegian University of Science and Technology (NTNU), Stiftelsen for industriell og teknisk forskning (SINTEF), ESRF, Université de Maine and University of Copenhagen. Those involved were Elvia A. Chavez Panduro, Leander Michels and Dag W. Breiby at NTNU, Malin Torsæter at SINTEF, Benoit Cordennier and Elodie Boller at ESRF, Alain Gibaud and Landry Ouanssi at Université de Maine, and Melania Rogowska and Henning Osholm Srensen at the University of Copenhagen.

I would like to thank my supervisor Dag W. Breiby at the Department of Physics (NTNU) for excellent guidance and thorough feedback, and my co-supervisor Malin Torsæter at SINTEF Industry for her truly valuable advice and support. Moreover, I am very grateful for the help I have received from Elvia A. Chavez Panduro at the Department of Physics (NTNU) to better understand the experiment and the results. I would also like to thank Alain Gibaud at Université de Maine and Kamila Gawel at SINTEF Industry for sharing their knowledge and expertise with me. Furthermore, I am grateful to those who performed the μ-CT experiment for letting me work on the obtained images.

Last but not least, I would like to thank my friends and family. In particular, I appreciate the encouragement I have received from my boyfriend Sigurd, the support from my parents, and all the meals and evenings shared with my flatmates Solveig, Ingrid and Anine this past year.

Trondheim, 18.06.2018

Ingrid Børve

Table of Contents

Abbreviations

am-SiO_2	=	Amorphous silica
C_3A	=	Tricalcium aluminate
$CaCO_3$	=	Calcium carbonate
C_4AF	=	Calcium aluminate ferrite
$Ca(OH)_2$	=	Portlandite
CCS	=	Carbon dioxide Capture and Storage
CO_2	=	Carbon dioxide
C_3S	=	Calcium silicate oxide
C-S-H	=	Calcium-Silicate-Hydrate
EOR	=	Enhanced Oil Recovery
ESRF	=	European Synchrotron Radiation Facility
H_2CO_3	=	Carbonic acid
IPCC	=	International Panel on Climate Change
ROI	=	Region of interest
SEM	=	Scanning Electron Microscopy
μ-CT	=	Micro Computed Tomography
2D	=	Two-dimensional
3D	=	Three-dimensional

Chapter 1

Introduction

1.1 Background and motivation

Since the pre-industrial times, global anthropogenic CO_2 emissions have increased [1]. Geological sequestration is a possible mitigating measure against a continued elevation of the atmospheric CO_2 concentration [2], but the risk of CO_2 leakage has hindered a large-scale implementation. One of the most promising sites for geological CO_2 sequestration is, according to the International Panel for Climate Change (IPPC), depleted oil and gas reservoirs [2]. CO_2 may be injected into the reservoirs through man-made oil or gas wells, which consist of a steel casing cemented into rock. To deter CO_2 from migrating towards the surface, abandoned wells and CO_2 injection wells must be sealed. This is typically done using a series of Portland cement plugs [3].

The wells are considered a weak link in the system confining CO_2 in depleted oil or gas reservoirs [4–12]. Dissolved CO_2 is acidic and may dissolve solid compounds in the well cement and, consequently, increase the cement permeability [5, 13]. In particular, cavities within the cement and along cement–steel or cement–rock interfaces may potentially be critical for the well integrity as they can boost the presence of CO_2 in contact with cement and thus a fortified cement alteration [5, 10].

In recent experiments, reaction zones have been observed to form in well cement near cement–CO_2 contact surfaces, giving rise to a change in cement properties such as the permeability, porosity and strength [6, 9, 14, 15]. Three distinct reaction zones have been identified. One of them have, in fact, a permeability that is lower than that of unreacted cement [16, 17], and consequently, a moderate cement carbonation may be advantageous for the integrity of wells [5]. On the other hand, a rapid cement degradation seems to be unfortunate as it leaves the cement weakened [5].

Recent studies show ambiguous results as to how the aperture of fractures inside cement

or at cement–steel or cement–rock interfaces is altered due to the presence of CO_2 [3, 10, 13, 14, 18–20]. While Walsh et al. and Chavez Panduro et al., among others, observed fracture self-sealing [10, 14], Cao et al. and Wigand et al. measured fracture opening [3, 18]. According to Brunet et al., the CO_2 flow rate and the fracture aperture and length are factors decisive for the outcome [13]. Fracture self-sealing may be caused by precipitation of calcium carbonate, cement weakening near the fracture and/or cement swelling [10, 14, 19], whereas fracture opening may be caused by the dissolution of cement compounds and/or stress induced by crystal precipitation [3, 18].

Few field studies of CO_2 well integrity have been carried out [20]. Exceptions include a study conducted by Carey et al. of Portland cement retrieved from an enhanced oil recovery (EOR) reservoir at the SACROC unit in Texas [5], and a study by Crow et al. of a natural CO_2 reservoir in Dakota [21]. In both studies, the cement was altered due to the CO_2 exposure, but both Carey et al. and Crow et al. concluded that the sealing ability of the cement had not been significantly compromised.

To be able to assess the risk related to CO_2 sequestration in depleted oil and gas reservoirs, an enhanced understanding of the influence of CO_2 on Portland cement at reservoir conditions should be obtained. Previously, cement carbonation has been studied by experimental techniques such as scanning electron microscopy (SEM) [6, 9, 14, 17, 22] and micro computer tomography (μ-CT) [10, 23]. Moreover, Chavez Panduro et al. has conducted an *in-situ* μ-CT study using an X-ray transparent pressure-cell [14]. *In-situ* refers to that measurements are made while the sample is subjected to relevant conditions, including temperature and pressure. In-situ X-ray studies enable time-lapse imaging, and the size, shape and location of three-dimensional (3D) image objects may be tracked as a function of time. By applying *synchrotron radiation* instead of a conventional X-ray source, as was used in the aforementioned experiment by Chavez Panduro et al., the spatial and temporal resolution of the images become improved [24]. Thus, in-situ synchrotron μ-CT studies of cement exposed to CO_2 may allow for a detailed analysis of the process of cement carbonation at reservoir conditions.

1.2 Approach

In this work, in-situ μ-CT images of Portland G cement exposed to CO_2 at high pressure and temperature are analyzed. The images feature a cylindrical cement sample with a through-going cavity serving as a CO_2 leakage path. Alternating CO_2 nonflow and flow conditions were applied. In the course of the experiment, three dimensional images were obtained for approximately one hundred time points. The images were obtained using synchrotron radiation at the European Synchrotron Radiation Facility (ESRF) prior to the start of this master's project.

The main task of the work of this master's thesis has been to develop automated routines for 3D image processing, including image segmentation. Image segmentation permits for the quantification of image features of interest, and it has been performed with the aim of measuring how the cement is altered due to the CO_2 exposure. The large amount of

μ-CT data requires automatic image segmentation, as opposed to manual segmentation. The procedures are written in the *ImageJ Macro* scripting language.

Routines for image processing were developed with the aim of evaluating the following phenomena:

- Calcium carbonate ($CaCO_3$) precipitation in the CO_2 leakage path.
- The growth of cement reaction zones near cement–CO_2 interfaces.
- A possible mechanical deformation of the cement sample.

The image analysis revealed that the CO_2 flow conditions were decisive both for the growth of reacted cement and for the evolution of $CaCO_3$ in the leakage pathway.

1.3 Thesis structure

The thesis is organized as follows: In Chapter 2, theory related to the research topic is presented. In Chapter 3, details of the μ-CT experiment are given. Thereafter, in Chapter 4, the performed image processing is explained in detail. The results are presented in Chapter 5 and discussed in Chapter 6. Finally, concluding remarks are given in Chapter 7.

This master's thesis is a continuation of the author's specialization project (Ref. [25], unpublished), which was written during the fall of 2017. Since the theory relevant for this master's thesis and that relevant for the specialization project overlap, parts of Chapter 2 are based on Ref. [25]. This concerns Sections 2.1–2.4 and 2.6.2.

Chapter 2

Theory

2.1 CO_2 storage in depleted hydrocarbon reservoirs

The process of CO_2 Capture and Storage (CCS) consists of three stages: Capturing the CO_2 from a high-emission source, transporting it to a suitable storage site, and storing the CO_2 for a long period [2].

According to the Special Report on CO_2 Capture and Storage by the Intergovernmental Panel on Climate Change (IPCC), depleted oil and gas reservoirs are promising candidates for CO_2 storage sites [2]. There are several reasons for this. Firstly, the integrity of reservoirs has proven itself throughout millions of years without substantial leakage of hydrocarbons, and the common opinion is that the caprock formations have the ability to trap also CO_2 [26]. Secondly, the technologies and systems that exist because of the oil and gas industry may be employed for injecting and monitoring CO_2. A third argument is that enhanced oil recovery can be achieved through the injection of CO_2 into a reservoir, meaning that oil production can be improved through a reservoir transition to CO_2 storage.

A successful CO_2 storage in depleted oil and gas reservoirs is contingent on a limited leakage of CO_2 to the atmosphere. According to Scherer and co-workers, the wellbores is the component of the reservoir construction that impose the largest risk of CO_2 migration towards the surface [12]. Oil and gas wells consist of multiple concentric steel casings with decreasing diameter as a function of subsurface depth that are cemented into the surrounding rock. Abandoned wells are typically sealed by a series of Portland cement plugs to prevent an upwards migration of fluids [3]. A worry is that the properties of the cement may be altered if CO_2 is injected into the reservoir, and leakage pathways could form along the wellbore casing, within the cement, or at cement–rock interfaces [13]. Figure 2.1 illustrates schematically CO_2 that is trapped under caprock, located in a depleted oil reservoir that is attached to a well.

According to White et al. (2003), it is disputable which leakage rate of CO_2 from a reservoir that should be acceptable [27]. Based on studies by Hepple and Benson (2002), Dooley and Wise (2002) and Ha-Duong (2002), White et al. suggest that a CO_2 leakage rate of less than 0.1%/year should be the performance requirement.

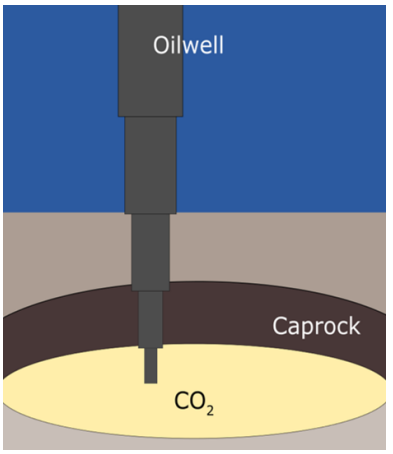

Figure 2.1: Schematic illustration of a CO_2 reservoir that is confined by caprock. An oilwell plugged with cement is connected to the reservoir. The illustration is based on figure 2.2 in the author's specialization project [25].

2.2 Properties of Portland cement and CO_2

2.2.1 Properties of Portland cement

Portland cement is made from materials containing calcium, silica, alumina, iron oxides and alkalis [4, 17]. The process of producing cement starts with pulverizing the raw materials and heating them to approximately 1450 °C forming Portland cement *clinker* [4]. Thereafter, the clinker is mixed with gypsum and ground into cement powder. Subsequently, the powder is combined with water to produce cement slurry. The slurry is commonly pumped into a well, where it goes through hardening, or *curing*, by the formation of hydration compounds [4, 28]. The result is a solid material whose main compounds are calcium-silicate-hydrates (C-S-H)[1], portlandite ($Ca(OH)_2$), and anhydrous grains [17, 29]. The compounds constituting anhydrous grains include calcium silicate oxide (abbreviated C_3S), calcium aluminate ferrite (abbreviated C_4AF) and tricalcium aluminate (abbreviated C_3A) [14]. C-S-H has an amorphous gel-like structure and constitutes about 70 wt % of Portland cement [17]. Portlandite and anhydrous grains, on the other hand, are crystalline [14]. In addition to the aforementioned compounds, also pore water and a small amount of other substances, such as ettringite, is present in Portland cement. Hardened Portland

[1] C-S-H is not a standard chemical formula, but commonly used in cement notation [17].

cement is a durable yet porous material. The pore water of Portland cement is basic, with a pH between 12.6 and 13.5 [30].

According to Lavrov and Torster, all well cement is heterogeneous to some degree [4]. Heterogeneities include pores, channels along cement surfaces and density and compositional gradients caused by gravity and so-called *wall effects*. Defects may form at several stages of the process of producing cement, including during cement mixing, when the cement slurry is pumped into a well, during cement hardening, or during the time that the cement resides in a well.

2.2.2 Properties of CO_2 at reservoir conditions

At subsurface conditions, CO_2 may be in a gaseous, liquid or supercritical state depending on the temperature and pressure. CO_2 becomes supercritical above the critical point which is at temperature $T = 31.1^\circ$ C and pressure $P = 7.38$ MPa [31]. As a supercritical fluid, CO_2 shares properties both with the gaseous and the liquid phases. Its density is similar to that of a liquid, yet it occupies a volume in the manner of a gas. The properties of a supercritical medium are advantageous for geological storage compared to those of a gas, as the supercritical fluid may be stored in a smaller volume due to its high density [32]. CO_2 will generally be a supercritical fluid at subsurface depths below 800 meters [32].

CO_2 is soluble both in water and in oil. When CO_2 dissolves in water, it reacts chemically to form carbonic acid (H_2CO_3). The solubility of CO_2 is about ten times greater in oil than in water [31]. At certain conditions, CO_2 and oil may be miscible. This is taken advantage of in Enhanced Oil Recovery (EOR) with injection of CO_2 gas, as the presence of CO_2 in a reservoir improves the flow of oil to the wells.

2.3 Geochemical model for the impact of CO_2 on Portland cement

When dissolved CO_2 is put in contact with Portland cement at reservoir conditions, a series of chemical reactions will occur. A model for the carbonation process was suggested by Kutchko et al. in 2007 and further modified by Mason et al. in 2013 [9, 17]. The reactions that occur are the same for non-flow of CO_2 as for flow conditions, but the propagation velocity of the reaction zone fronts will depend on the CO_2 flow rate. According to the proposed model, three distinct reaction zones form in the cement as time passes [17]. The zones are located parallel to the cement interface, as shown in figure 2.2. Zone 1 is the first to form and is called the *portlandite depleted zone*. Thereafter, zone 2, which is called the *fully carbonated zone*, develops, followed by zone 3. Zone 3 was first named the *porous silica zone* in the article by Kutchko et al., but later renamed by Mason et al. to the *porous zeolite zone* based on their experimental results [9, 17]. In this project, it will be referred

to simply as the *porous zone*. The three zone fronts propagate away from the cement–CO_2 interface with time.

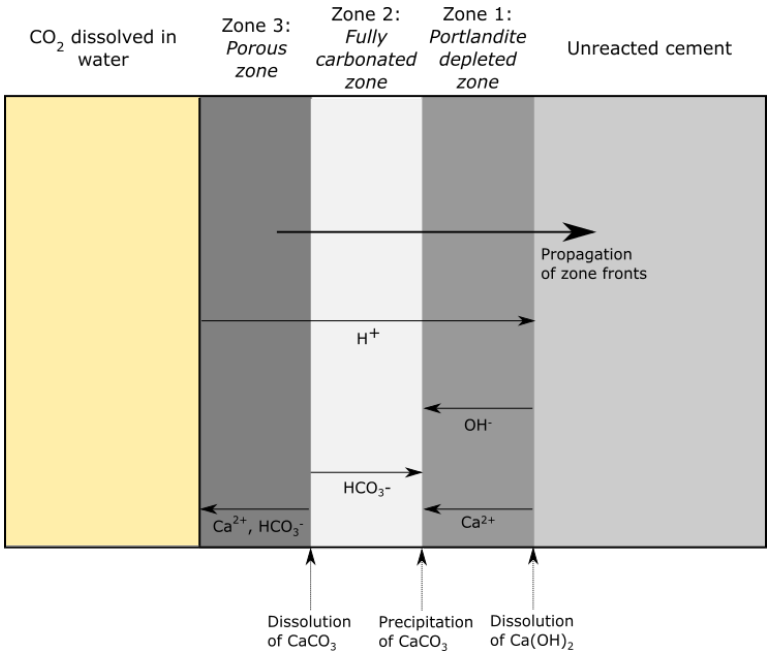

Figure 2.2: Dissolved CO_2 in contact with cement causes the creation of reaction zones: Zone 1 is the portlandite depleted zone, zone 2 is the fully carbonated zone, and zone 3 is the amorphous zone. The zone fronts propagate away from the cement–CO_2 interface with time, as indicated in the figure. At the front of zone 1, $Ca(OH)_2$ dissolves because the pH has been lowered from the diffusion or flow of CO_2 into the cement. The resulting aqueous OH^- and Ca^{2+} ions diffuse through zone 1, which is somewhat more porous than the unreacted cement. At the zone front of zone 2, $CaCO_3$ precipitates, giving rise to a region of lowered permeability. At the front of zone 3, the acidic environment causes re-dissolution of $CaCO_3$. The resulting zone is amorphous, weak and highly porous. The figure is based on figure 2.1 in the author's specialization project [25] and inspired by figure 3 in Ref. [17].

When CO_2 dissolves in water, carbonic acid forms leading to a lowering of the solution's pH. Kutchko et al. calculated the pH of a CO_2–brine mixture at 50 °C and 30.3 MPa, and found it to equal approximately 2.9 [17]. Consequently, the acidic solution will diffuse into the cement due to the pH and concentration gradients. In the case of non-flow CO_2 conditions, the diffusion rate controls the movement of dissolved CO_2 into the cement, but in the case of flow conditions, it may be determined by advection [7]. The concentrations of species CO_2, HCO_3^- and CO_3^{2-} in carbonic acid depend on the effluent pH [33].

When carbonic acid comes in contact with the cement, the pH in the cement pore water is lowered near the cement–CO_2 interface, leading to dissolution of portlandite ($Ca(OH)_2$) through the reaction

$$\mathrm{Ca(OH)_{2(aq)} \rightarrow Ca^{2+}_{(aq)} + 2OH^{-}_{(aq)}}, \tag{2.1}$$

which gives rise to the portlandite depleted zone. The porosity of this region is increased compared to that of unreacted cement, which boosts the presence of acidic water and hence the leaching of calcium ions [17]. The leached calcium ions diffuse towards the cement–CO_2 interface, whereas the net movement of carbonic acid is inwards in the cement. This, and the fact that the presence of hydroxide ions counteracts the pH lowering caused by the carbonic acid, permits for precipitation of calcium carbonate ($CaCO_3$) through the chemical reaction

$$\mathrm{Ca^{2+}_{(aq)} + HCO^{-}_{3(aq)} \rightarrow CaCO_{3(s)} + H_2O}, \tag{2.2}$$

and the fully carbonated zone forms between the portlandite depleted zone and the dissolved CO_2. The calcium carbonate precipitates both in the cement matrix and in fractures, if any. Consequently, cavities may be partially or completely sealed, a phenomenon that is known as self-sealing or self-healing [14]. The permeability of the fully carbonated zone is less than that of unreacted cement, and measurements by Kutchko et al. show that the hardness in units [HV/100 g] is more than doubled[2] [17]. According to Mason et al., also amorphous aluminosilicate precipitates in cavities, as a result of dissolution of C-S-H and calcium-aluminum-monosulfate at the propagation front of the fully carbonated zone [9]. In the experiment by Huerta et al. (2013) on the other hand, calcite and brownmillerite were identified in the region using micro X-ray diffraction [19]. Interexperimental variations in conditions and cement composition may be the cause of these discrepancies.

If portlandite becomes completely depleted in the fully carbonated zone, the pH of the pore water will decrease to below 11 due to the cease of renewal of hydroxide ions [17]. At this pH, calcium carbonates redissolve to form aqueous calcium bicarbonate through the reaction

$$\mathrm{CaCO_{3(s)} + H^{+}_{(aq)} \rightarrow Ca^{2+}_{(aq)} + HCO^{-}_{3(aq)}}, \tag{2.3}$$

which leads to an increased porosity of the cement in this region, and eventually the formation of a porous and weak amorphous zone [17]. In this manner, cavities that have previously sealed through the process of self-sealing may potentially re-open. Kutchko and co-workers propose that the amorphous state forms through the dissolution of C-S-H through the reaction

$$\mathrm{C\text{-}H\text{-}S_{(aq)} \rightarrow Ca^{2+}_{(aq)} + OH^{-}_{(aq)} + am\text{-}SiO_{2(s)}}, \tag{2.4}$$

where am-$SiO_{2(s)}$ is an abbreviation for amorphous silica gel [17]. In contrast, Mason et al. state that the porous zone is dominated by amorphous zeolite instead of amorphous

[2] HV refers to Vickers hardness values [17].

silicate [9]. According to Abdoulghafour et al., the formation of the porous zone may lead to a swelling of the cement in this region [34].

The growth of the reaction zones will, according to Kutchko et al., continue until the cement is completely degraded, as equilibrium can not be reached in the presence of a pH gradient [17]. Even so, the alteration of the cement may be limited if the growth rate is sufficiently small.

2.4 Computed tomography

The images that are analyzed in this project are obtained using X-ray μ-Computed Tomography (μ-CT). CT is an imaging technique that was invented in the 1970s [35], and the process of obtaining a CT image consists of two main steps: 1) Collecting X-ray projection images and 2) reconstructing the object from the projection images. In the first stage, X-rays are sent towards an object of interest. When the beam reaches the object, the photons interact with matter as described in section 2.4.1 below. The radiation that exits the object is recorded by detectors that are located in the projection plane, and a projection image is acquired. Thereafter, the object is rotated a small angle $\Delta\theta$, and a new projection image is recorded. The procedure is repeated until a predetermined number of projection images are obtained. The second step of X-ray imaging involves taking the projection images as input to algorithms for object reconstruction. CT makes it possible to gain knowledge about the interior of an object without destructing it. In this section, the physical principles behind X-ray imaging and the mathematical principles of image reconstruction are presented.

2.4.1 Interactions between X-rays and matter

Interactions between radiation and matter can be described by the complex refractive index n, defined as $n = 1 - \delta - i\beta$ with δ as the phase-shift term and β the extinction term [36]. The phase-shift term δ explains effects such as refraction, diffraction and interference, whereas the extinction term describes absorption of light and is therefore also called the absorption term [37].

The wavefunction ψ of photons propagating through matter in the z-direction is in the case of plane waves given by

$$\psi(z) = E_0 \mathrm{e}^{inkz} = E_0 \mathrm{e}^{i(1-\delta)kz} \mathrm{e}^{-\beta kz}, \tag{2.5}$$

where E_0 is the amplitude of the wave and nk is the wavenumber [36]. As the intensity of a wave is proportional to $|\psi|^2$, it is seen from equation 2.5 that the value of β is directly significant for the intensity of a wave.

X-rays interact with matter primarily via the photoelectric effect, the Compton effect and Rayleigh scattering [38]. The photoelectric effect implies that all of an incident photon's

energy is transferred to a bound electron, so that the electron, now entitled photoelectron, is released from its atom. In order for this to happen, the energy of the photon is required to be larger than or equal to the binding energy of the electron. The probability that photoelectric absorption occurs is nearly proportional to Z^3/E_γ^3, given that Z is the atomic number of the atom from which the photoelectron is released, and E_γ is the energy of the incident photon. Compton scattering, on the other hand, is inelastic scattering of an incident photon by a valence electron. The photon is deflected as a consequence of the interaction, and it has reduced energy compared to the incoming photon. Rayleigh scattering is, as opposed to Compton scattering, elastic scattering [38]. In Rayleigh scattering, the electric field of an incoming photon makes the electrons of an atom oscillate in phase and thus emit electromagnetic radiation. Rayleigh scattering occurs mainly for low-energy X-rays.

2.4.2 X-ray imaging

Conventional CT imaging makes use of absorption contrast [39]. When a photon beam traverses an object, it is attenuated due to interactions between photons and matter as described in section 2.4.1. Figure 2.3 illustrates a two-dimensional object, an X-ra source and a detector that are located in an (x, y)-coordinate system. Assume that a photon beam of intensity I is sent in the y-direction from the source towards the object. It enters the object at location A and exits it at B. When the beam travels a distance dy from A, the intensity is reduced by an amount dI that is proportional to I:

$$dI = -\mu(x, y)Idy, \tag{2.6}$$

where $\mu(x, y)$ is a position dependent quantity known as the linear attenuation function of the material [40].

If the initial intensity of the beam is denoted by I_0, it follows from integration of equation 2.6 that the beam that exits the object is of intensity

$$I(x) = I_0 e^{-\int_A^B \mu(x,y)dy}. \tag{2.7}$$

This is known as Beer's law [41]. The projection function $p(x)$ is obtained from equation 2.7 and defined as

$$p(x) = -\ln \frac{I(x)}{I_0} = \int_A^B \mu(x, y)dy \tag{2.8}$$

[40]. When parallel beams are sent towards the object in the y-direction, $p(x)$ is determined for a range of x.

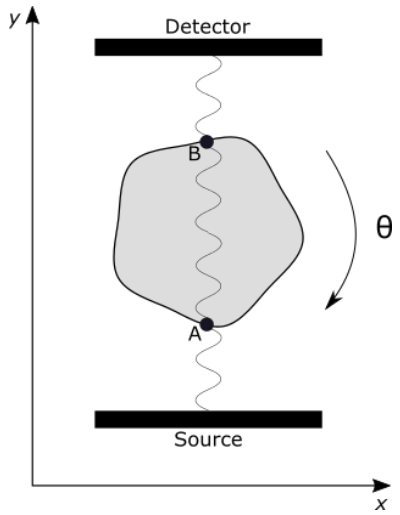

Figure 2.3: Schematic illustration of the setup for CT measurements. X-rays propagate from the source towards the object of interest. They reach the object at point A, and between points A and B, the beam is attenuated due to interactions with matter. The degree of attenuation depends on the properties of the object at each spatial location and the energy of the beam. The rays leave the object at point B and propagate towards the detector, where the intensity is measured. The illustration is taken from the author's specialization project [25].

2.4.3 Image reconstruction

Image reconstruction may be accomplished through analytical or iterative methods [42]. For commercial CT scanners, a branch of analytical methods known as *filtered backprojection* is commonly used [42]. Filtered backprojection has also been used on the data set analyzed in this project, and it is therefore at the focus of this section. Parallel beam projection data is assumed. In the case of fan or cone beam data, corrections must be made.

To be able to reconstruct the image of an object using CT, projections of the object from numerous angles are needed. During CT imaging, the object of interest is rotated, and it is therefore convenient to introduce a set of axes that are rotated an angle θ relative to the x- and y-axes. A rotated coordinate system with axes ξ and η may be expressed as

$$\xi = x\cos\theta + y\sin\theta \tag{2.9}$$

$$\eta = -x\sin\theta + y\cos\theta. \tag{2.10}$$

by a conventional rotation operation [43]. The projection function is written as $p_\theta(\xi)$ from hereon, as it depends on both ξ and θ. Figure 2.4 illustrates qualitatively the projection

function for a given object and direction of radiation. The purpose of CT imaging is to obtain information about the linear attenuation function $\mu(x, y)$ of an object of interest, and, as seen from equation 2.8, a projection image contains information about this quantity. For filtered backprojection methods, the relevant information is extracted through application of the Fourier Slice Theorem [44]. In the following, the theorem is derived in a rotated coordinate system (ξ, η).

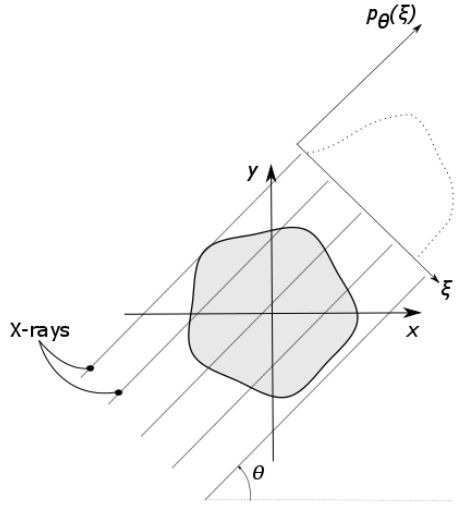

Figure 2.4: An object is exposed to X-rays that propagate in direction θ relative to the x-axis. The projection function $p_\theta(\xi)$ reflects how the intensity of the original beam is attenuated by the object in this specific direction. The figure is taken from the author's specialization project [25].

The Fourier transform of the projection function $p_\theta(\xi)$ is given by

$$\mathscr{F}\{p_\theta(\xi)\} = \int_{-\infty}^{\infty} p_\theta(\xi) e^{-2\pi i \xi k_\xi} d\xi \equiv P_\theta(k_\xi). \tag{2.11}$$

k_ξ is the Fourier space conjugate variable of ξ. Moreover, the two-dimensional Fourier transform of the linear attenuation function $\mu(\xi, \eta)$ is given by

$$\mathscr{F}\{\mu_\theta(\xi, \eta)\} = \int_{-\infty}^{\infty}\int_{-\infty}^{\infty} \mu_\theta(\xi, \eta) e^{-2\pi i(\xi k_\xi + \eta k_\eta)} d\xi d\eta \equiv M_\theta(k_\xi, k_\eta). \tag{2.12}$$

When the integral in equation 2.12 is evaluated at $k_\eta = 0$, it becomes

$$\mathscr{F}\{\mu_\theta(\xi, \eta)\}_{k_\eta=0} = \int_{-\infty}^{\infty}\left[\int_{-\infty}^{\infty} \mu_\theta(\xi, \eta) d\eta\right] e^{-2\pi i \xi k_\xi} d\xi = M_\theta(k_\xi, 0), \tag{2.13}$$

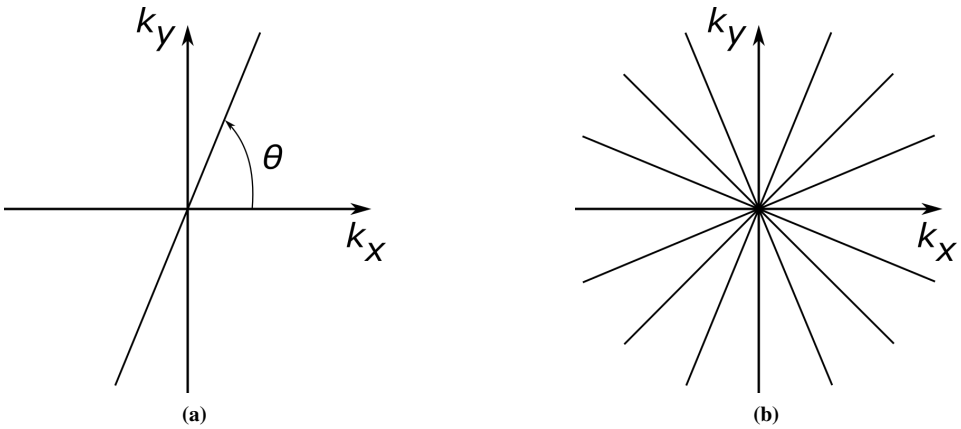

Figure 2.5: Lines $M_\theta(k_\xi, 0)$ displayed in the (k_x, k_y) coordinate system. (a) The line displayed makes an angle θ with axis k_x in the (k_x, k_y) coordinate system. In the coordinate system (k_ξ, k_η) on the other hand, which is rotated an angle θ relative to (k_x, k_y), this line would be horizontal. (b) A set of lines $M_\theta(k_\xi, 0)$ displayed in the (k_x, k_y) coordinate system. Each line corresponds to a unique rotation angle θ. In the (k_ξ, k_η) coordinate system, all of the lines would be horizontal. The figures are taken from the author's specialization project [25].

which by inspection equals $P_\theta(k_\xi)$ as defined in equation 2.11. This equality is known as the Fourier Slice Theorem. It implies that in k-space, the projection function $P_\theta(k_\xi)$ is identical to the line of $M_\theta(k_\xi, k_\eta)$ for which $k_\eta = 0$. In other words, one may determine $M_\theta(k_\xi, 0)$ by measuring $p_\theta(\xi)$ and finding its Fourier transform. Once $M_\theta(k_\xi, 0)$ is found for a large set of angles θ, an inverse rotational transformation followed by an inverse Fourier transformation will give a representation of $\mu(x, y)$. The inverse rotational transformation involves that for all θ for which measurements are done, the line $M_\theta(k_\xi, 0)$ is presented in the coordinate system (k_x, k_y). Since the line is horizontal in the coordinate system (k_ξ, k_η), it forms an angle θ with the k_x-axis in the coordinate system (k_x, k_y), as illustrated in figure 2.5a. Figure 2.5b shows how a set of lines $M_\theta(k_\xi, 0)$ for different angles θ appear in the (k_x, k_y) coordinate system.

If the sampling distribution had been uniform in (k_x, k_y)-space, an inverse Fourier transform of $M(k_x, k_y)$ could have been applied directly to obtain $\mu(x, y)$. However, as indicated by figure 2.5b, the density of measurements decreases proportionally to the inverse of the radial distance from the origin. Therefore, the lower frequencies will be overrepresented when reconstructing $\mu(x, y)$, which leads to a blurry image. In the method of filtered backprojection, the problem is dealt with by applying a ramp filter so that the low frequency data points are weighted less than those of high frequency. The linear attenuation function may be expressed as

$$\mu(x,y) = \int_{-\infty}^{\infty}\int_{-\infty}^{\infty} P(k_x,k_y)e^{i2\pi(k_x x+k_y y)}dk_x dk_y, \tag{2.14}$$

due to the Fourier Slice Theorem. Rewriting the expression in equation 2.14 to polar coordinates with Fourier space radius ω and polar angle ϕ, it becomes, after some manipulation,

$$\mu(x,y) = \int_0^{\pi}\Big[\int_{-\infty}^{\infty} P(\omega,\phi)|\omega|e^{i2\pi\omega(x\cos\phi+y\sin\phi)}d\omega\Big]d\phi \tag{2.15}$$

[45]. Equation 2.15 represents both a filtering operation and a backprojection operation. The filtering operation is embodied in $|\omega|$, which can be considered to be a weighting function. $|\omega|$ may be replaced by other functions $H(\omega)$ in order to achieve desired filtering effects. For instance, high-frequency noise can be reduced by applying a ramp filter with a cut-off frequency ω_{max}.

2.4.4 Phase contrast imaging

As stated in 2.4.1, the complex refractive index n consists of both an absorption term β and a phase term δ. It is possible to achieve improved CT image contrast if absorption contrast is combined with phase contrast [36, 41]. This has been employed for the images analyzed in this work. Phase contrast imaging exploits that waves are refracted on the boundary between two media, causing the direction of propagation to be slightly altered [36]. The phenomenon is illustrated in figure 2.6. The angular deviation is proportional to the gradient of the refracted beam's phase, and a change in δ, which depends on the phase, may therefore be observed [36].

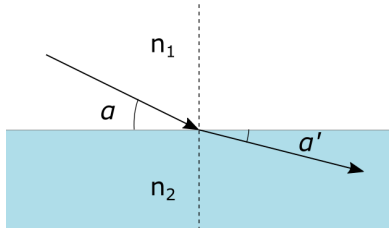

Figure 2.6: A ray is refracted at the interface between two media respectively of refractive indices n_1 and n_2, where $n_2 < n_1$. This leads to the angle α' between the outgoing beam's direction of propagation and the interface being smaller than the angle α between the incoming beam and the interface. The figure is based on figure 2.6 in the author's specialization project [25].

The phase of an X-ray wave cannot be observed directly [39]. Hence, methods are required to transform phase into measurable intensity variations. The method that has been used for the CT images analyzed in this work is in-line phase contrast, also called propagation-based phase contrast [39]. Figure 2.7 illustrates the principle of the method. Radiation

is sent towards an object of interest, and at the object edges, the rays are slightly bent due to refraction. This affects the intensity measurements, as indicated by the figure. In order to extract the phase from measured intensity variations, *phase retrieval* is required. Algorithms for phase-retrieval developed by Paganin and co-workers have been used in the process of reconstructing the CT images analyzed in this work [41].

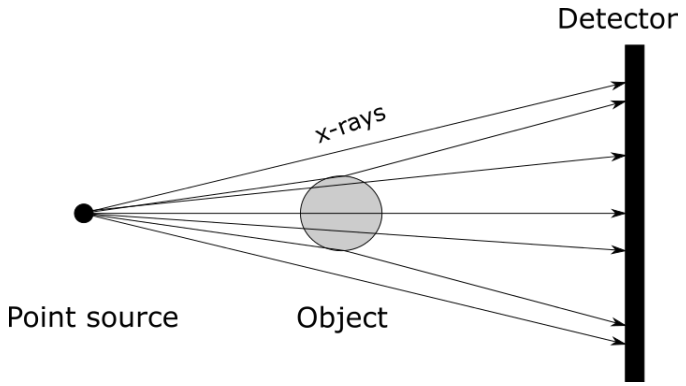

Figure 2.7: Schematic illustration of the principals of in-line phase contrast imaging. Rays are bent near the edges of the imaged object, affecting the measured intensity distribution. The figure is taken from the author's specialization project [25].

In-line phase contrast requires that the photon source delivers a beam of high spatial coherence [39]. Such a beam can be generated by a synchrotron. Furthermore, it is important that the distance between the object of interest and the detector is sufficiently long to permit the development of phase contrast. A combination of both absorption and phase contrast is achievable in the near-field regime.

2.5 Digital images

A gray-scale digital image is a two-dimensional (2D) or three-dimensional (3D) array of numerical values that determines the gray level intensity displayed at each spatial location of the image [46–48]. An array element is referred to as a *pixel* for 2D images and a *voxel* for 3D images[3], and a single integer is assigned to each pixel or voxel. The integers are in the range $[0, 2^8 - 1]$ for 8-bit images and in the range $[0, 2^{16} - 1]$ for 16-bit images. Commonly, the displayed brightness of a pixel increases with integer size, implying that integer value 0 is displayed in black and 255 is displayed in white for 8-bit images. For CT images, pixel or voxel integer values are calculated by designated image reconstruction algorithms based on the CT projection images, as described in section 2.4.3. The integers represent density values at distinct spatial locations of the imaged object. The image reconstruction algorithms typically create images in which the pixel/voxel values increase

[3]The word *pixel* originates from *picture element*, while *voxel* originates from *volume element*.

with increasing material density. Thus, vacuum is commonly represented by black color, and absorptive materials are represented by bright gray or white.

2.6 Image processing

Image processing is an umbrella term applicable to operations that modify or examine information incorporated in images [8]. According to Petrou and Petrou, image processing has four main purposes: image enhancement, image restoration, image compression and feature extraction [48]. Image enhancement implies that image characteristics, such as the contrast, are improved [48]. Image restoration, on the other hand, is performed to reverse damage that has been previously inflicted on an image. In other words, while the goal of image enhancement is to subjectively improve the image quality, that of image restoration is to replicate a known image. Methods used for image enhancement that have been applied in this project are presented in section 2.6.1. Image restoration has not been performed in this project, and is therefore not further dealt with. Going on, image compression is the process in which the number of bits used to store an image is reduced. Ideally, information should not be lost in this process. Lastly, feature extraction is performed to reduce the complexity of the image while retaining features of interest. The process in which pixels or voxels are grouped based on certain shared properties is referred to as *image segmentation* [46]. Image segmentation is typically performed to facilitate further image analysis. The topic is further dealt with in section 2.6.2.

2.6.1 Image enhancement

Image enhancement is applied with the aim of preparing images for further analysis or display [49]. This may be accomplished for instance by operations that reduce noise, improve the contrast, or highlight features of interest. In this section, methods applied in the work of this master's thesis are presented. The image displayed in figure 2.8 is used to illustrate several of the operations.

Noise reduction filters

The *mean filter*, the *median filter*, the *Gaussian blur filter* and the *Kuwahara filter* are typically used for noise reduction [51–53]. They take an input image and a sample window size $m \times n$ as input arguments, and return the transformed image. The size of the sample window, also called *kernel*, determines the degree of image blurring. In this section, 2D images are assumed, but the mathematical models are also applicable for 3D images. The input image will be represented by the function $I(x, y)$, and the output image by $\Theta(x, y)$. Figure 2.9 shows examples of how the mean, median, Gaussian and Kuwahara filters alter an input image.

(a) **(b)**

Figure 2.8: Image used for examples presented in this section. (a) The original image, included as a sample image in the Fiji package [50]. (b) The image after salt and pepper noise has been added.

The *mean filter* transforms an image by locally smoothing pixel intensities [51]. The sample window size specifies the size of the pixel neighborhood included in the smoothing operation. Mathematically, the mean filter can be defined as

$$\Theta(x,y) = \frac{1}{mn} \sum_{(\tilde{x},\tilde{y})\in S_{xy}} I(\tilde{x},\tilde{y}), \tag{2.16}$$

where S_{xy} is a region centered about (x, y) of size equal to that of the sample window $(m \times n)$ [51]. The mean filter can also be described as the convolution between the original image and an averaging kernel. Given a 3×3 window size, this may be expressed as

$$\Theta(x,y) = I(x,y) * \frac{1}{9}\begin{bmatrix} 1 & 1 & 1 \\ 1 & 1 & 1 \\ 1 & 1 & 1 \end{bmatrix}. \tag{2.17}$$

The *median filter* is similar to the mean filter, except that a pixel value is replaced by the *median* value of the pixel neighborhood, and not the mean. The median filter can be used to remove intensity outliers and to blur small image details [8]. Mathematically, the median filter can be described as

$$\Theta(x,y) = \text{median}_{(\tilde{x},\tilde{y})\in S_{xy}}\{I(\tilde{x},\tilde{y})\} \tag{2.18}$$

[51]. As in the case of the mean filter, S_{xy} is an area centered about (x, y) with size $(m \times n)$ determined by the choice of sample window.

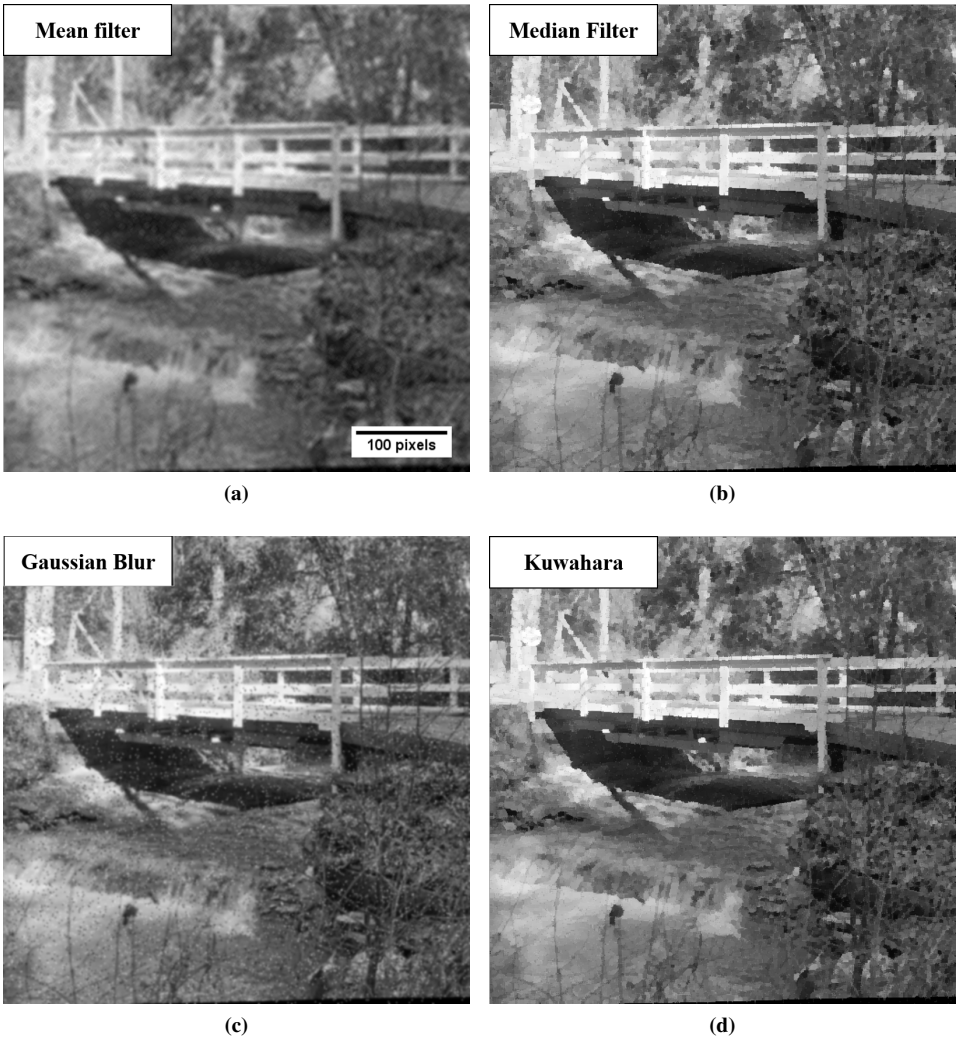

Figure 2.9: Examples of how an image with salt and pepper noise (figure 2.8b) is transformed by (a) the *mean* filter, (b) the *median* filter and (c) the Gaussian blur filter and (d) the *Kuwahara* filter. (a) Output image after the mean filter has been applied with a sample window 3×3. (c) Output image after the median filter has been applied with sample window 3×3. (d) Transformation by the Gaussian blur filter with sample window 3×3 and standard deviation $\sigma = 1$. (e) Result of the Kuwahara filter being applied to the image in 2.8b with sample window size 5×5.

The *Gaussian blur filter* transforms an image by convolving it with a Gaussian kernel, which is a discrete representation of the Gaussian function [53]. To illustrate, the transformation may be written as

$$\Theta(x,y) = I(x,y) * \frac{1}{16}\begin{bmatrix}1 & 2 & 1\\ 2 & 4 & 2\\ 1 & 2 & 1\end{bmatrix}, \tag{2.19}$$

given the kernel size 3×3 and a standard deviation $\sigma \simeq 0.8$.

The *Kuwahara filter* involves smoothing of already homogeneous regions [52]. Because of this, and the fact that the position of edges is maintained, the Kuwahara filter is known as an edge-preserving filter. Assume that a sample window of side lengths $2a + 1$ is chosen, where a is an integer[4]. The Kuwahara algorithm involves that for each pixel (x, y), the sample window region centered about (x, y) is divided into four quadratic sub-regions of side lengths $a + 1$ [54]. Figure 2.10 illustrates the four sub-regions. For each sub-region $i = \{1, 2, 3, 4\}$, the standard deviation $\sigma_i(x, y)$ of the pixel values is calculated, and the sub-region with the lowest standard deviation determines the new value of pixel (x, y). Pixel (x, y) is assigned the mean intensity value $m_i(x, y)$ of this sub-region.

Papari et al. expresses the image transformation mathematically as

$$\Theta(x,y) = \sum_i m_i(x,y) f_i(x,y), \tag{2.20}$$

where $\Theta(x, y)$ is the output, $m_i(x, y)$ is the mean value of the pixels in sub-region i, and $f_i(x, y)$ is defined as

$$f_i(x,y) = \begin{cases} 1, & \text{if } \sigma_i(x,y) = \min_k\{\sigma_k(x,y)\} \\ 0, & \text{otherwise.} \end{cases}$$

Unsharp masking

Unsharp masking is used to enhance the high frequency components of an image, making the image appear *sharper* [55]. Figure 2.11 shows an example of how unsharp masking transforms an image. The result is achieved by subtracting a blurred version of the image from the original image. The blurred image is commonly created by convolving a Gaussian kernel with the image. Equation 2.21 illustrates the mathematical operation of unsharp masking:

$$\Theta(x,y) = I(x,y) * \begin{bmatrix}0 & 0 & 0\\ 0 & 1 & 0\\ 0 & 0 & 0\end{bmatrix} - I(x,y) * \frac{1}{16}\begin{bmatrix}1 & 2 & 1\\ 2 & 4 & 2\\ 1 & 2 & 1\end{bmatrix}. \tag{2.21}$$

The function $I(x, y)$ represents the original image, whereas $\Theta(x, y)$ is the output image. When unsharp masking is applied to an image, the original image convolved with a Gaussian kernel is subtracted from the original image convolved with the identity kernel.

[4]The sample window side lengths should be odd for symmetry reasons.

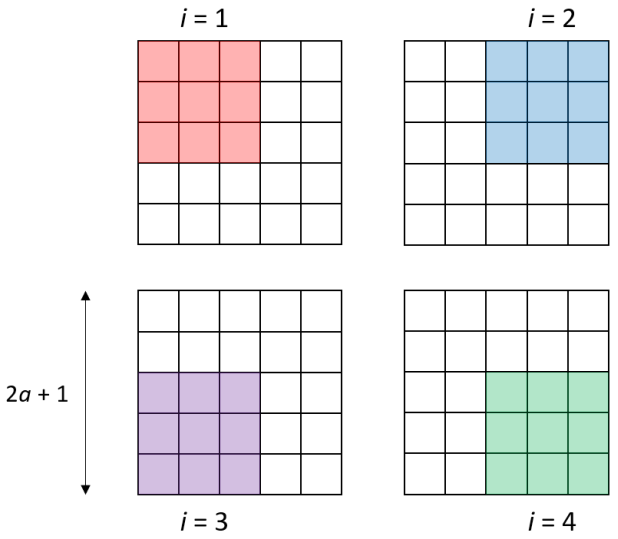

Figure 2.10: The division of the sample window into four partly overlapping sub-regions denoted by $i = \{1, 2, 3, 4\}$ as performed by the Kuwahara algorithm. Each sub-region is displayed in a unique color. $a = 2$ is used for this example. The smallest squares represent pixels, and the sample window is centered about the pixel (x, y). When the Kuwhara filter is carried out, the division of the sample window into sub-regions is performed for each pixel.

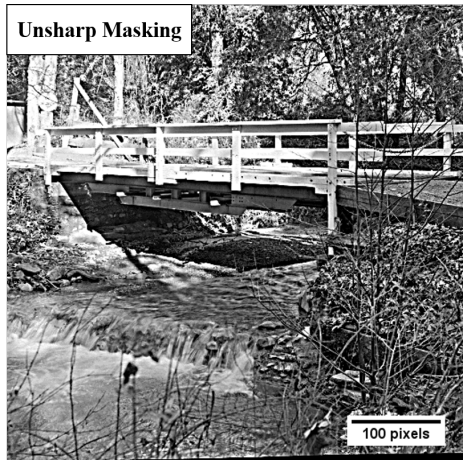

Figure 2.11: Image 2.8a after unsharp masking has been performed.

Subtract Background

Preparing images for analysis, it may be useful to normalize the image backgrounds [56]. In the *Fiji* software package, this is achieved using a rolling ball algorithm based on that

described by S. Sternberg in Ref. [56]. Imagine that the pixel values create a surface such that the brightest pixels are found on summits. When the rolling ball algorithm is applied, a ball of pre-selected radius is translated across the bottom side of the pixel-value surface. If the ball comes in contact with a pixel value, this pixel is assigned to the image background. In Fiji, there is an option to replace the ball with a sliding paraboloid. This may be advantageous if the size of image objects is small compared to the height of the peaks in the pixel-value surface. Figure 2.12 illustrates the effect of the subtract background algorithm.

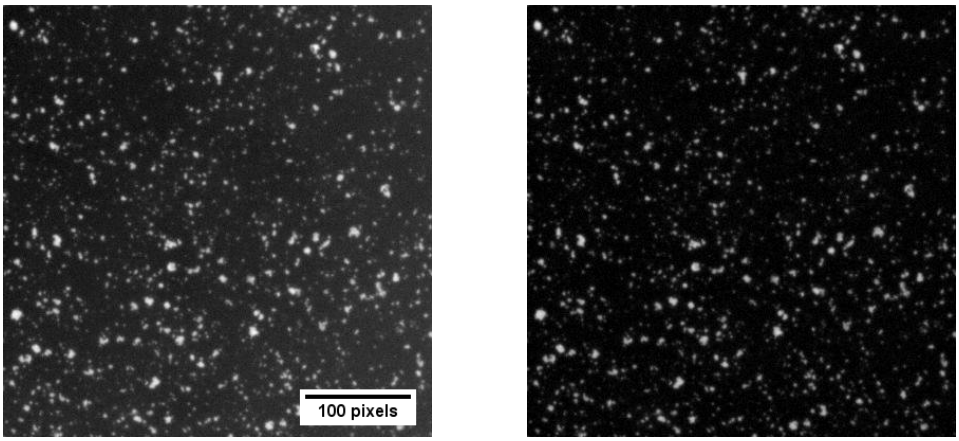

Figure 2.12: Example of how an image is transformed by the rolling ball algorithm for background normalization. (a) Original image included in the Fiji package [50]. (b) Transformed image obtained using rolling ball radius equal to 50 pixels.

Mathematical morphology

Mathematical morphology is a theory based on mathematical sets with applications in image processing [8, 57, 58]. Morphological operations are applied to images with the purpose of eliminating undesired features, while conserving the characteristics of the image objects [59]. The word *morphology* means the study of shapes, and in the case of mathematical morphology, mathematical sets constitute the shapes [8, 58]. A mathematical set is a finite or infinite group of objects [60], and in the field of image processing, a set consists of pixels or voxels [8]. For binary images, a set is composed of the pixels in the image foreground, which typically are white.

When a morphological operation is performed on an image, the image is combined with a *structuring element* [57]. A structuring element is an object of a given shape and size, the latter generally being smaller than that of the image object [8]. Commonly, structuring elements are chosen to be of a simple shape, such as a line, square, diamond or disk.

Examples of structuring elements are shown in figure 2.13. Each quadratic box represents a pixel, and the red spots mark which pixels that are chosen as *reference pixels*. During a morphological operation, the structuring element is introduced at all locations of the image. The reference pixel should in turn be placed at all of the image pixels before the operation is ended. The choice of operation decides how the image is transformed by the interaction with the structuring element.

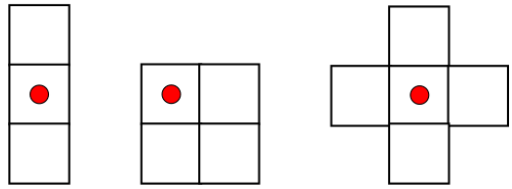

Figure 2.13: Examples of structuring elements (line, square and diamond). The quadratic boxes represent pixels, and the red spots indicate which pixels that are reference pixels. The figure is inspired by figure 6.4 in *Digital and Medical Image Processing* by T. Maintz [8].

The most basic morphological operations are *dilation* and *erosion* [59]. In the following, binary images are assumed. The dilation operator δ applied to a set X with structure element E is defined as

$$\delta_E(X) = \{x + e | x \in X \wedge e \in E\}, \tag{2.22}$$

where x and e are elements of respectively X and E [8]. Erosion is the dual operation of dilation, and the erosion operator ϵ is defined as

$$\epsilon_E(X) = \{x | \forall e \in E, x + e \in X\} \tag{2.23}$$

[8]. Dilation is also known as Minkowski addition, and erosion is known as Minkowski subtraction. Figure 2.14 illustrates the effect of dilation and erosion on an image using a diamond-shaped structuring element. The foreground color is white.

By modification or combination of dilation and erosion, other morphological operations may be defined [59]. *Morphological closing* and *morphological opening* are examples of operations that are made by sequentially combining erosion and dilation. Morphological closing is defined as dilation followed by erosion, and typically it is used to seal small holes and narrow cracks in the image object. Morphological opening, on the other hand, is defined as erosion followed by dilation. This operation can be used to smooth the surface of an image object and to remove islands of small size.

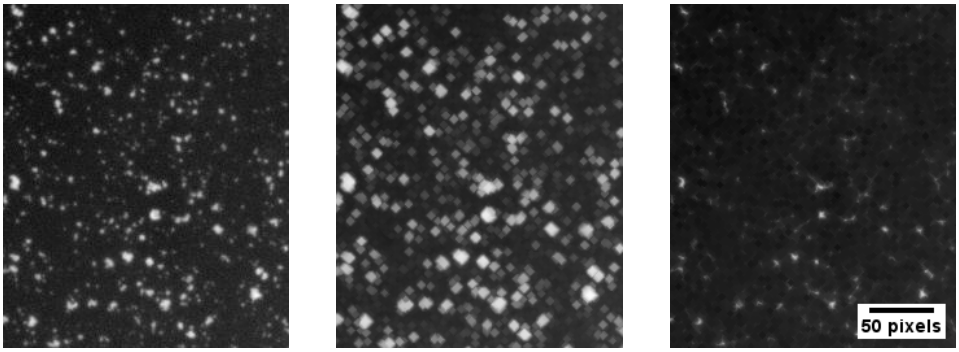

(a) (b) (c)

Figure 2.14: Examples of the transformation of (a) a test image included in the Fiji package [50] by morphological (b) dilation and (c) erosion. The morphological operations have been performed using a diamond-shaped structuring element of height and width 5 pixels with a centered reference pixel.

2.6.2 Image segmentation

Image segmentation is the process in which objects of interest are isolated through categorization of pixels or voxels into non-overlapping regions [46, 47]. A classical definition of image segmentation is that the set of all pixels or voxels, Λ, is subdivided into connected regions S_1, S_2, ..., S_n so that

$$\Lambda = \cup_{i=1}^{n} S_n \tag{2.24}$$

with

$$S_i \cap S_j = \phi, \quad i \neq j \tag{2.25}$$

[46, 61]. Furthermore, all pixels within a region must be of homogeneous character, distinct from the character of pixels in neighboring regions. Nikhil and Sankar Pal express this formally through a uniformity predicate $P(S)$ with properties $P(S_i) = True$ for all S_i, and P($S_i \cup S_j$) $= False$ for all adjacent regions S_i and S_j [61].

An extensive variety of methods exist for image segmentation. Pham et al. have divided the methods into the following categories: thresholding segmentation, region-growing segmentation, classifiers, clustering, Markov random field models, deformable models, atlas-guided approaches and trainable segmentation [46]. A short introduction to each method is given here, except for gray-level thresholding and region-growing segmentation which will be dealt with more thoroughly as they are made use of in this project.

- Classifier: A classifier algorithm segments an image based on training data that has been previously created through manual segmentation and labeling [46]. Classifier segmentation is referred to as a supervised technique.
- Clustering: Clustering methods perform segmentation by alternating between analyzing the image for shared properties that should define a class, and assigning pixels to each class [46, 62]. Clustering is known as an unsupervised technique.
- Markov random field (MRF) modeling: Image properties are modeled from detected correlations between pixels that are in the same spatial neighborhood [46, 61]. Based on the modeling, segmentation may be achieved.
- Deformable models: Deformable models are used to delineate the outline of objects by closed curves or surfaces [46]. This is achieved by first choosing a curve or surface confined by the selected object to be the starting point. Thereafter, the curve or surface is deformed by internal and external "forces" that are extracted from the image features with the aim that the curve or surface approaches the boundary between the object and its surroundings, and that it remains smooth.
- Atlas-guided methods: Atlas-guided methods require a pre-developed $atlas$, which is one or multiple images that contain information about the geometry and specific and relative location of all objects [63]. The image of interest is segmented by mapping its coordinates to those of the atlas.
- Trainable segmentation: Trainable segmentation makes use of artificial neural networks and hence mimic the knowledge humans apply when extracting objects from an image.

In addition to automated segmentation methods, *manual* segmentation techniques exist [46]. Manual segmentation methods require an operator to delineate objects of interest in images. Drawbacks of manual segmentation include that it may be very time-consuming, and that the person performing the segmentation may make errors.

The image displayed in figure 2.15 will be used for the examples in this section.

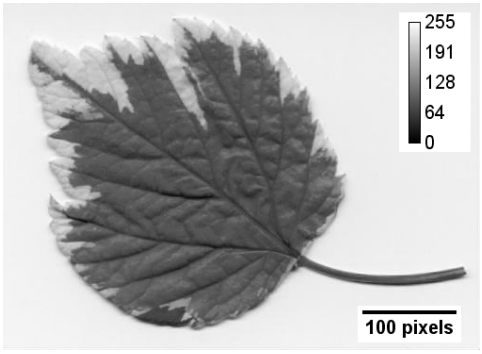

Figure 2.15: Example image used for examples. The image is part of the Fiji package [50].

Gray-level thresholding

Gray-level thresholding is a segmentation technique in which all image pixels with intensity values within a specified range are assigned to one group, and all remaining pixels are assigned to a second group. Subsequently, the resulting image is binary. Figure 2.16 shows two binary images obtained from the image displayed in figure 2.15 using intensity thresholds of respectively 130 and 228.

(a) **(b)**

Figure 2.16: Results of segmentation by gray-level thresholding applied on figure 2.15 with intensity thresholds (a) 130 and (b) 228.

Region-growing segmentation

Region-growing segmentation takes the spatial location of a pixel into account when assigning it to a group [48]. The pixels that are part of the same group are spatially connected and have attributes within a predefined range. In the following, an introduction is given to the two methods of region-growing segmentation that are applied as part of this master's project: single linkage region-growing and statistical region merging.

In *single linkage region-growing*, a pixel seed is manually chosen for each desired region. Thereafter, the algorithm adds neighboring pixels to the region if they fulfill the predetermined criteria. The criteria are generally related to intensity values and spatial intensity variation [62]. For instance, the difference in intensity between two neighboring pixels can determine whether or not the outer pixel is included in the region. A suitable choice of seed is crucial for the success of simple region-growing segmentation. Since the seed is chosen manually, a person must employ knowledge about the image at hand when making the decision. For a set of similar images, the same seeding choice may be employed if it is certain that the location of a seed is within the desired region for all images. The trial and error method may be useful to some extent when choosing a seed. Moreover, the region-growing method is sensitive to noise. For images with substantial noise, there might appear holes within a region [46].

In statistical region merging, regions are combined if a statistical test is passed [64]. The solver starts by assigning one unique segment to each pixel. Thereafter, the intensities of pixels are compared to the mean intensities of neighboring segments to decide whether the intensities are sufficiently similar for the segments to be merged[5]. Image 2.17 illustrates how an image is transformed by the statistical region-merging method. In the implementation included in the Fiji package, the user must select an estimate of the number of image segments before the algorithm is executed [50, 65].

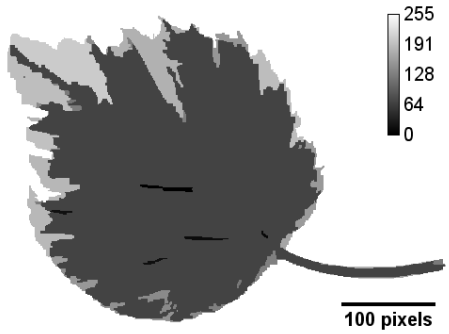

Figure 2.17: Image obtained by statistical region merging applied on image 2.15 with pre-selected number of regions equal to ten.

[5] See Ref. [64] for information about the statistical test applied.

Chapter 3

Experimental description

The images analyzed in this work were obtained in an in-situ μ-CT experiment carried out at the European Synchrotron Radiation Facility (ESRF) at the beamline ID19 using X-rays of energy $\sim$ 80 keV. Details about the experiment are presented in this chapter.

3.1 The Portland cement sample

The images display a Portland cement cylinder exposed to CO_2 at high pressure and temperature. The cement sample is shaped as a cylinder of height ~ 4 mm and diameter ~ 5 mm, and it contains a through-going cylindrical cavity of diameter ~ 0.4 mm. The cavity functioned as a CO_2 leakage path during the experiment.

For convenience, a Cartesian coordinate system is assigned to the cement cylinder. The (x, y)-plane is defined in figure 3.1a, which displays a reconstructed cross-sectional μ-CT image. The z-axis is parallel to the longitudinal cylinder axis, and $z = 0$ corresponds to the top surface of the cement cylinder, as is illustrated in figure 3.1b.

A 3D rendered image of the cement cylinder is shown in figure 3.2a, and a semi-transparent surface-view is included in figure 3.2b. As the images suggest, the end surfaces of the cement cylinder are somewhat uneven. Moreover, the cement sample was purposely fractured prior to the experiment to be able to study the kinetics of fracture healing caused by the presence of CO_2. Schematic illustrations of the cement cylinder geometry are included in figure 3.3.

The cement specimen is of Portland G cement made with water/cement powder ratio 0.44. The cement was cured for approximately two weeks at room temperature ($\sim 20^\circ$)C and atmospheric pressure. For the first three days, the cement slurry was placed in a cylindrical mould. A nylon line ran through the slurry creating a cavity that would serve as

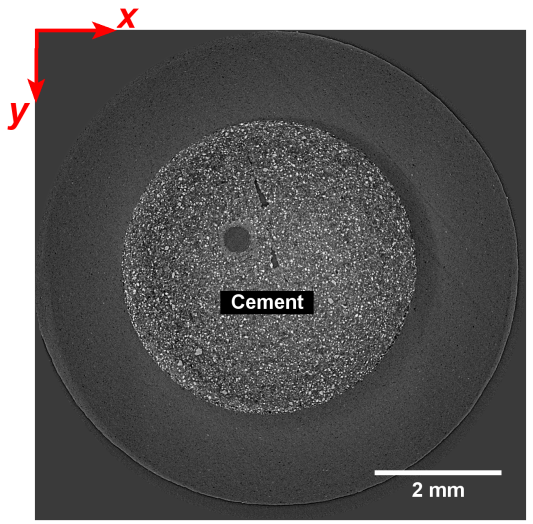

(a)

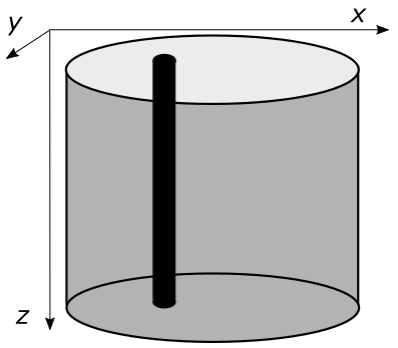

(b)

Figure 3.1: The spatial coordinate system. (a) Reconstructed CT slice image defining the (x, y)-plane. The image displays the cement cylinder surrounded by a rubber jacket and silicon oil (see section 3.2 for information about the experimental setup). Dense materials are displayed in bright shades of gray. $(x = 0, y = 0)$ is chosen to be in the upper left corner of the reconstructed μ-CT slice images. (b) Schematic illustration of the cement cylinder indicating that z refers the longitudinal axis of the cylinder. $z = 0$ at the top surface of the cement cylinder.

a CO_2 leakage pathway during the experiment. After three days, the mould and the nylon line were removed, and the sample was placed in a plastic bag with the purpose of retaining moisture during the cement hardening process. Hardened cement consists both of semi-amorphous and crystalline materials (see section 2.2). The relative content of the

crystalline phases in the cement sample was according to the supplier approximately 45% C_3S, 25% $Ca(OH_2)$, 24% C_4AF, 1% C_3A and 5% ettringite.

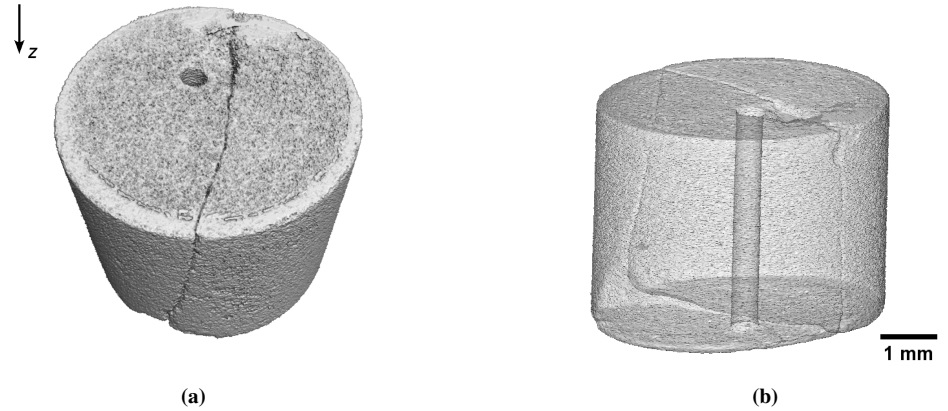

Figure 3.2: (a) 3D rendered image of the cement cylinder. (b) Semi-transparent surface-view.

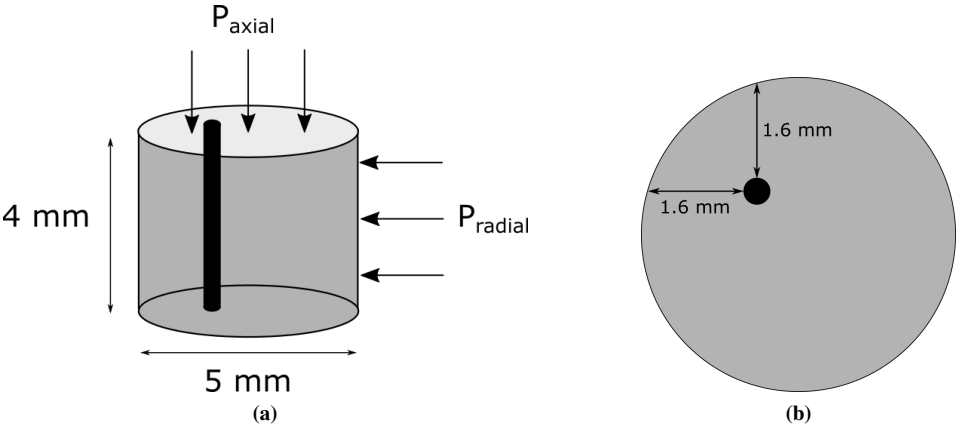

Figure 3.3: Schematic illustrations of the cement cylinder with cavity. (b) Schematic 3D view. The dimensions of the cement cylinder and the directions of axial and radial pressures exerted on the cement cylinder are indicated. (c) Cylinder top view. The approximate position of the cylindrical cavity with respect to the top surface is included.

Figure 3.4 demonstrates that the cement sample is heterogeneous. Figures 3.4a and 3.4b show 3D views of the cylinder respectively along the z-direction and x-direction. The blue-colored particles correspond to dense cement grains that, by comparison to figure 1 in Ref. [17] and figure 3 in Ref. [66], are identified as anhydrous cement grains. By visual inspection, it is clear that the grains are not uniformly distributed within the (x, y)-

plane. Large grains are not common in the region surrounding the cylindrical cavity and in particular not in the upper left quarter of the (x, y)-plane as seen in figure 3.4a.

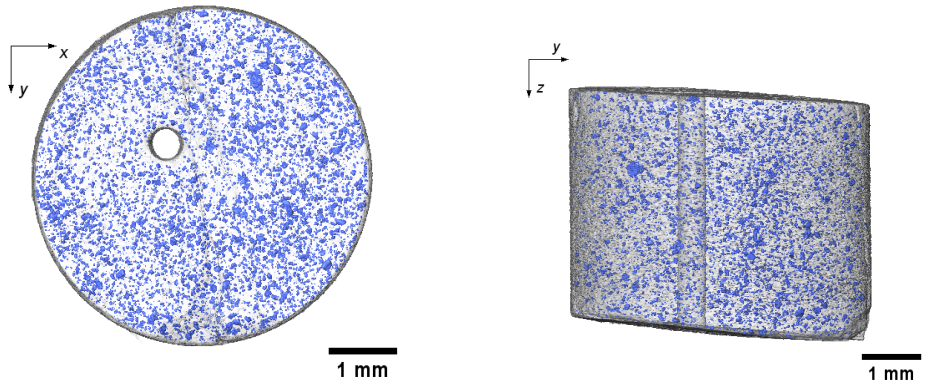

Figure 3.4: Distribution of dense (unhydrated) cement grains within the cement sample seen along (a) the z-direction and (b) the x-direction. The grains are colored in blue.

3.2 The HADES rig

The cement sample was placed in a high pressure and temperature X-ray transparent cell called HADES [67]. HADES is designed for high-energy radiation experiments in which time-lapse measurements are obtained. It is transparent to X-rays with energy above 60 keV [67]. Figure 3.6 is a schematic illustration of the components that were located inside the rig during the experiment. The cement cylinder was placed in a rubber annulus to ensure that it was isolated from surrounding silicon oil contributing to the high pressure. Moreover, volumes of sandstone of porosity $\sim 7\%$ were located above and below the cement cylinder to achieve a homogeneous flow of CO_2 towards and away from the cement.

The cement cylinder was subjected to high pressure and temperature during the experiment with the purpose of simulating reservoir conditions. The cell exerted a pressure on the cement sample both in radial and axial directions (see figure 3.3a). The axial pressure was applied both on the top and bottom end surfaces.

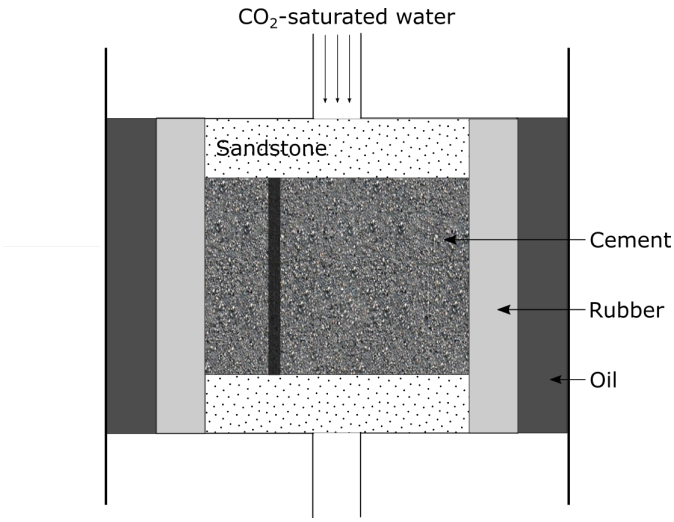

Figure 3.5: A schematic drawing of the components inside the HADES rig. The cement sample was placed between volumes of sandstone inside a rubber jacket. Silicon oil exerted pressure on the cement. CO_2–saturated water was introduced to the system from above. The figure is based on figure 3.2 in Ref. [25].

3.3 Acquisition and reconstruction of μ-CT images

Figure 3.6 shows schematically the setup for the image acquisition, including the X-ray source and detector.

Figure 3.6: Schematic illustration of the setup used for the acquisition of μ-CT projection images. For each projection image, X-rays propagated from the source towards the HADES rig, which in this figure is represented by the cement cylinder. The detector measured the intensity of X-rays that had been attenuated by the sample. The illustration is based on figure 3.3 in the author's specialization project (Ref. [25]).

The experiment lasted for approximately 20 hours. CT measurements were begun circa every eleventh minute. For each measurement, the HADES rig was rotated 180° about its axis, and 2000 projection images were obtained. The measuring time of one projection image was 0.025 seconds.

Image reconstruction was performed at ESRF making use of both absorption contrast and phase contrast. Filtered back-projection was employed to exploit the absorption contrast, and phase contrast was obtained through a method for in-line phase contrast imaging developed by Paganin et al. [41].

3.4 The timeline of the experiment

Figure 3.7 illustrates the pressures and CO_2 flow conditions applied during the experiment. A detailed description is given in the following. The first measurement was made when the axial pressure was 6 MPa and the radial pressure 5 MPa. This is defined as time $t = 0$ minutes in this thesis. Thereafter, the axial and radial pressures were increased to respectively 31 MPa and 30 MPa. CO_2-saturated water was injected to the system starting at $t = 10$ minutes with flow rate of approximately 50 ml/h. At $t = 20$ minutes, the flow rate was reduced to ~ 25 ml/h, and the second measurement was obtained at $t = 30$ minutes. From $t = 40$ minutes and throughout the remainder of the experiment, alternating static conditions and flow conditions were applied. In the periods $t = [40, 340]$ minutes and $t = [620, 860]$ minutes, static conditions were used, and thus the CO_2 resided in the cement cavity. In the periods $t = [340, 620]$ minutes and $t = [860, 1140]$ minutes, the CO_2-saturated water flowed through the cavity with flow rate 1 ml/h. Towards the end of the experiment, in the period $t = [1140, 1180]$ minutes, the flow rate was increased to 20 ml/h. It should be mentioned that there are uncertainties related to the temporal axis, arising from the fact that measurements were not begun precisely every eleventh minute.

3.5 The data set

The reconstructed data set originating from the experiment consists of 16-bit images of voxel size 6.45 μm. Images were obtained for 103 time points. For each time point, information about the cement cylinder was saved as 2D images displaying cross-sections of the cement cylinder. The dimensions of the 2D images are 1200×1200 pixels. The CT field of view is displayed in figure 3.1a for $t = 80$ minutes at $z = 1.61$ mm.

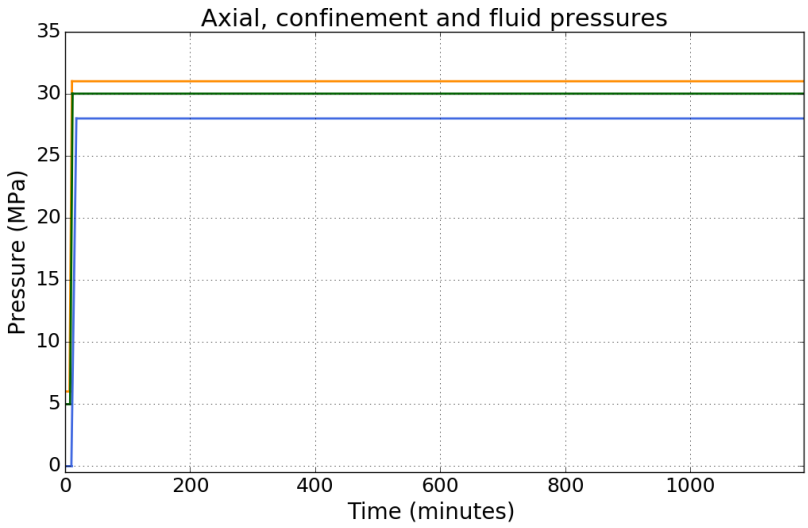

(a)

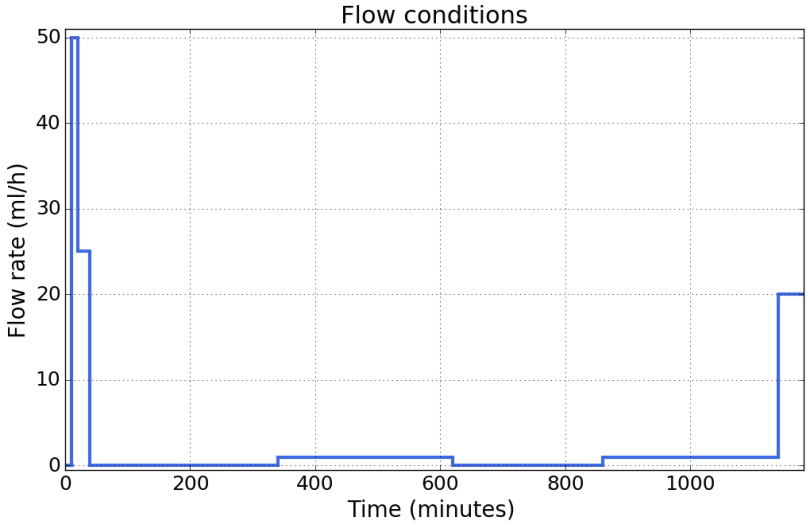

(b)

Figure 3.7: (a) Pressures and (b) CO_2-saturated water flow rate applied during the experiment. (a) The cement sample was exposed to axial pressure, radial pressure and fluid pressure. The pressures were increased at the beginning of the experiment, and thereafter kept approximately constant. (b) The flow rate of the CO_2-solution varied in the course of the experiment. The periods with zero flow rate are referred to as *static* or *nonflow* periods, whereas those with flow rate higher than zero are referred to as periods with *flow* conditions.

Chapter 4

Image processing

Image processing was performed by means of automatic procedures written in the *ImageJ Macro* scripting language. The *Fiji* software, which is a distribution of the Java-based program ImageJ [68], was applied. Automatic procedures, as opposed to manual image segmentation, was required due to the large amount of image data. ImageJ Macro scripts were created with the following objectives:

- To quantify the volume of precipitated calcium carbonate in the cylindrical cavity as a function of time.
- To measure the amount of reacted cement as a function of time.
- To investigate whether there is a deformation of the cement cylinder during the experiment.

The general approach taken is presented in figure 4.1.

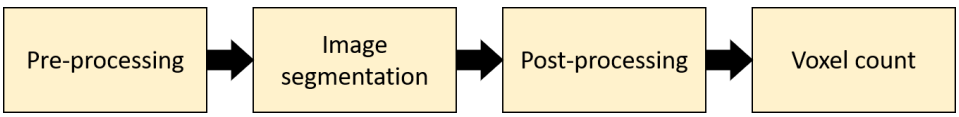

Figure 4.1: Diagram illustrating the general approach taken for image processing.

Prior to further image processing, 8-bit versions of the CT images were created to reduce the need for computer memory during the image processing.

4.1 $CaCO_3$ precipitation in the cylindrical cavity

Calcium carbonate ($CaCO_3$) crystals formed and redissolved in the cylindrical cavity in the course of the experiment. With the aim of measuring the growth and redissolution of $CaCO_3$ as a function of time, 3D image processing was performed. An action sequence was executed for each time point using an ImageJ Macro (Listing A.1 in Appendix A) consisting of four main steps as presented by figure 4.2.

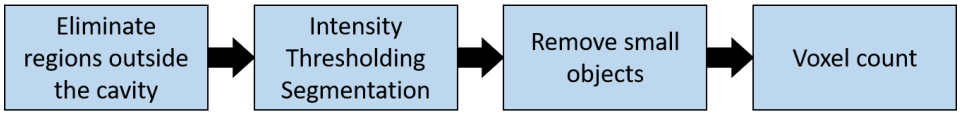

Figure 4.2: The steps performed in order to isolate the voxels corresponding to $CaCO_3$ from the surrounding voxels.

Step 1 was carried out with the purpose of reducing the probability that cement grains located outside the cylindrical cavity were labeled as precipitated $CaCO_3$. This was necessary since the intensity range of imaged $CaCO_3$ is similar to that of anhydrous cement grains present in the cement matrix. 2D ellipsoidal regions of interest (ROIs) covering the cylindrical cavity were introduced to the slice images, and the regions outside the ROIs were filled with intensity 0 (black). Figure 4.3a shows the slice image at $z = 3.35$ mm for $t = 360$ minutes after this step had been completed.

Steps 2 and 3 served to isolate the voxels corresponding to $CaCO_3$ from the surrounding voxels. First, gray-level thresholding was performed. Figure 4.3b shows the appearance of a slice image after the completion of step 2. Comparing visually the resulting images to the original gray-scale images, it was found that small objects near the cylindrical cavity walls were incorrectly labeled as $CaCO_3$. This occurred because the ROIs applied in step 1 were not utterly accurate. The issue was resolved by filtering the objects by size: it was

Figure 4.3: Reconstructed CT slice image displaying the cylindrical cavity at $z = 3.35$ mm for $t = 340$ minutes after the completion of (a) the first, (b) the second and (c) the third steps displayed in figure 4.2.

estimated that objects of volume less than approximately 65 voxels were not precipitated $CaCO_3$ and thus should be relabeled as part of the background. Figure 4.3c shows the result of the filtering operation. Finally, in step 4, the volume of the detected $CaCO_3$ grains was measured for each time point.

4.2 Reacted cement

Reacted layers developed in the cement near CO_2 contact surfaces. Two reaction zones, identified as the fully carbonated zone and the porous zone, are clearly visible in the images. The third reaction zone identified by Kutchko et al. and Mason et al. [6, 9], called the portlandite depleted zone, is not easily detectable in the CT images. The volume of the portlandite depleted zone is therefore not quantified in this project, and will for simplicity not be included when referring to *reacted cement*.

Image processing was performed with aim to measure: 1) The total amount of reacted cement in the sample as a function of time, 2) The growth of reacted cement near the CO_2 leakage pathway, and 3) The volumes of respectively the porous zone and the fully carbonated zone near the CO_2 leakage pathway as functions of time.

4.2.1 Volume of reacted cement

Reacted cement developed both near the cylinder end surfaces and near the cylindrical cavity. Automatic routines for image processing were designed with the objective to quantify the volume of reacted cement (combined volume of the porous and fully carbonated zones) in the cylinder as a function of time. The procedures for image processing were incorporated in an ImageJ Macro which is included in listing A.2 in Appendix A. The entire cylinder was considered except the topmost and bottommost $\sim 45\mu$m of the cement cylinder, which was excluded because of complications during image segmentation caused by the presence of sandstone at the cylinder end surfaces.

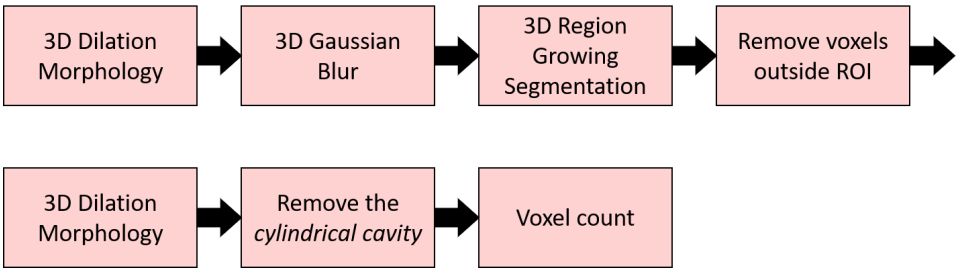

Figure 4.4: Schematic representation of the operations performed with the purpose of isolating the image voxels corresponding reacted cement in the cement cylinder from the surrounding image voxels.

The routine for image processing is presented in figure 4.4. First, morphological dilation was carried out using a cubic structuring element. The operation was performed to exploit the fact that unreacted cement has a higher content of bright grains than unreacted cement does. Consequently, the morphological dilation increased the displayed intensity of the unreacted cement more than that of the reacted cement. Figure 4.5 illustrates how the images were transformed by the morphological operation. Next, 3D Gaussian blur was carried out with the purpose of smoothing intensities. The result is displayed in figure 4.5c. Thereafter, 3D single linkage region-growing was performed. Inconveniently, some voxels in the rubber surrounding the cement were labeled as part of the image foreground and had to be relabeled in a separate step. Next, morphological dilation was performed once again with the purpose to fill small holes caused by noise and to relabel voxels that were wrongly categorized as background voxels on account of the first dilation operation. Moreover, the volume of $CaCO_3$ located in the cylindrical cavity had to be subtracted from the image foreground. The cylindrical cavity including precipitated $CaCO_3$ was segmented using a separate ImageJ Macro, which is described in section 4.3.2 below. Finally, the number of voxels corresponding to reacted cement was counted.

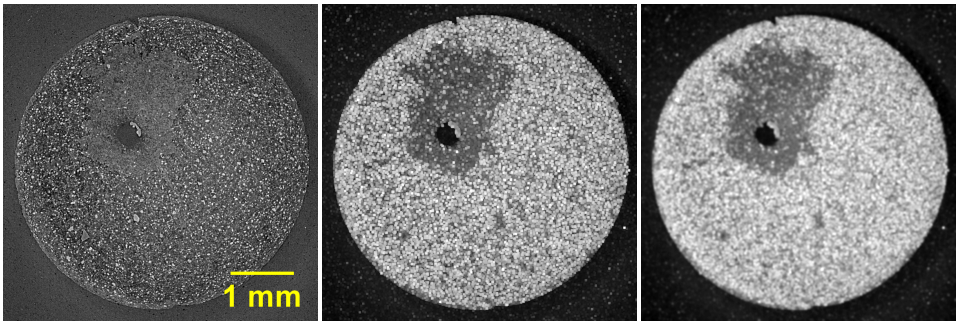

Figure 4.5: The transformation through image processing of a reconstructed CT slice image located at $z = 0.6$ mm for $t = 620$ minutes. The CT image prior to the image processing is displayed in (a), and the appearance of the image after the first dilation operations has been performed is displayed in (b). (c) displays the image after the Gaussian blur algorithm has been executed.

4.2.2 Reacted cement near the cylindrical cavity

The cement near the cylindrical cavity is considered in more detail in the following. The top ($\sim$ 1 mm) and bottom ($\sim$ 0.7 mm) segments of the cement cylinder are disregarded because they also experience carbonation caused by CO_2 present at the end surfaces. In addition to the method for image processing described above (from hereon referred to as *Method 1*), a second method (*Method 2*) is carried out. There are errors related to both methods, and hence it is useful to compare the two resulting volume series. As for the previous section, the portlandite depleted zone is not included in the segmentation.

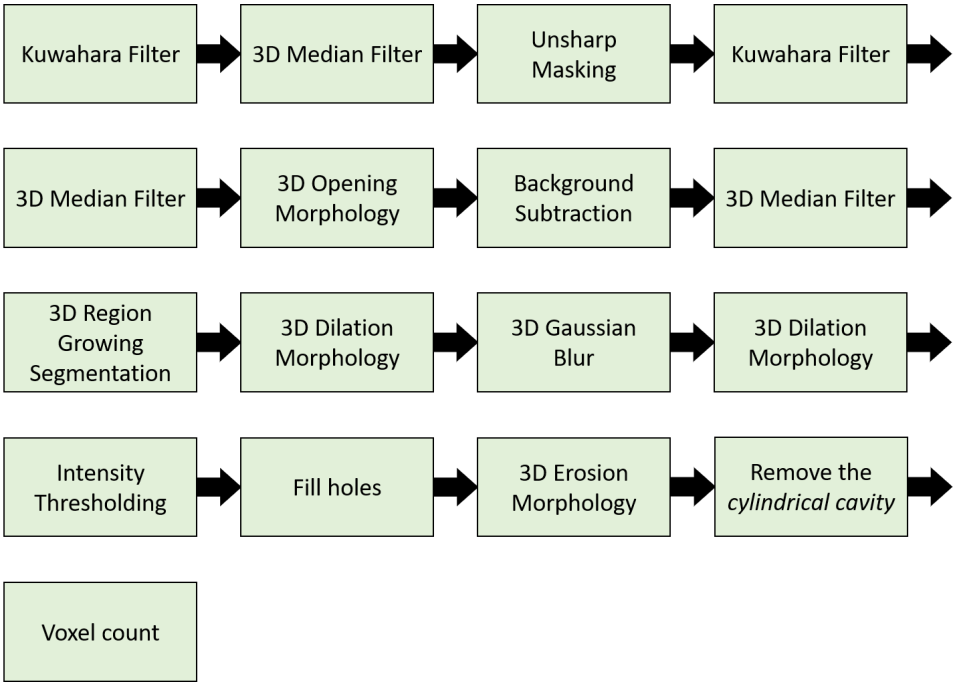

Figure 4.6: The procedure corresponding to Method 2. It is executed for each time point with the purpose of extracting the reacted cement near the cylindrical cavity from the surrounding regions in the CT images.

The routine for image processing of Method 2 is presented in figure 4.6 and in listing A.3 in Appendix A. The two first operations of the procedure served to remove noise. Thereafter, the reacted cement was highlighted using unsharp masking. Image 4.7b illustrates the appearance of a slice image after the completion of this operation. Next, further noise reduction was performed, followed by 3D morphological opening using a cubic structuring element. The purpose of the latter operation was to create a homogeneous low-intensity image background without decreasing the intensity of voxels corresponding to the reacted cement. An example of a resulting slice image is shown in figure 4.7c. The contrast between the reacted and unreacted cement was further improved by running the subtract background algorithm, which is explained in section 2.6.

Image segmentation was performed by means of 3D single linkage region-growing. An example of a resulting image is displayed in 4.7d. Further image processing was required as significant parts of the reacted cement were not labeled correctly. Operations were performed with aim to make the annulus-shaped image foreground continuous in all slice images. The result is illustrated by image 4.7e. Thereafter, the region inside the annulus was added to the image foreground using a 2D *Fill holes* operation, and morphological erosion was carried out to re-assign voxels to the image background that had erroneously been labeled as reacted cement by previously performed dilation operations. Image 4.7f shows

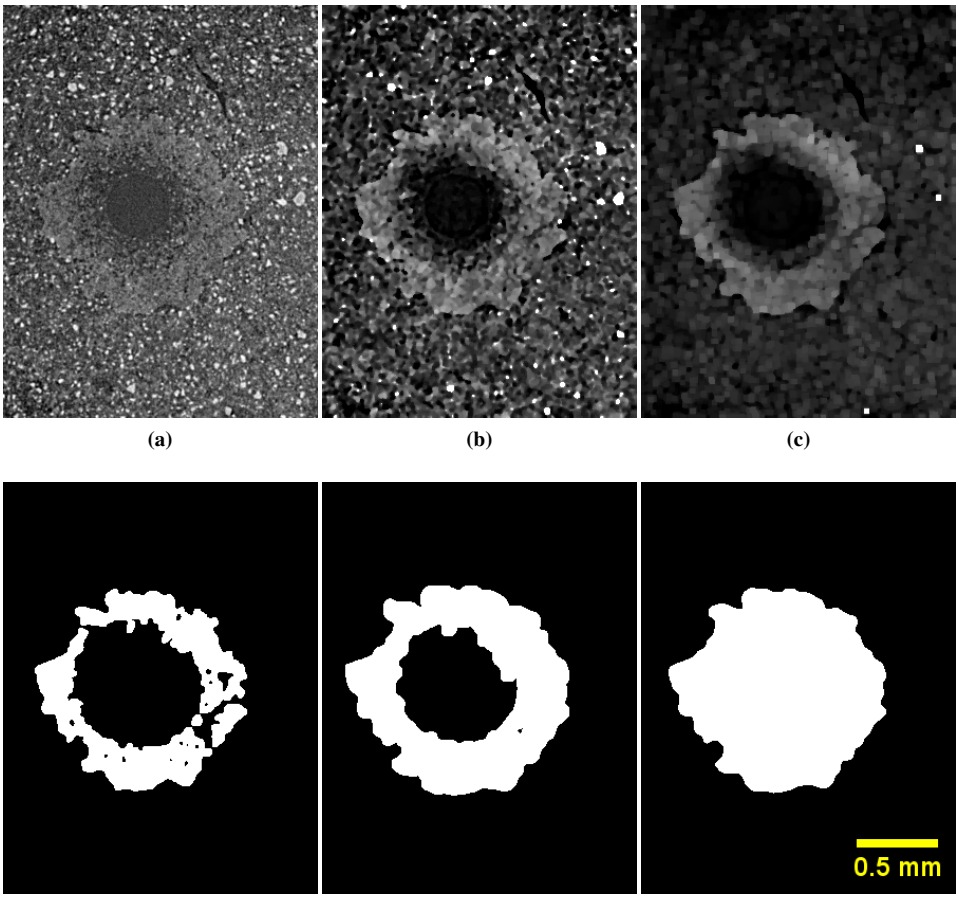

Figure 4.7: The transformation of a reconstructed CT slice image (located at $z = 3.35$ mm for $t = 340$ minutes) by image processing. The aim of the image processing was to extract the reacted cement near the cylindrical cavity from the surrounding region. See figure 4.6 for an overview of the performed operations. (a) Original CT image. (b-f) The image at different stages during the image processing: (b) after the completion of unsharp masking, (c) after 3D morphological opening, (d) after connected region-growing, (e) after intensity thresholding, and (f) after morphological erosion.

how a slice image has been transformed at this point. As can be seen, the cylindrical cavity is included in the image foreground, which occurred attributed to the *Fill holes* operation. Voxels corresponding to the cylindrical cavity (including precipitated $CaCO_3$) were thus subtracted from the images. The series of operations is completed by the measurement of foreground voxels.

4.2.3 The porous zone and the full carbonated zone

It is of interest to measure the growth of respectively the porous zone and the fully carbonated zone surrounding the cylindrical cavity to get an improved insight into the carbonation kinetics. As for the combined volume of the these reaction zones near the cavity, the top ~ 1 mm and bottom ~ 0.7 mm of the cylinder are not considered in the following.

The porous zone

Listing A.4 in Appendix A contains a series of operations that were performed in order to measure the volume of the porous zone near the cylindrical cavity for each time point. The steps are also presented in figure 4.8.

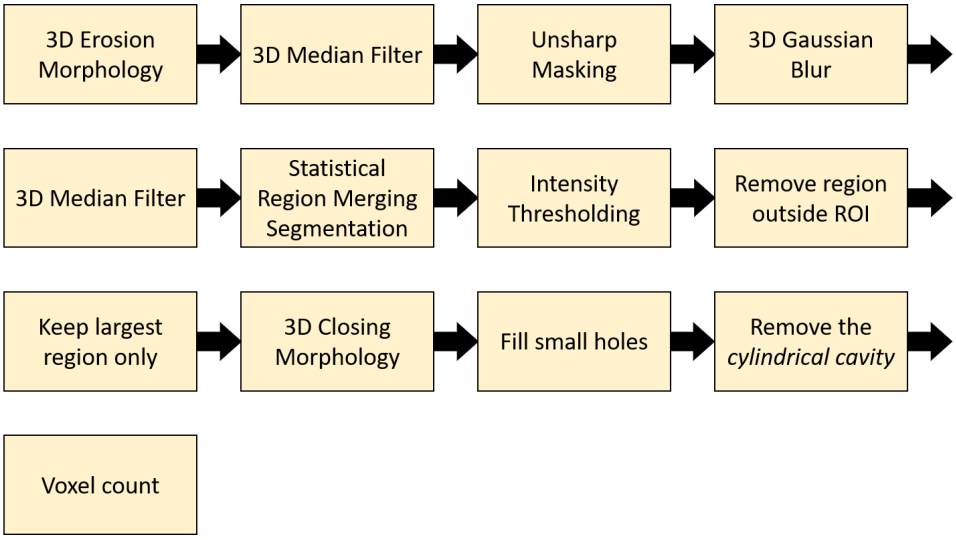

Figure 4.8: The series of operations used for segmentation of the porous zone near the cylindrical cavity.

The first step of the series of operations was to remove any bright voxels within the reaction zones by morphological erosion using an elliptical structuring element elongated in the z-direction. Thereafter, the median filter was run to smooth the image, and unsharp masking transformed the image so that the low-frequency components were highlighted. This enhanced the reaction zones. Next, the Gaussian blur filter and the median filter

were applied to reduce noise. Figure 4.9b displays the appearance of a slice image after the completion of these steps. 3D statistical region merging, which is a region-growing segmentation technique, was carried out subsequently. The resulting segmented image is shown in figure 4.9c. To extract the low-intensity regions, intensity thresholding was performed. The porous zone was separated from other low-intensity regions using customized ROIs. Thereafter, only the largest 3D region was contained, leading to the removal of voxel outliers. 3D morphological closing followed by the 2D hole filling operation were carried out with the purpose of compensating for errors caused by image noise. Finally, the cylindrical cavity was removed from the image foreground, and the number of voxels labeled as part of the porous zone were counted.

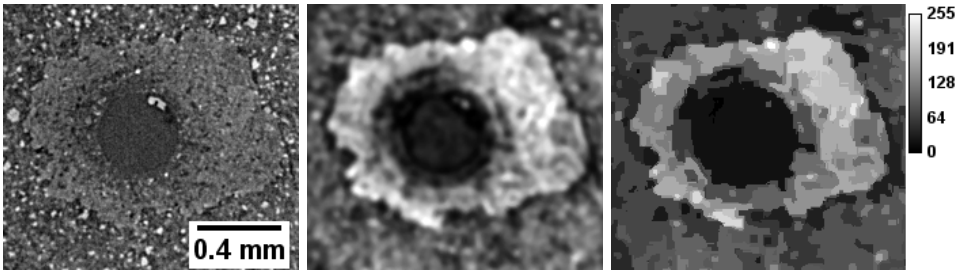

Figure 4.9: The transformation of a reconstructed CT slice image (located at $z = 3.1$ mm for $t = 960$ min) by image processing. The image displays reacted cement surrounding the cylindrical cavity, and the purpose of the image processing is to isolate the porous zone from the surrounding regions. (a) The image prior to image processing. (b) The image after the five first operations presented in figure 4.8 have been performed. (c) The image after statistical region merging has been executed.

The fully carbonated zone

The volume of the fully carbonated zone was calculated by subtracting the volume of the porous zone from the combined volume of the porous and fully carbonated zones. Two versions of segmentation of the fully carbonated zone was performed. For the first version, the combined volume of the reaction zones was achieved by Method 1 as defined in section 4.2.1. For the second version, Method 2, as is explained in section 4.2.2, was employed.

4.3 Mechanical deformation of the cement cylinder

This section presents procedures for image processing that are designed to investigate whether there is a deformation of the cement cylinder during the experiment. The volume

of the cement cylinder [1] and the cylindrical cavity are measured for all time points. Moreover, an improved insight into the deformation of the cylinder is achieved by considering the movement of selected cement grains in the course of the experiment.

4.3.1 The cement cylinder

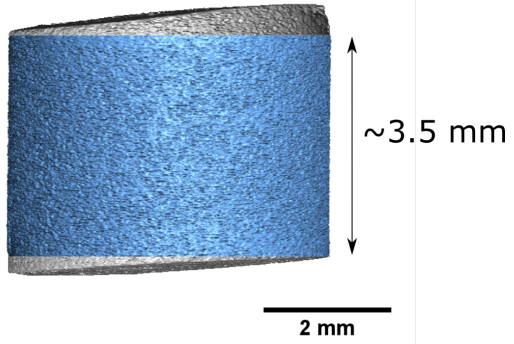

Figure 4.10: Only the blue-colored region is included in the image processing performed to measure the volume of the cement cylinder as a function of time.

Image processing was carried out with the objective to extract the cement cylinder from the surrounding rubber. Figure 4.10 illustrates the region of the cement cylinder (colored in blue) that was isolated through image segmentation. The top and bottom cylinder volumes were excluded because a high uncertainty was related to the image segmentation of these regions. Three main factors contributed to the high uncertainty: 1) The density of the sandstone adjacent to the cylinder ends is similar to the density of cement, 2) The cylinder ends experienced a significant density change in the course of the experiment due to interactions with CO_2, and 3) The cement surface at the cylinder ends was uneven (see figure 3.3 in Chapter 3), which caused additional errors during the image processing.

The image processing carried out for each time point is presented in figure 4.11 and in listing A.5 in Appendix A. First, unsharp masking was executed with the purpose of highlighting the cement grains. Thereafter, the contrast between the cement and the surrounding rubber was further improved using an algorithm for background subtraction described in section 2.6.1. Figure 4.12b shows how a slice image has been transformed at this point. Next, 3D morphological closing was performed using a cubic structuring element. The result is displayed in figure 4.12c. The closing operation exploits that the cement, unlike the rubber, contains bright grains. Next, image segmentation was performed using an intensity threshold. The result is displayed in figure 4.12d. Subsequently, image post-processing was carried out, including the closing of holes in the image foreground, removing outlying voxels and 3D morphological closing. Moreover, the cylindrical cavity, which had

[1] The top and bottom end regions of the cement cylinder are not included. See subsection 4.3.1 for an explanation.

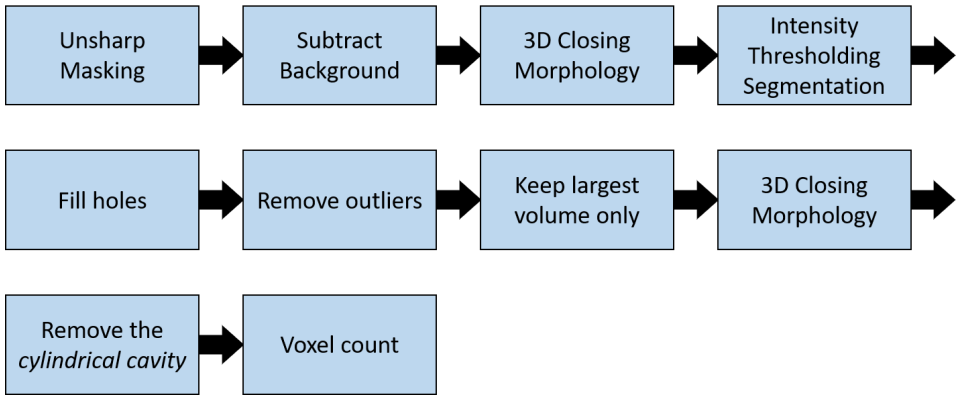

Figure 4.11: Schematic presentation of the series of image operations performed with the purpose of isolating the cement sample from the surrounding rubber.

been characterized as part of the image foreground during the image post-processing, was subtracted. Lastly, the number of voxels corresponding to the cement was counted.

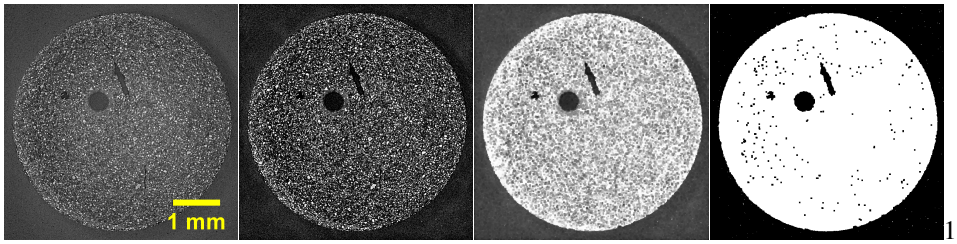

Figure 4.12: Comparison of a reconstructed CT slice image (located at $z = 1.7$ mm for $t = 80$ min) at different stages of the image processing procedure. An overview of all the steps of the image processing is presented in figure 4.11. (a) displays the image prior to image processing, whereas (b-d) illustrate how it was transformed after (b) subtraction of the image background, (c) 3D morphological closing and (d) intensity thresholding.

4.3.2 The cylindrical cavity

Figure 4.13 displays the series of operations performed with the aim of obtaining a segmentation of the cylindrical cavity. The corresponding ImageJ Macro script is included in listing A.6 in Appendix A. First, 3D morphological closing with a cubic structuring element was carried out, which increased the homogeneity of the cement surrounding the cylindrical cavity. The intensities were further smoothed using respectively a 3D median filter and 3D mean filter. The result is shown in figure 4.14b for $t = 970$ minutes at

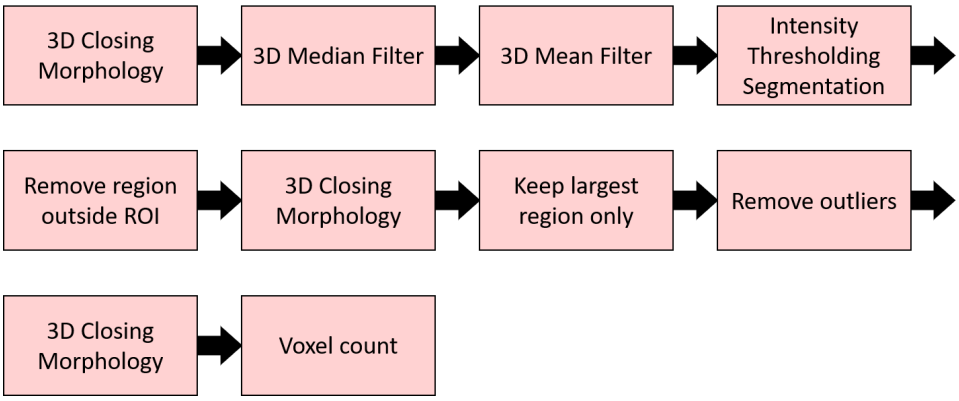

Figure 4.13: Diagram illustrating the operations performed with purpose to measure the volume of the cylindrical cavity as a function of time.

$z = 2.5$ mm. Thereafter, intensity thresholding was carried out. Unfortunately, also voxels in the porous zone had intensities in the chosen intensity range. To reduce the problem, voxels that in all likelihood were part of the reacted cement were removed from the image foreground using elliptical regions of interest (ROIs). Next, only the largest connected 3D region for each time point was contained as the cylindrical cavity should be continuous in space. Thereafter, operations were performed to smooth the edge of the cylindrical cavity, which was done based on the assumption that the cylindrical cavity had approximately an elliptical shape in the (x, y)-plane and hence a rather smooth edge. Narrow passages adjacent to precipitated $CaCO_3$ crystals as seen in figure 4.14c were removed, and the number of voxels in the image foreground was counted for all time points.

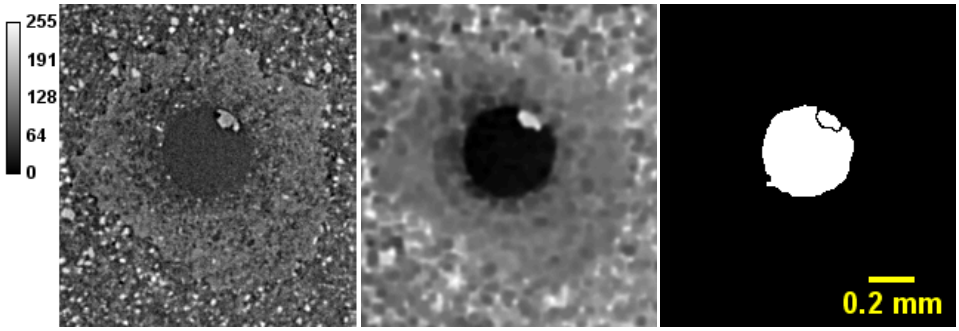

(a) **(b)** **(c)**

Figure 4.14: The transformation of a reconstructed CT slice image at $z = 2.5$ mm for $t = 960$ min by image processing (see figure 4.13 for the series of operations performed). (a) displays the original image, whereas (b) is the slice image after the first three operations as presented in figure 4.13 has been executed. For (c), also intensity thresholding has been performed.

4.3.3 Movement of cement grains

With the aim of gaining improved insight into the deformation of the cement cylinder, a number of cement grains were segmented and their movements along the z-axis tracked. The segmentation was carried out using single linkage region-growing segmentation with no pre- or post-processing. The z-position of each grain at $t = 80$ min and $t = 1180$ min was measured and compared to one another.

4.4 Uncertainty estimates

The uncertainty related to the performed image segmentation was estimated in a "worst-case" manner, which involves that the measured quantity should be found within the range of values covered by the uncertainty estimate[2]. The uncertainty was estimated based on the following procedure: For each feature to be isolated, two versions of manual segmentation were performed for a small selection of slice images of various z- and t-values. In the first version, the segmentation was carried out so that the isolated region consisted of the *minimal* number of voxels that could be considered to be part of the feature of interest. In the second version, the *maximal* number of voxels were included. Figure 4.15 illustrates the area of a slice image labeled as reacted cement by minimal (figure 4.15a) and maximal (4.15b) manual segmentation. The uncertainties of automatically performed image segmentation were estimated by comparing the areas of labeled regions obtained through manual segmentation and those achieved through automatic procedures. The uncertainty of the performed segmentation is further dealt with in section 6.1.

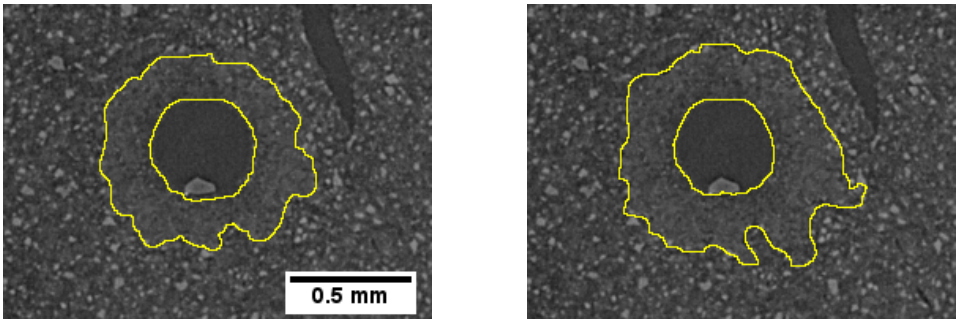

(a) **(b)**

Figure 4.15: The area labeled as reacted cement by manual image segmentation with (a) a minimal inclusion of voxels and (b) a maximal inclusion of voxels are contained within the yellow lines. The reconstructed CT image displayed corresponds to $t = 520$ minutes at $z = 2.9$ mm.

[2]For an introduction to worst-case uncertainty, see for instance Ref. [69].

Chapter 5

Results

5.1 Qualitative observations

The in-situ μ-CT experiment revealed chemical processes occurring in the cement cylinder during the experiment, including precipitation and re-dissolution of calcium carbonate both in the cement matrix and in the CO_2 leakage pathway.

Crystals of calcium carbonate ($CaCO_3$) grew at the walls of the cylindrical cavity during the first period of static conditions. The crystal growth was localized, and the crystals were approximately of spherical shape. During the periods of CO_2 flow, the calcium carbonate re-dissolved. The process of crystal precipitation and re-dissolution can be observed in figure 5.1, which shows that at $t = 80$ minutes and $t = 1130$ minutes, $CaCO_3$ crystals are not detected. At $t = 630$ minutes on the other hand, bright crystals are visible in the cavity.

In the course of the experiment, the density of cement near CO_2 contact surfaces, including both the cylinder ends and the cylindrical cavity, became modified. Figure 5.1 illustrates the growth of reacted cement near the cylindrical cavity. The front of the visible reacted cement is colored in yellow. Two reaction zones that are identified as the porous zone and the fully carbonated zone based on the terminology used in recent studies are clearly visible in the CT images. The porous zone is seen as a region consisting of low-intensity voxels adjacent to CO_2 contact surfaces, and the fully carbonated zone is a bright region surrounding the porous zone. Figure 5.1 shows that the spatial transition between the two zones is rather gradual. Moreover, in particularly figure 5.1c illustrates that the reacted cement has not grown isotropically about the cylindrical cavity.

The CT images revealed that the growth of the porous and fully carbonated zones depended on the CO_2 flow rate. In general, the volume of reacted cement grew faster during CO_2 flow conditions than during static conditions. This is the case both for the reacted

cement surrounding the CO_2 leakage pathway and for the reacted cement at the cylinder ends.

The third reaction zone predicted by the geochemical model (see section 2.3) is not easily detectable in the CT images. A thin ($\sim 20\mu$m) region outside the fully carbonated zone is slightly less dense than the adjacent unreacted cement and may be interpreted to be the portlandite depleted zone. However, due to density variations in the unreacted cement, it is difficult to visually detect the transition between the portlandite depleted zone and unreacted cement.

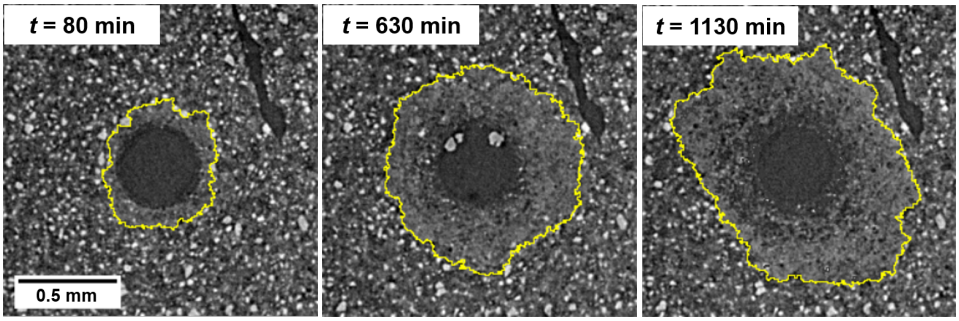

Figure 5.1: The growth of reacted cement seen for a reconstructed CT slice image located at $z = 2.1$ mm for (a) $t = 80$ min, (b) $t = 630$ min and (c) $t = 1130$ min. The cement region contained within the yellow line consists of the porous and fully carbonated reaction zones.

5.2 $CaCO_3$ precipitation in the cylindrical cavity

The temporal evolution of precipitated $CaCO_3$ was measured after image segmentation had been performed. Figure 5.2 illustrates how the images were transformed by the segmentation process.

A 3D view of the segmented precipitated $CaCO_3$ is displayed in figure 5.3. Four time points are included: $t = 120$ min, $t = 340$ min, $t = 620$ min and $t = 1110$ min. The yellow voxels correspond to the $CaCO_3$, whereas the dark gray voxels represent the cement. The figure shows that the $CaCO_3$ precipitates first in the upper part of the cylindrical cavity. Moreover, the crystal growth is not uniform in the (x, y)-plane. The preferential location is at the left part of the cylindrical cavity in the view of figure 5.3.

Figure 5.4 presents the $CaCO_3$ volume measurements. The red curve refers to the total amount of $CaCO_3$ in the cylindrical cavity, and the orange band indicates the worst-case uncertainty of the measurements, which was estimated to be 14 $\%$. The blue and yellow lines correspond to the volume of $CaCO_3$ in respectively the upper and lower half of the cavity.

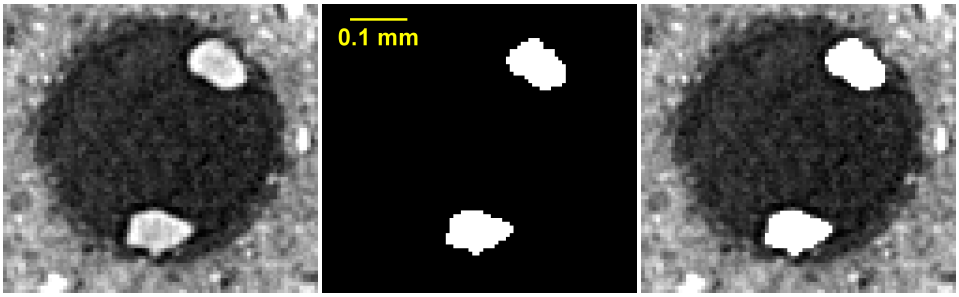

Figure 5.2: The segmentation of precipitated $CaCO_3$ in the cylindrical cavity at $z = 2.0$ mm for $t = 340$ minutes. (a) Reconstructed CT slice image prior to the image segmentation. (b) The segmented slice image. (c) A slice image created by adding the intensity values of (a) and (b) that illustrates which voxels that were labeled as precipitated $CaCO_3$.

The crystal precipitation occurred in the first quarter of the experiment, during which nonflow CO_2 conditions were applied. The total volume of detected $CaCO_3$ went from zero to 28 ± 0.4 mm^3. From $t \sim 180$ minutes, the growth rate of the volume measurements was linear ($\sim 10^{-4}$ mm^3/min). Nonflow CO_2 conditions were applied also during $t = [620, 860]$ minutes, but no $CaCO_3$ precipitation was observed for this time interval. Throughout the remainder of the experiment, the $CaCO_3$ re-dissolved. In the time intervals with CO_2 flow rate of 1 ml/h, an approximately linear volume decrease was measured. The measured dissolution rate was the same during both periods of flow rate 1 ml/h ($\sim -4 \times 10^{-5}$ mm^3/min). Furthermore, the dissolution rate increased by a factor of ten upon the introduction of CO_2 flow rate of 20 ml/h at $t = 1140$ minutes. At the end of the experiment, the cylindrical cavity was, according to the measurements, emptied of solid $CaCO_3$. Figure 5.4 shows that the precipitation was larger in the upper half of the cylindrical cavity than in the lower half. When CO_2 flow rate of 1 ml/h was introduced at $t = 340$ minutes, the volume of $CaCO_3$ in the upper part of cylindrical cavity was approximately twice as large as that in the lower part.

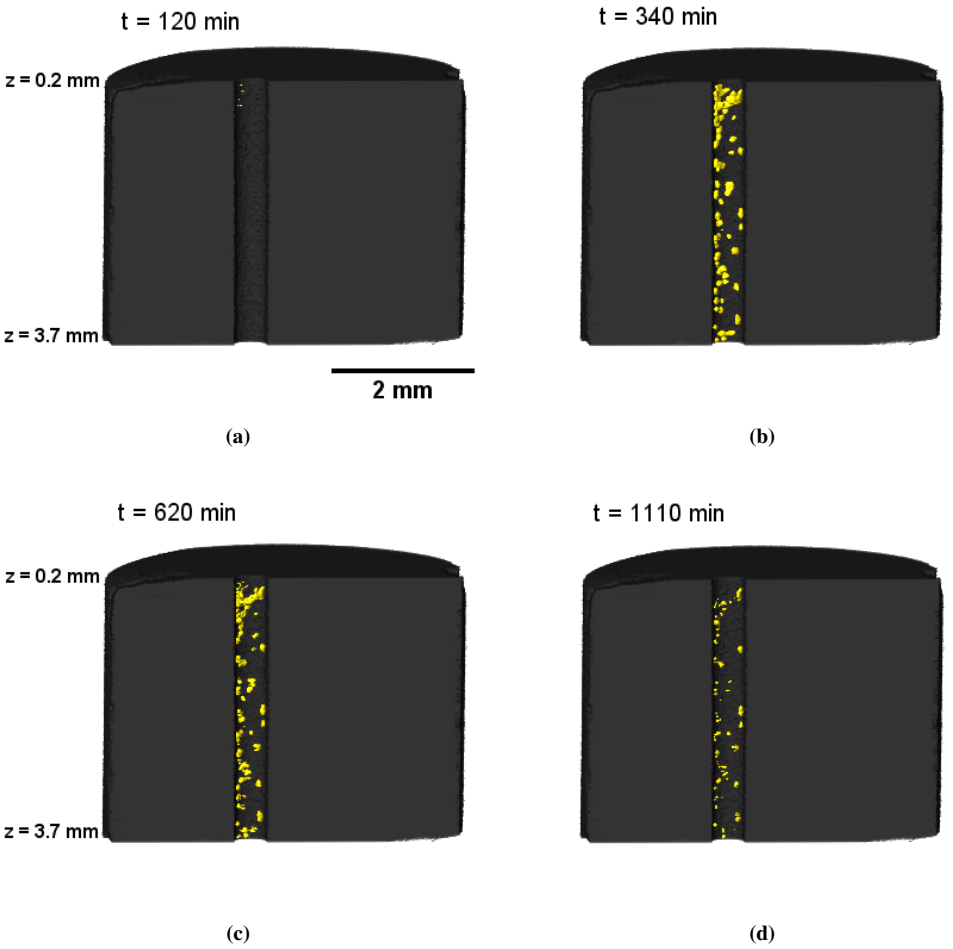

Figure 5.3: 3D visualization of precipitated $CaCO_3$ in the CO_2 leakage pathway for $t = 120$, $t = 340$, $t = 620$ and $t = 1110$ minutes. The $CaCO_3$ is colored in yellow, and the cement cylinder in dark gray.

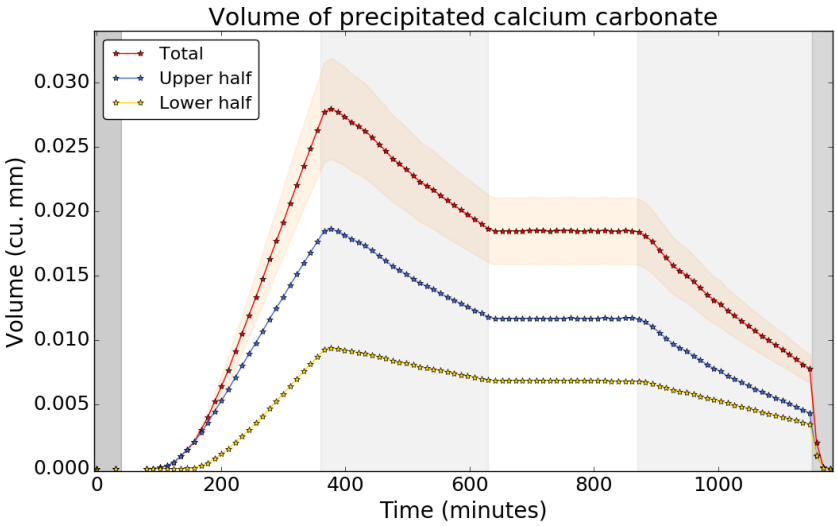

Figure 5.4: The time evolution of the volume of solid $CaCO_3$ in the cylindrical cavity. The worst-case uncertainty of the segmentation is estimated to be $\sim 14\%$. The red curve corresponds to the total amount of precipitated $CaCO_3$, whereas the blue and yellow curves correspond to $CaCO_3$ in respectively the upper and lower half of the cylindrical cavity. The orange band illustrates the worst-case uncertainty of the measurements. The background colors indicate the CO_2 flow conditions: Dark gray (assigned to $t < 40$ min) refers to high CO_2 flow rates (25-50 ml/h) applied during the CO_2 injection period; white color refers to no CO_2 flow; light gray color indicates flow rate of 1 ml/h; and medium gray at high t-values represents flow rate of 20 ml/h.

5.3 Reacted cement

5.3.1 Volume of reacted cement

The combined volume of the fully carbonated zone and the porous zone in the cement cylinder was measured after image segmentation had been performed. The result of the segmentation is shown in figure 5.8 for an example slice image located near the bottom surface of the cylinder. A 3D rendering of the segmented reacted cement is displayed in figure 5.6 for $t = 80$ minutes, $t = 620$ minutes and $t = 1170$ minutes.

Figure 5.7 shows the results of the volume measurements. The red curve corresponds to the volume of reacted cement in the cement sample as a function of time. The worst-case uncertainty of the measurements is visualized by the orange band. It is estimated to be 17% of the measurement values. The figure also displays the volume of reacted cement in the top (blue color) and bottom (yellow color) ~ 0.9 mm cylinder end segments only, and the

volume of reacted cement in the middle part of the cement cylinder (green color).

Figure 5.5: Image segmentation of the combined volume of the fully carbonated zone and the porous zone for a reconstructed CT slice image at $z = 3.6$ mm for $t = 620$ minutes. (a) The reconstructed CT image prior to the image processing. (b) The result of the image segmentation. (c) The outline of (b) added on (a) for an improved visualization of the segmentation.

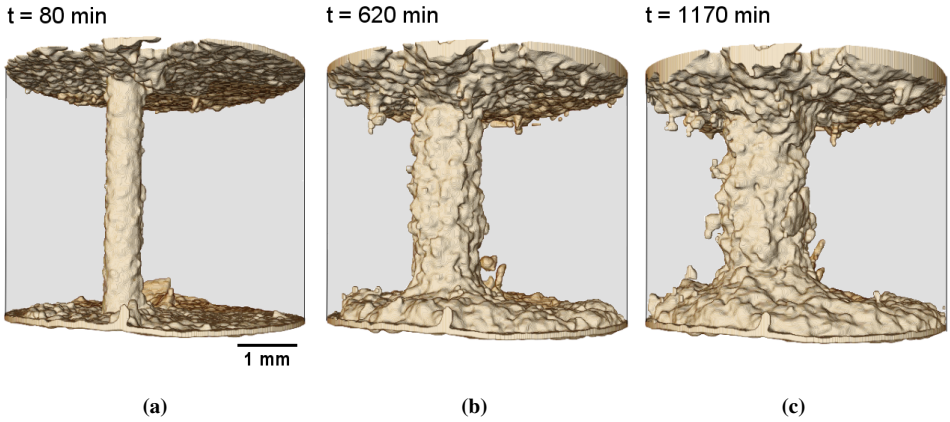

Figure 5.6: 3D volume rendering of the reacted cement at $t = 80$, $t = 620$ and $t = 1170$ minutes. The gray background represents the cement cylinder.

The growth of reacted cement was significantly faster during CO_2 flow than nonflow conditions. Moreover, for nonflow conditions, the volume increase was found to be approximately the same during the first ($t = [80, 340]$ minutes) and second ($t = [620, 860]$ minutes) measurement series. This was not the case for the time intervals of CO_2 flow of 1 ml/h: the growth rate of the volume for the first period of flow 1 ml/h ($t = [340, 620]$ minutes) was found to be approximately twice that of the second ($t = [860, 1140]$ minutes).

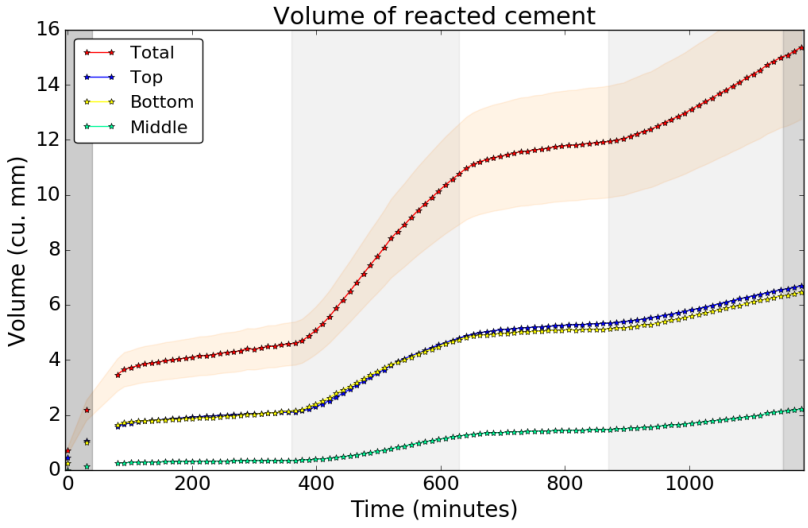

(a)

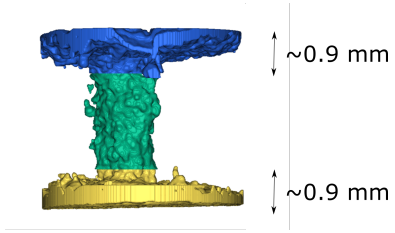

(b)

Figure 5.7: (a) The combined volume of the porous and fully carbonated zones in the cement cylinder as a function of time. The red curve includes the reacted cement both at the cylinder ends and near the cavity. The worst-case uncertainty of the measurements is estimated to be $\sim 17\%$, and this is indicated by the orange band. The blue and yellow curves refer to the reacted cement in respectively the top and bottom parts of the cylinder, and the green curve presents the volume of reacted cement in the middle part of the cylinder. The background colors indicate the CO_2 flow conditions: Dark gray (assigned to $t < 40$ min) refers to high CO_2 flow rates (25-50 ml/h) applied during the CO_2 injection period; white color refers to no CO_2 flow; light gray color indicates flow rate of 1 ml/h; and medium gray at high t-values represents flow rate of 20 ml/h. (b) 3D rendering of the reacted cement illustrating the volume included as part of the cylinder top (blue color), bottom (yellow color) and middle part (green).

5.3.2 Reacted cement near the cylindrical cavity

The combined volume of the fully carbonated zone and the porous zone growing around the cylindrical cavity was segmented using two methods for image processing named Method 1 and Method 2 (see section 4.2.2). Both methods provide with a satisfactory segmentation based on the bounds determined using manual segmentation as described in section 4.4. Figure 5.8 shows the segmentation results for both methods for a slice image located at $z = 1.0$ mm for $t = 620$ minutes.

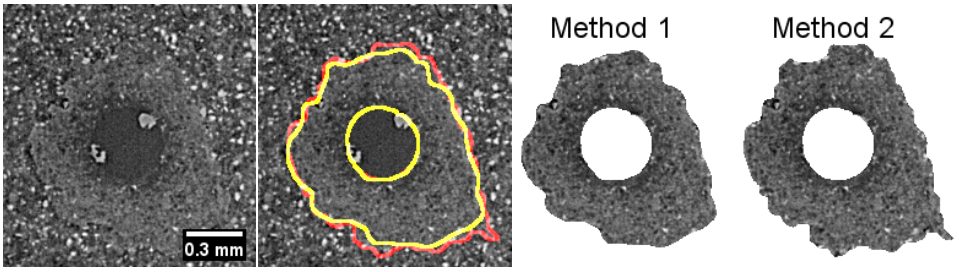

Figure 5.8: The region labeled as reacted cement near the CO_2 leakage path. (a) A reconstructed CT slice image at $z = 1.0$ mm for $t = 620$ minutes. (b) Outlines of regions labeled as reacted cement by Method 1 (yellow line) and Method 2 (red line). (c) The region categorized as reacted cement by Method 1. (d) The region categorized as reacted cement by Method 2.

Figure 5.9 displays the volume series as obtained by Method 1 and Method 2. The worst-case uncertainty is indicated by the orange band. During the first $\sim$ 1100 minutes of the experiment, Method 2 categorized more voxels as reacted cement than did Method 1. Moreover, in the course of the first period of static conditions, Method 1 resulted in a volume increase that was one order of magnitude greater than that measured by Method 2. Even so, both methods gave that the growth of reacted cement during the second period with static conditions was greater than that of the first. Furthermore, the results show that the growth of reacted cement was faster for the first period of flow rate 1 ml/h than for the second one. The average radial propagation velocity of the front of reacted cement was approximately reduced by half for the second period of flow rate 1 ml/h compared to the first.

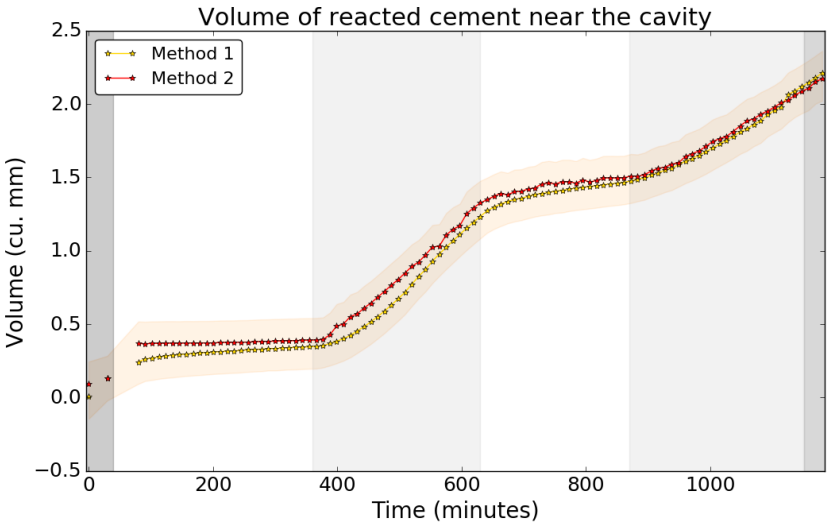

Figure 5.9: Volume of reacted cement near the cylindrical cavity obtained using Method 1 (yellow curve) and Method 2 (red curve) for image processing. The estimated worst-case uncertainty of each measurement is indicated by the orange band. The uncertainty is based on manual segmentation performed as described in section 4.4. The background colors refer to the CO_2 flow conditions as in previous figures.

5.3.3 The porous zone and the fully carbonated zone

Segmentation of respectively the porous zone and the fully carbonated zone was performed as described in section 4.2.3. The result of the segmentation is visualized in figure 5.10 for an image at $z = 2.5$ mm for $t = 1180$ minutes. Figure 5.11 illustrates a 3D volume rendering of the segmentation for $t = 80$ min, $t = 630$ min and $t = 1180$ min.

Figure 5.12 displays the measured *volume* and *average radial width* of the porous zone and the fully carbonated zone near the cylindrical cavity. Two estimates of the fully carbonated zone are included: the curve shown in yellow is calculated based on Method 1, whereas the red curve corresponds to Method 2[1]. The worst-case uncertainty of the volume measurement is indicated in green for the porous zone and in orange for the fully carbonated zone in figure 5.12a.

According to the measurements, the growth of the porous zone was very limited while static CO_2 conditions were applied. Regarding the fully carbonated zone, a volume increase was observed for the second nonflow period ($[t = 620, 860]$ minutes). Method 2 indicates also a volume increase for the first period of static conditions ($t = [80, 340]$ minutes).

[1] See Section 4.2 for a description of Method 1 and Method 2 and the method for calculating the fully carbonated zone.

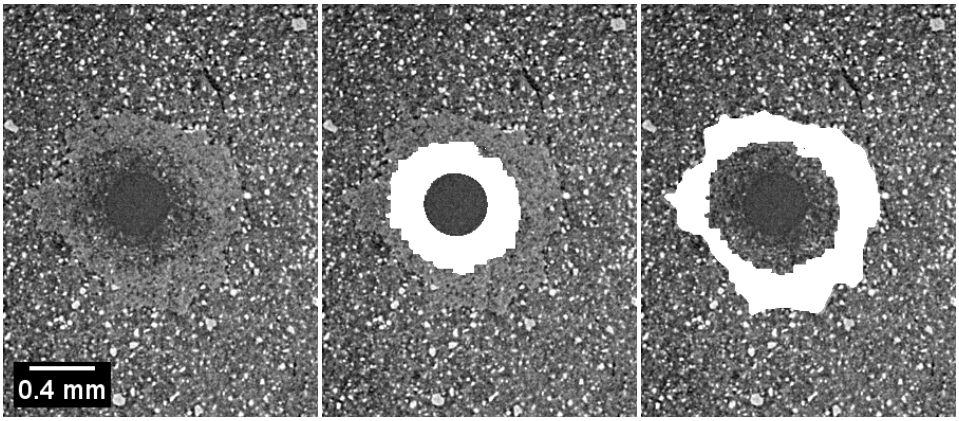

Figure 5.10: Segmentation of the porous zone and the fully carbonated zone for a reconstructed CT image at $z = 2.5$ mm for $t = 1180$ minutes. (a) Original reconstructed CT slice image. (b) The region labeled as part of the porous zone is colored in white. (c) The region labeled as part of the fully carbonated zone by Method 2 is colored in white.

A *volumetric* growth was observed for both for the fully carbonated zone and the porous zone during CO_2 flow conditions (see figure 5.12a). During the first period of flow rate 1 ml/h ($t = [340, 620]$ minutes), the volume increase of the fully carbonated zone was about three times faster than that of the porous zone. Towards the end of the experiment, on the other hand, the porous zone grew the fastest. The *radial* growth rate of the porous zone was approximately equal for the first and second periods of CO_2 flow rate of 1 ml/h (see figure 5.12b). Moreover, the measurements suggest a slight decrease in the radial width of the fully carbonated zone during the second period of flow conditions 1ml/h.

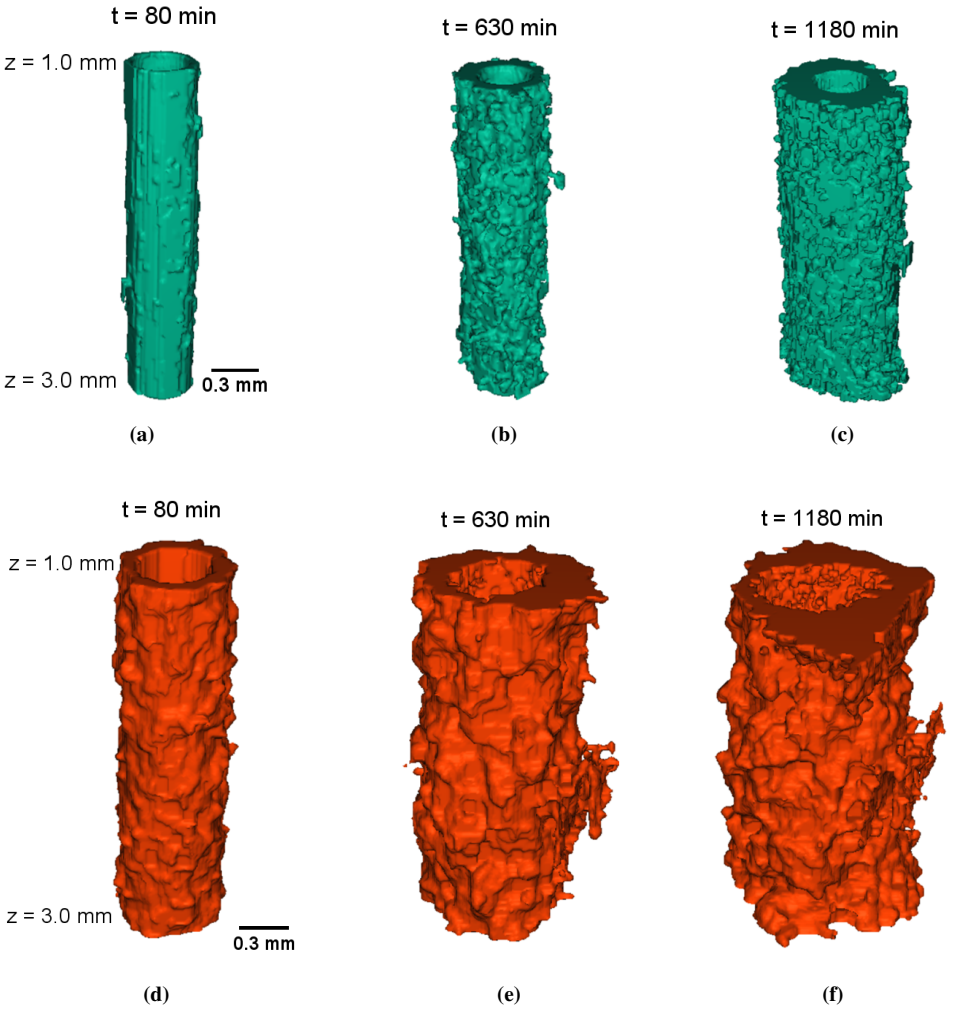

Figure 5.11: 3D rendering of the porous zone for (a) $t = 80$ min, (b) $t = 630$ min and (c) $t = 1180$ min, and of the fully carbonated zone for (d) $t = 80$ min, (e) $t = 630$ min and (f) $t = 1180$ min.

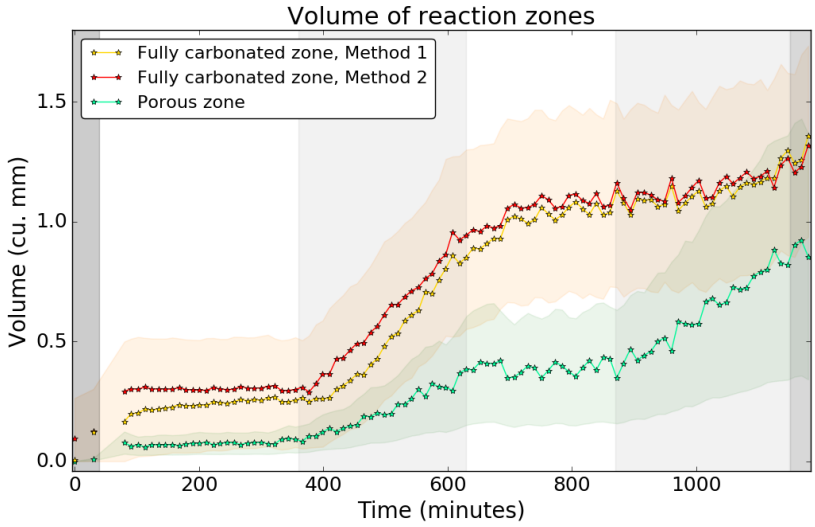

(a)

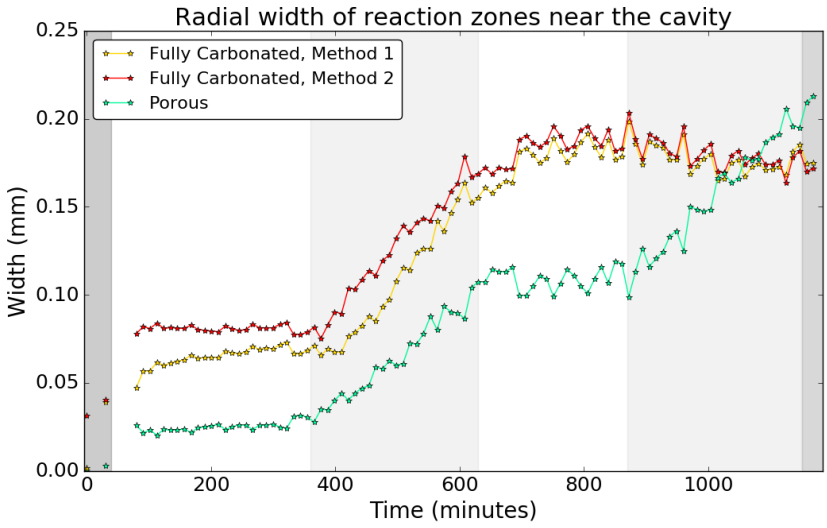

(b)

Figure 5.12: (a) Volume and (b) average radial width of the fully carbonated zone and the porous zone. The fully carbonated zone was evaluated twice based on separate procedures for image processing referred to as Method 1 and Method 2. The estimated worst-case uncertainty is indicated in (a) by orange and green bands for respectively the fully carbonated zone and the porous zone. The colors of the background inform of the CO_2 flow conditions as in previous figures.

5.4 Mechanical deformation of the cement cylinder

5.4.1 The cement cylinder

Figure 5.13 presents the average cylinder *radius* as a function of time. Based on the measurements, the average radius increased by ~ 1 μm between $t = 80$ and $t = 1180$ minutes, which corresponds to an average growth of $\sim 10^{-3}$ μm/min. The worst-case uncertainty of each measurement is estimated to be 1%. This implies that the uncertainty of each measurement is an order of magnitude higher than the measured radius increase.

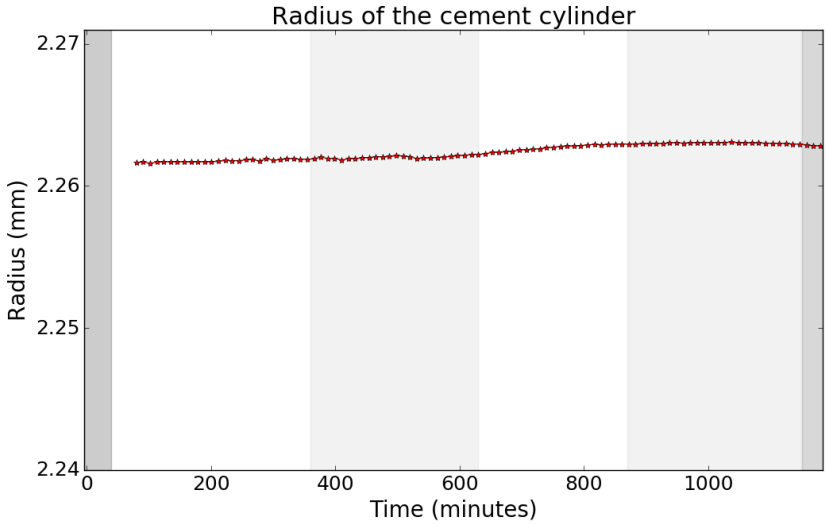

Figure 5.13: The average cement cylinder radius calculated based on the performed segmentation. The worst-case uncertainty of each measurement is estimated to be 1% of the measurement value. The colors of the background inform of the CO_2 flow conditions as stated previously in this chapter. No measurements are included during the first 80 minutes, as the cylinder moved slightly along the z-direction during this period, giving rise to an additional error.

Figure 5.14 presents the *area* of cylinder cross-sections for $t = 80$ minutes and $t = 1180$ minutes. The cylinder ends ($\Delta z \sim 0.5$ mm) are not included in the figure. The measurements suggest that the cylinder cross-sections located in the middle part of the cylinder increased slightly during the experiment. The worst-case uncertainty is estimated to be $\sim 2\%$.

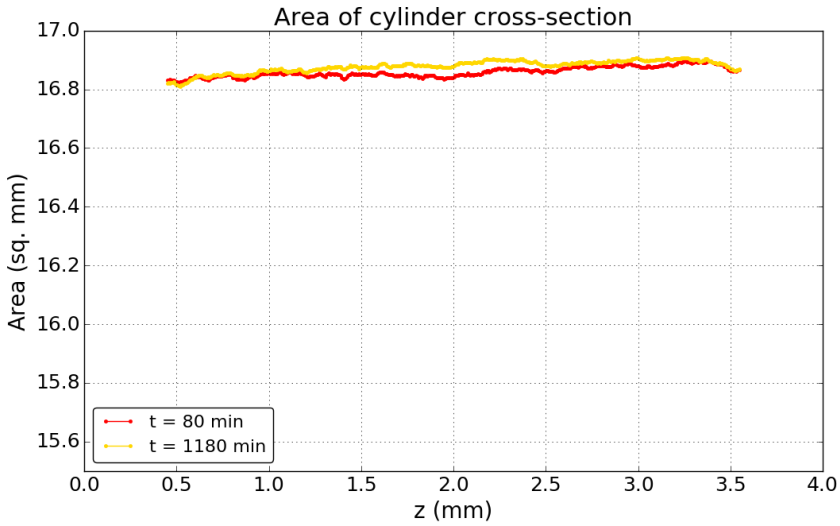

Figure 5.14: The measured area of cylinder cross-sections for $t = 80$ minutes and $t = 1180$ minutes. The worst-case uncertainty of the measurements is estimated to be $\sim 2\%$.

5.4.2 The cylindrical cavity

Figure 5.15 illustrates which voxels that were labeled as part of the cylindrical cavity for the reconstructed slice image located at $z = 2.5$ mm and $t = 1180$ minutes. The average cavity radius as a function of time obtained from the image segmentation is displayed in figure 5.16. The worst-case uncertainty of each measurement is estimated to be $\sim 8\%$. The results to do not indicate neither a significant radius expansion nor reduction.

5.4.3 Movement of cement grains

The movement along the z-direction for a selection of cement grains was measured as described in section 4.3.3. The result is visualized in figure 5.17. The length of an arrow, excluding the arrowhead, corresponds to the translation of a grain between $t = 80$ minutes and $t = 1180$ minutes multiplied by a factor of ten. The trend is that grains in the upper part of the cement cylinder slightly translate upwards, whereas grains in the lower part of the cylinder slightly move downwards.

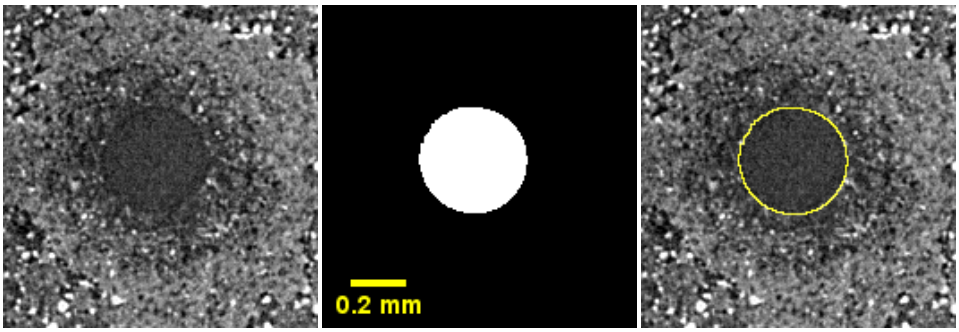

(a) (b) (c)

Figure 5.15: (a) Reconstructed CT slice image at $z = 2.5$ mm for $t = 1180$ minutes. (b) Result of the segmentation. (c) The outline of (b) added to (a) with the purpose of visualizing which voxels that were labeled as part of the cavity.

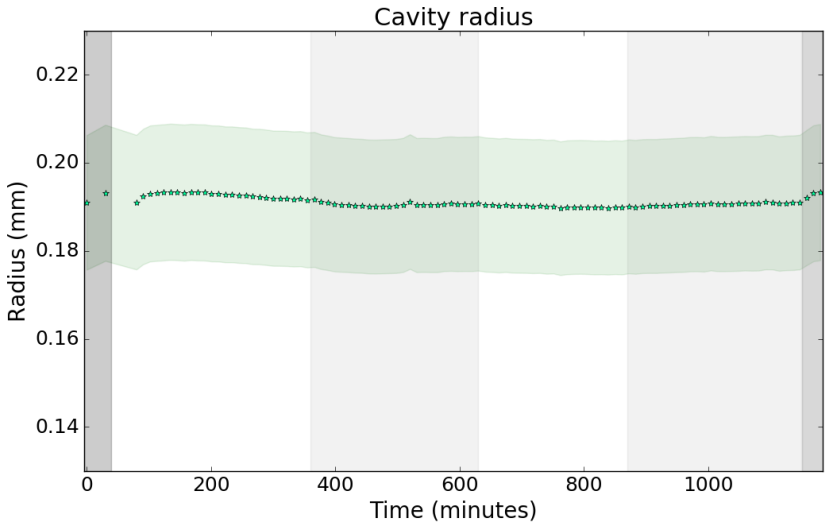

Figure 5.16: The measured average radius of the cylindrical cavity. The worst-case uncertainty is shown by the green band. It is estimated to be $\sim 8\%$. The colors of the background inform of the CO_2 flow conditions as stated previously in this chapter.

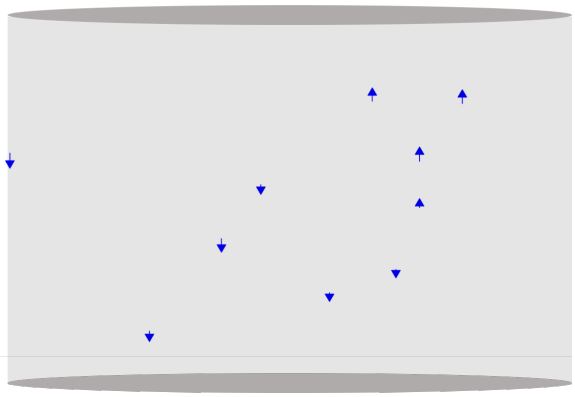

Figure 5.17: Visualization of the movement of cement grains in the z-direction between $t = 80$ min and $t = 1180$ min. The length of an arrow, excluding the arrowhead, corresponds to the translation of the grain multiplied by a factor of ten.

Chapter 6

Discussion

6.1 Segmentation errors

Due to the spatial resolution of the CT images being limited and the contrast between substances of similar density being low, errors are related to the performed segmentation. In Chapter 5, an estimation of the *worst-case uncertainty* is presented for each of the measured quantities[1]. The error related to segmentation is dependent both on subjective evaluations and on systematic and random mislabeling of voxels. The choice of method for image segmentation will thus affect the number of voxels included in a segmented region. In the following, the performed segmentation is briefly evaluated.

The segmentation of precipitated calcium carbonate in the cylindrical cavity was performed by intensity thresholding (see section 4.1). The threshold used to obtain the volume series of $CaCO_3$ presented in section 5.2 is referred to as Threshold 1 in the following. Figure 6.1 illustrates how the choice of intensity threshold affects the resulting volume measurements. By modifying Threshold 1 by $\pm 3\%$, the volume series shown in blue and yellow color are obtained (referred to as respectively Threshold 2 and Threshold 3). The figure demonstrates that the *evolution* of the volume of calcium carbonate as a function of time to little degree is affected by whether Threshold 1, Threshold 2 or Threshold 3 is applied. Moreover, the figure reflects that the image segmentation is prone to systematic errors that slightly "translate" the measurement series along the volumetric axis.

The volume of reacted cement near the cylindrical cavity is obtained using two different methods for image processing (see section 4.2), referred to as Method 1 and Method 2. Figure 5.9 displays the corresponding volume measurements as a function of time. The volumetric evolution obtained with each of the two methods is similar. However, the volume measured by Method 2 is generally greater than that obtained by Method 1 for the

[1] See section 4.4 for information about how the uncertainty is estimated.

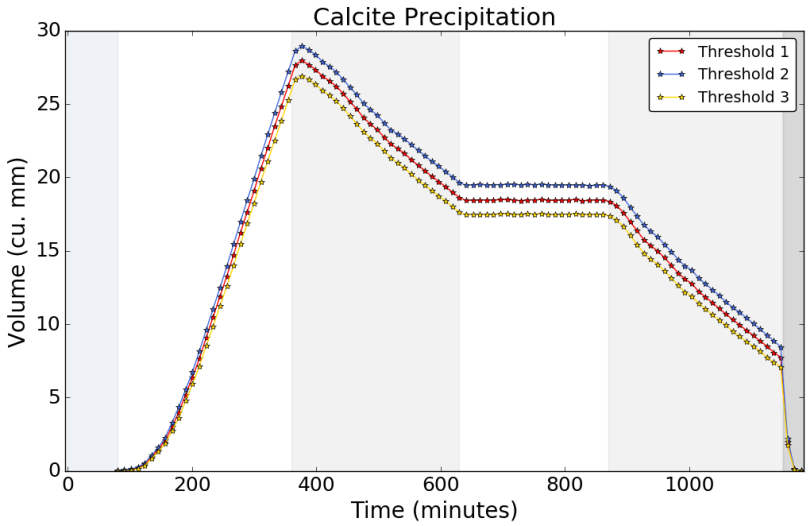

Figure 6.1: The volume of precipitated calcium carbonate in the cylindrical cavity as a function of time obtained using three different intensity thresholds for image segmentation. The threshold that is considered to give the most correct segmentation based on a visual comparison between the original and segmented images is Threshold 1. Thresholds 2 and 3 deviate from Threshold 1 by respectively -3% and $+3\%$.

most of the experiment, which indicates that Method 2 has a tendency to label more voxels as reacted cement than Method 1 has.

Regarding the segmentation of the porous zone only, additional uncertainty is caused by the transition between the porous and fully carbonate zones being rather gradual. Consequently, systematic errors are related to the choice of cement density required for the cement to be labeled as *porous*. Moreover, as shown in figure 5.12, the curve corresponding to the measured temporal evolution of the porous zone is less *smooth* than that of the combined volume of the porous and fully carbonated zones (see figure 5.9). This may indicate that the stochastic error of each measurement is larger for the measurement series of the porous zone than it is for the combined volume of the two zones. Even so, the results from the segmentation show a clear tendency in the temporal evolution as a function of flow conditions.

It was found challenging to consistently segment the cylindrical cavity since the density of the surrounding cement changed during the experiment. As the porous zone grew to dominate the cement enclosing the cylindrical cavity, the contrast between the cylindrical cavity and the cement became reduced. Further complications were caused by the growth and dissolution of calcium carbonate crystals within the cavity.

The uncertainty related to the segmentation of the cement cylinder is lower than that of the cylindrical cavity, mainly because the contrast between the rubber and the anhydrous ce-

ment phases is higher than that between the cavity and the porous zone. There is, however, errors related to the performed segmentation of the cement cylinder, primarily attributed to the limited spatial resolution of the experiment and the contrast between the rubber and the C-S-H being rather poor.

Despite the worst-case error being relatively high for the performed segmentation, it is believed that the *evolution* of the volume measurements give valuable insight into the dynamics of the process of cement carbonation. As illustrated by figure 6.1, the volume measurement series may be ”shifted” along the volumetric axis depending on the choice of parameters. Thus, the measured *temporal evolution* may represent the ”true” evolution despite the error of each measurement being relatively high.

6.2 Analysis of the results

6.2.1 Reacted cement

Based on previous studies, it is expected that reaction zones form in the cement near CO_2–cement interfaces [6, 9, 14, 17, 22]. In the μ-CT images analyzed in this thesis, two reaction zones are clearly visible (the fully carbonated zone and the porous zone), and a thin region adjacent the unreacted cement may be interpreted as a third reaction zone (the portlandite depleted zone). Based on a previous experiment conducted by Chavez Panduro et al., it is anticipated that the portlandite depleted zone is difficult to detect in in-situ μ-CT [14]. Chavez Panduro et al. did not observe the portlandite depleted zone in the CT images. However, alongside Kutchko et al., Mason et al., and Huerta et al., Chavez Panduro et. al. observed the reaction zone using scanning electron microscopy (SEM) [6, 9, 14, 22].

Figure 5.1 illustrates that the radial growth rate of the reaction zones surrounding the cylindrical cavity depends on the angular position. Similar observations were made by Chavez Panduro et al. [66]. The non-isotropic growth of cement near CO_2 leakage pathways may be explained by the cement being a heterogeneous material, meaning that the porosity and chemical composition is a function of the spatial location.

The experimental results show that the rate of cement degradation depends on the CO_2 flow conditions. As illustrated by figure 5.7, the combined volume of the porous and fully carbonated zones increased much more rapidly during flow conditions than during static conditions. This is in accordance with previous studies: A rapid cement alteration has been observed for experiments using flow conditions [9, 15, 34], and a limited degradation has been observed for experiments with no CO_2 flow [6, 70]. It should however be noted that there are exceptions not fitting into this pattern, for instance an experiment conducted by Barlet-Gouédard et al., in which the cement was altered quickly despite static CO_2 conditions [71]. Kutchko et al. address this, and propose that short cement curing time and high curing and experimental temperatures are to blame [6]. According to Carroll et al., the width of the reaction zones is a function of the duration of CO_2 exposure, the conditions of the experiment, including CO_2 flow rate, temperature and pressure, and the

cement composition [72]. The complexity of the conditions determining the alteration of cement may complicate the comparison of experiments.

The CO_2 flow conditions are important for the rate of cement degradation because they determine both the renewal of carbonic acid and the removal of products from the cement carbonation reactions [72]. Confirmed by experiments by Huerta et al. and simulations by Chavez Panduro et al., the effluent pH is dependent on the fluid flow rate [19, 66]; for closed systems and systems with a slow renewal of CO_2, the effluent pH is higher than in the case of open systems. This affects the transport of CO_2 into the cement. According to Iyer et al., the cement carbonation is transport-limited, unless the reacted cement layers are "sufficiently" thin[2] [73]. In the regime of transport-control, the rate of diffusion or advection of CO_2 into the cement is crucial for the rate of cement degradation. Moreover, the transport of reactants into the cement may be dominated by advection in the case of flow conditions [7], which may allow for a further enhanced cement carbonation. In the case of nonflow conditions, on the other hand, the transport of reactants into the cement is diffusion-limited [7, 13].

The growth of reacted cement is observed to be faster for the first than for the second period of flow rate 1 ml/h (see figure 5.7). Furthermore, during the first period of flow 1 ml/h, the volumetric growth rate decreased. Previous studies support that the cement degradation may slow down with time [6, 72]. Kutchko and co-workers explained this by a change in the properties of the cement in the course of their experiment, caused by the growth of the dense fully carbonated zone. The hypothesis is supported by research by Duguid et al., who observed that the cement alteration became slower once the fully carbonated zone formed [15].

Figure 5.12 shows that the growth of the fully carbonated zone slows down after static conditions have been re-introduced to the system at $t = 620$ minutes. When static conditions are applied, the transport of reactants into the cement slows down. However, as the diffusion of ions is an on-going process, it is reasonable that H^+, H_2CO_3 and free calcium ions present inside the cement will retain the expansion of the fully carbonated zone for a period, before the growth slows down.

The radial expansion of the porous zone near the cylindrical cavity is approximately the same during the first and second periods of flow rate 1 ml/h. As the growth of the porous zone is contingent on ion transportation through the porous zone only, and not through the dense fully carbonated zone, the result is reasonable. In a study conducted by Duguid et al., it was concluded that the growth of the porous zone is controlled by the leaching rate of calcium carbonate from the fully carbonated zone, and not by the diffusion of ions through the porous zone [15]. During the periods of no CO_2 flow, the volume of the porous zone was measured to be approximately constant. This indicates that the pH and/or ionic concentrations of the fluid to little degree permitted dissolution of calcium carbonate from the fully carbonated zone. Supported by pH simulations carried out by Chavez Panduro et al., the effluent pH remains high for closed systems (i.e. systems with a negligible renewal of CO_2) [66], which hinders dissolution of calcium carbonate and thus an expansion of the porous zone.

[2] See section 6.2.2 or Ref. [73] for more information about this topic.

6.2.2 Precipitation of $CaCO_3$ in the cylindrical cavity

In the course of the experiment, calcium carbonate both precipitates in and re-dissolves from the CO_2 leakage path. The results suggest that fracture *self-healing* followed by *re-opening* is observed. Self-healing implies that the permeability of the leakage path is reduced, whereas fracture opening refers to a permeability rise [72]. The conditions leading to fracture healing versus fracture opening have been investigated in recent studies conducted by Huerta et al., Luquot et al. and Brunet et al. [13, 19, 20, 22]. They conclude that the fracture length, fracture aperture and fluid flow rate are decisive factors for the outcome.

In accordance with what is observed in recent experiments with static or nearly static CO_2 conditions [14, 19, 22], $CaCO_3$ crystals grew in the cavity during the first period of static CO_2 conditions. However, as seen in figure 5.4, the growth of calcium carbonate crystals did not begin immediately after static CO_2 conditions were introduced. This may be explained by the short period of rapid CO_2 flow that was applied before $t = 40$ minutes. For precipitation of calcium carbonate to occur, the pH and ion concentrations must allow for the fluid to become over-saturated. However, due to the quick renewal of acid solution during the CO_2 flow conditions, the pH and the concentrations of calcium and carbonate ions are believed to have been low upon the introduction of static conditions. According to Carroll et al., ions are continuously being washed out of the system in the case of flow conditions [72]. Moreover, constant renewal of carbonic acid leads to the effluent pH remaining low[3]. Thus, an 'incubation period' may have been required for the cavity fluid to become over-saturated after the introduction of static CO_2 conditions.

In the time period $t \sim [180, 340]$ minutes, the volume of the precipitated calcium carbonate in the cavity increased approximately linearly as a function of time. The growth of crystals may be limited by the availability of ions and/or reactions occurring on the crystal surface [74]. If the crystal growth had been purely surface reaction controlled, it should be expected that the volumetric crystal growth rate would increase with time. Thus, the obtained results may indicate that the growth of calcium carbonate is not purely controlled by surface reactions, and it is believed that the availability of calcium ions and/or carbonate ions in the cavity fluid influences the crystal growth rate. In order to create a model predicting the concentrations of ions diffusing into the cavity, coupled processes should be taken into account. A model describing the transport of calcium ions into the cavity would have to capture the spatial and temporal concentration distribution of calcium ions in the cement, which depends on the coupling between diffusion of carbonic acid into the cement and the dissolution and precipitation of calcium-containing solid phases. Moreover, the growth of the cement reaction zones led to a change in the cement permeability which should be included in the model. Due to time constraints, an attempt has not been made to develop a model predicting the concentration of calcium ions diffusing into the cavity. A simple consideration is however presented in the following. Assume that $V_{\mathrm{diffusion}}(t)$ refers to the volume of cement surrounding the cavity that is likely to contain calcium ions that may reach the cavity at time t. $V_{\mathrm{diffusion}}(t)$ may be expressed as

[3] Simulations by Chavez Panduro et al. and experiments by Huerta et al. suggest that the effluent pH remains low for systems with a rapid renewal of dissolved CO_2 [19, 66].

$$V_{\text{diffusion}}(t) = h\pi\Big(r^2_{\text{diffusion}}(t) - r^2_{\text{cavity}}\Big), \tag{6.1}$$

with h as the height of the cavity, $r_{\text{diffusion}}(t)$ as the radius of the disk in the (x, y)-plane with calcium ions that may reach the cavity at time t, and r_{cavity} as the radius of the cavity. $r = 0$ is defined to be in the center of the cavity in the (x, y)-plane. $r^2_{\text{diffusion}}(t)$ increases with time; the diffusion distance is proportional to the square root of time according to diffusion theory [75]. Based on this simplified model, $V_{\text{diffusion}}(t)$ increases linearly in t. Thus, despite the average distance the calcium ions must travel to reach the cavity increases as a function of time, so does the volume from which the ions may "originate".

In the second period of static conditions, no change in the amount of precipitated $CaCO_3$ was detected (see figure 5.4). Precipitation or dissolution may still have occurred, but with an insufficient reaction velocity for it to be measured in the given experiment. In the following, an explanation is proposed for why precipitation of calcium carbonate is observed in the first period of static conditions, but not in the second one. The proposed explanation is based on a reaction model developed by Iyer and co-workers [73]. According to Iyer et al., the width of the cement reaction zones determine whether the growth of the fully carbonated zone is reaction-limited or diffusion-limited [73]. If the reaction zones are thin, as is common in the case of no CO_2 flow and/or a short exposure period, the dissolution or precipitation reactions limit the growth of the fully carbonated zone. Consequently, calcium ions may diffuse into the cavity, causing the fluid to become over-saturated, which leads to calcium carbonate precipitation in the CO_2 leakage pathway. This scenario may describe the situation of the cement sample for the first period of static conditions. When static conditions are re-introduced at $t = 620$ minutes however, the thickness of the fully carbonated and porous zones near the cavity have, according to figure 5.12, increased significantly. Thus, it is reasonable that the growth of the fully carbonated zone is diffusion-controlled. According to the model developed by Iyer and co-workers, the growth of the fully carbonated zone being diffusion-limited leads to the fluid in the cavity not becoming over-saturated, and hence, calcium carbonate precipitation is not observed. Moreover, it is reasonable that if the porous zone had expanded during the second period of no CO_2 flow, calcium ions would diffuse into the cavity, as the permeability of the porous zone is higher than that of the fully carbonated zone [6]. Such a diffusion process would have caused an increase in the saturation index of the cavity fluid. However, as seen in figure 5.12, a growth of the porous zone was not measured for the second period of static CO_2 conditions.

During the periods of CO_2 flow, dissolution of $CaCO_3$ was observed (see figure 5.4). Attributed to the constant renewal of CO_2 to the cavity, the effluent pH remained low and calcium ions were removed [66, 72, 73], causing the system to become under-saturated. The slope of the evolution of calcium carbonate does not seem to depend strongly on the volume or surface area of the calcium carbonate crystals, and this indicates that surface reactions did not limit the dissolution process. Instead, it is proposed that the concentration of calcium ions and the pH of the cavity fluid control the dissolution rate. As seen in figure 5.4, the slope of the volumetric evolution is constant during time periods of alike CO_2 flow conditions (flow rate 1 ml/h). However, when flow rate of 20 ml/h is introduced towards the

end of the experiment, the dissolution rate is increased. When the flow rate is increased, both the concentration of calcium ions and the effluent pH in the cavity are believed to become reduced due to the rapid renewal of CO_2-saturated water.

It is stated in section 5.2 that the precipitation of calcium carbonate crystals was greater in the upper half of the cavity than in the lower half (see figure 5.4). Moreover, according to figure 5.4, the conditions for crystal precipitation were met in the upper half of the cavity before they were met in the lower half. A hypothesis to explain the differences in $CaCO_3$ precipitation between the upper and lower halves of the cavity is presented in the following. The hypothesis involves that the direction of the flow applied prior to the static conditions caused the concentration of calcium ions in the cement to be dependent on z. The calcium carbonate precipitation occurred in the first interval of static conditions, prior to which the cavity was subjected to a rapid CO_2 flow coming from above the cylinder. Considering that the cement degradation may be advection-driven in the case of CO_2 flow conditions [7], the flow direction may have caused the concentration of free calcium ions in the cement to be boosted near the top surface of the cylinder. Calcium ions are believed to diffuse into the cavity also after the introduction of static CO_2 conditions. Thus, assuming that the amount of calcium ions released in the cement depended on z, it is suggested that also the concentration of calcium ions inside the cavity depended on z. A difference in the concentration of calcium ions between the upper land lower halves of the cavity may have led to the fluid becoming over-saturated in the upper half of the cavity before it became over-saturated in the lower half of the cavity.

As to why the precipitation of calcium carbonate was not uniform along the cavity walls in the (x, y)-plane (see figure 5.3), it is believed that the heterogeneity of the cement surrounding the cavity may be of importance. As illustrated by figure 5.1, the growth of reacted cement about the cavity depended on the angular position. The proposed explanation for the non-isotropic growth (see section 6.2.1) was related to the porosity and/or chemical composition of cement being a function of spatial location[4]. Considering that the growth of the reaction zones surrounding the cavity depended on the angular position, it may be reasonable that also the transport of calcium ions into the cavity depended on the angular position. Moreover, the availability of calcium ions along the cavity wall may have affected the locations at which calcium carbonate crystals formed.

Figure 6.2 is a schematic illustration of the process of $CaCO_3$ precipitation and re-dissolution as proposed in this chapter. Calcium carbonate precipitated during the first period of static conditions (labeled 2 in the figure), and re-dissolved when flow conditions were applied (labeled 3, 5 and 6 in the figure). Moreover, the figure illustrates that H^+ ions (black disks) seeped into the cement in the course of the experiment, and that the transport was faster during flow than nonflow conditions. The Ca^+ ions (yellow disks) were released primarily by the dissolution of portlandite and calcium carbonate in the cement.

[4] As stated in Chapter 2, cement is a heterogeneous material [4].

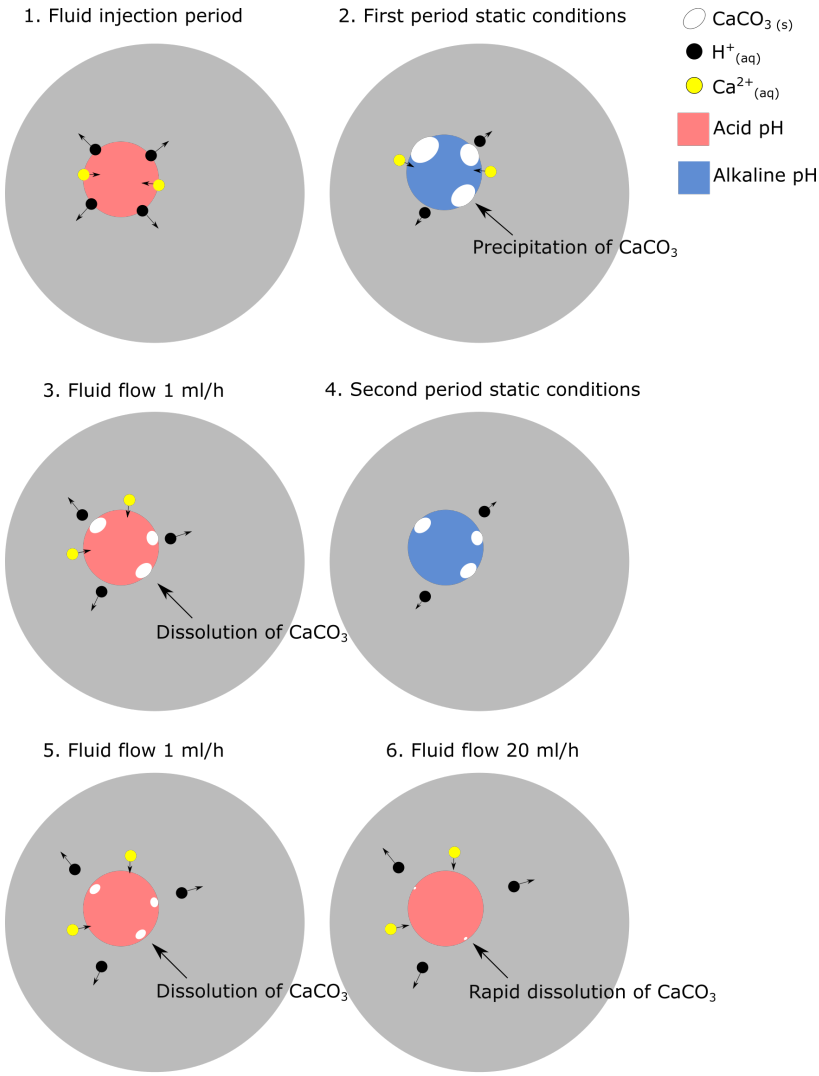

Figure 6.2: Schematic illustration (not to scale) of the process of precipitation and re-dissolution of calcium carbonate in the CO_2 leakage pathway (colored red if acid pH and blue if alkaline pH) based on the series of events proposed in this section. Ca^{2+} is represented by yellow disks, and H^+ is represented by black disks. H^+ ions diffused/flowed into the cement in the course of the experiment. The transport was faster in the case of flow conditions compared to static CO_2 conditions.

6.2.3 Mechanical deformation of the sample

The results presented in section 5.4 may suggest that the cement sample may have expanded *slightly* ($\sim \mu$m) during the experiment, both in the radial and longitudinal directions, despite that the cement was subjected to high pressures. It is however possible that the measured cross-sectional expansion of the cylinder was evoked by time-dependent segmentation errors, despite the cause of such errors not being clear. The results do not indicate a change in the radius of the cylindrical cavity. However, due to the carbonation processes happening inside and adjacent to the cavity, it is likely that time dependent segmentation errors have occurred. Based on this, it is possible that the radius of the cavity in fact changed in the course of the experiment, but that this was not detected due to measurement errors.

According to Carroll et al. and Walsh et al., the formation of reaction zones may lead to deformation of the cement [10, 72]. Walsh et al. investigated the deformation of cement near a cement–caprock interface when exposed to CO_2-rich brine [10]. They found that cement grains were displaced towards the direction of the cement–caprock interface in the course of the experiment, and their analysis indicates that the local strain within the cement was altered due to the carbonation processes. A swelling of cement by the growth of the porous zone is suggested to contribute to the permeability decrease of fractures in experiments conducted by Walsh et al. and Abdoulghafour et al. [10, 34]. The swelling may be caused by the molecular volume of amorphous silicate being greater than that of calcium silica hydrates [10]. However, the growth of the porous zone does not necessarily lead to an expansion of the cement, considering that compounds such as portlandite and C-S-H are dissolved [10]. If a volume expansion of the porous zone occurred for the experiment at hand, it would be reasonable that the radius of the cavity had decreased. It is, however, possible that a reduction in cavity volume was prevented by the CO_2 fluid pressure inside the cavity, or, that it occurred, but was not detected due to uncertainties in the measurements.

The fully carbonated zone is denser than unreacted cement because calcium carbonate occupies a larger volume than portlandite [6, 17, 76]. It is therefore possible that a slight cement expansion is attributed to the formation of the fully carbonated zone. Estimating the volume increase that may be caused by the formation of the fully carbonated zone is however not a trivial matter due to the coupling between chemical and mechanical processes. The calcium carbonate precipitates in the pore space of the cement, implying that the volume of portlandite being replaced by calcium carbonate is not necessarily proportional to the volume occupied by the fully carbonated zone. Moreover, the molar volume of the cement may potentially decrease due to an increase in pressure, and the elastic modulus of the cement is, according to Constantinides and Ulm, reduced upon the leaching of calcium [77].

6.3 Implications for well integrity

A fast cement degradation may compromise the sealing ability of well cement [5]. Even though a moderate carbonation may be advantageous attributed to the low permeability of the fully carbonated zone [5], a continued degradation will leave the cement weak, brittle and porous, due to the growth of the porous zone. Kutchko et al. states that the propagation of cement reaction zones will continue until the cement is completely degraded, as equilibrium is not obtained in the presence of a pH gradient [17]. The study presented demonstrates that the CO_2 flow conditions are decisive for the rate of cement degradation. In the case of CO_2 flow rate of 1 ml/h, a rapid cement carbonation was observed, whereas a relatively slow degradation was seen for static CO_2 conditions. Moreover, in the case of flow conditions, the radial growth rate of the porous zone was found to be approximately constant as a function of time, whereas that of the fully carbonated zone was seen to decrease. This suggests that, in the case of flow conditions, the weak and porous layer may dominate the altered cement over time. When, however, nonflow CO_2 conditions were applied, the volume of the porous zone remained nearly constant. Consequently, the results suggest that the sealing ability of well cement may be contingent on a sufficiently low CO_2 flow rate.

Field studies at the SACROC unit conducted by Carey et al. show a limited cement degradation [5]. Based on the studies, Carey and co-workers suggest that wellbore cement is in general not subjected to fluid flow, except in wells containing continuous gaps along material interfaces. If the hypothesis of Carey and co-workers is correct, the results obtained in this study are promising for the well integrity of properly completed wells, due to the slow degradation observed for static CO_2 conditions.

CO_2 leakage pathways may form along cement–cement, cement–steel or cement–rock interfaces, leading to CO_2 flow induced by a pressure gradient [22, 78]. It is common that continuous openings remain undetected in today's wells, even though they can be several kilometers long [22, 72]. Thus, the CO_2 flow rates of leakage pathways may be crucial for the integrity of CO_2 wells. If the pathway permeability is constant or increasing, the cement adjacent the fracture may experience a rapid degradation over long time periods. Consequently, the sealing ability of the well may become reduced with time. In the performed study, it was demonstrated that cavity self-healing occurred adjacent cement with thin reaction zones, but not adjacent already severely degraded cement. This indicates that self-sealing by calcium carbonate precipitation may not be likely to occur for leakage pathways with an initially high CO_2 flow rate, regardless of whether the flow rate is reduced with time. Moreover, the study shows that precipitated calcium carbonate can re-dissolve if the fluid flow rate in the cavity is increased.

Based on the performed study, it is plausible that cement may swell slightly due to the carbonation process. An expansion is beneficial for the integrity of CO_2 wells, as it may lead to the sealing of cracks and the reduction of cement–steel and cement–rock interface gaps.

An important point is whether the conditions of the experiment represent realistic CO_2 well conditions. According to Huerta et al., the pH of downhole conditions is typically higher

than that of the performed experiment [22]. This may suggest that the cement degradation observed in the experiment is faster than what is expected for CO_2 sequestration sites. Moreover, the flow velocity of subsurface CO_2 is typically slow [7], supporting that the fast cement degradation observed in this experiment may be unlikely to occur in CO_2 wells.

Even though the reactions leading to cement carbonation is understood, the long-term impact of cement degradation for the sealing ability of wells is not [13]. The coupling of chemical processes, mechanical processes and fluid flow makes it difficult to predict how specific systems evolve. According to Carroll et al., more research needs to be done on for instance the influence of chemical reactions on the mechanical properties of cement, and on the stresses that the wellbore cement is subjected to [72]. Long-term consequences for well integrity should therefore not be drawn directly from the results obtained in this work.

6.4 Suggestions for further research

Future research should be performed with the aim of further improving the understanding of risks associated with CO_2 sequestration in depleted oil and gas reservoirs. Suggestions are given in the following.

The work presented demonstrates that in-situ μ-CT with synchrotron radiation is a technique well-suited for investigating the response of cement when exposed to CO_2. In order to obtain further insight into processes that may affect CO_2 well integrity, it is proposed that in-situ μ-CT is applied to study: 1) The importance of factors such as temperature, pressure and cement curing conditions for the dynamics of cement carbonation, 2) Degradation mechanisms occurring at cement-steel and cement–rock interfaces exposed to CO_2, and 3) The effect of normal and shear stresses on cement degradation near CO_2 leakage pathways.

Research may be performed with the aim of obtaining an improved understanding of the results presented in this thesis. In particular, it is suggested that a geochemical model is developed for the precipitation and re-dissolution of calcium carbonate crystals in cement cavities containing CO_2. To the knowledge of the author, a well-founded model relating the process of cement carbonation, CO_2 flow conditions and the rate of growth/dissolution of calcium carbonate crystals is not developed as of today.

As pointed out in section 6.3, further research should be performed on the long-term integrity of CO_2 wells. Considering the complexity of CO_2 reservoirs, long-term studies are crucial for the prediction of CO_2 leakage scenarios. In particular, long-term *field studies* are essential to provide with an improved insight into the coupled mechanisms that the well cement is subjected to, as decisive factors may be excluded in controlled experiments. Moreover, as pointed out by Abdoulghafour et al. [34], long-term studies are required to reveal whether self-sealing of leakage pathways is persistent, or if the precipitated calcium carbonated may re-dissolve for instance by erosion.

According to Huerta et al., it is as of today difficult to detect leakage pathways in completed wells [22]. Thus, it is suggested that research should be devoted to improving methods for CO_2 well monitoring. Moreover, with the purpose of creating well-founded risk assessments, improved models for predicting the CO_2 leakage along wells should be developed. Models exist as of today, but simplifications have been made, such as assigning an overall permeability to the well or treating parameters probabilistically [78].

Lastly, it is proposed that further work is invested in designing improved algorithms for automatic image segmentation of μ-CT images of carbonated cement. Assuming that a number of in-situ μ-CT well cement studies will be conducted in the future, it would be beneficial if a set of segmentation routines could with few adjustments be applied on newly obtained images. One possibility is to make use of machine learning, using μ-CT images from previous experiments as training data.

Chapter 7

Conclusion

Analysis of in-situ μ-CT images has been conducted with the purpose of gaining an improved understanding of the carbonation process of well cement when exposed to CO_2-saturated water at reservoir conditions. The analysis has been performed by means of automatic procedures for image segmentation using *ImageJ Macro* scripts. During the μ-CT experiment, alternating no flow and flow of CO_2-saturated water was applied, and the fluid resided in or flowed through a cylindrical cavity running through the cement sample. The foci of the image analysis has been the precipitation of calcium carbonate in the CO_2 leakage pathway, the propagation of cement reaction zones near cement–CO_2 interfaces and the cross-sectional radii of the cement cylinder and cylindrical cavity.

Crystals of calcium carbonate were seen to grow in the CO_2 leakage pathway during the first period of static CO_2 conditions of the μ-CT experiment. Precipitation was however not observed in the second period of no CO_2 flow. In the case of static CO_2 conditions, it is suggested that the degradation of cement near a CO_2 leakage pathway affects whether precipitation of calcium carbonate may be achieved. Furthermore, during periods of CO_2 flow, the calcium carbonate crystals re-dissolved. The rate of dissolution was approximately constant when CO_2 flow rate 1 ml/h was applied. However, when the flow rate was increased to 20 ml/h towards the end of the experiment, also the rate of dissolution increased. By the end of the experiment, the cavity appeared to by emptied of solid calcium carbonate.

The μ-CT images revealed that reaction zones developed near CO_2–cement interfaces in the course of the experiment. Two layers, identified as the *fully carbonated zone* and the *porous zone* in accordance with the terminology used in previous studies, are clearly visible in the images. The growth of reacted cement was seen to be significantly faster during CO_2 flow conditions compared to static conditions. This observation was expected as it is reasonable that a constant renewal of CO_2-saturated water to the system will enhance the transport of carbonic acid into the cement. Moreover, according to the measurements, the expansion of the fully carbonated zone was more rapid for the first than for the second

period of CO_2 flow rate of 1 ml/h. A suggested explanation is related to the growth of the dense fully carbonated zone reducing the flux of carbonic acid into the cement. Regarding the porous zone, on the other hand, the results indicate that the growth rate is retained in time given a constant (and ”sufficient”) renewal of CO_2 to the system.

The measurements indicate a *slight* expansion of the cement cylinder in the course of the experiment. A suggested explanation is related to the growth of the fully carbonated zone, which is denser than unreacted cement. Regarding the cylindrical cavity, the results indicate neither an increase nor decrease in the cavity radius.

The results of this study may be considered as promising for the integrity of properly completed CO_2 wells. For well cement subjected to static CO_2 conditions, which is expected to be the case for properly completed wells, the results suggest a slow cement carbonation and the possibility of fracture self-healing through precipitation of calcium carbonate. For wells containing continuous openings, however, CO_2 flow conditions may be generated, and a relatively rapid cement degradation may be expected. Moreover, the results indicate that the porous zone, as opposed to the fully carbonated zone, may dominate the reacted cement over time in the case of CO_2 flow conditions, which is unfortunate for the CO_2 well integrity.

The presented study demonstrates that in-situ μ-CT with synchrotron radiation is a technique well-suited for studying the degradation of cement caused by the presence of carbonic acid. It is therefore suggested that this experimental technique is applied for future research related to CO_2 well integrity.

Bibliography

[1] S. Solomon, D. Qin, M. Manning, Z. Chen, M. M., K. Averyt, M. Tignor, and T. Miller, eds. *Contribution of Working Group I to the Fourth Assessment Report of the Intergovernmental Panel on Climate Change*. Cambridge, United Kingdom and New York, NY, USA: Cambridge University Press, 2007.

[2] B. Metz, O. Davidson, H. de Coninck, M. Loos, and L. Meyer, eds. *IPCC Special report on Carbon Dioxide Capture and Storage*. Cambridge: Cambridge University Press for the Intergovernmental Panel on Climate Change, 2005, pp. 1–31.

[3] M. Wigand, J. P. Kaszuba, J. W. Carey, and W. K. Hollis. "Geochemical effects of CO_2 sequestration on fractured wellbore cement at the cement/caprock interface". In: *Chemical Geology* 265.1-2 (2009), pp. 122–133.

[4] A. Lavrov and M. Torsæter. *Physics and Mechanics of Primary Well Cementing*. Springer, 2016, pp. 1–72.

[5] J. W. Carey, M. Wigand, S. J. Chipera, G. WoldeGabriel, R. Pawar, P. C. Lichtner, S. C. Wehner, M. A. Raines, and G. D. Guthrie. "Analysis and performance of oil well cement with 30 years of CO_2 exposure from the SACROC Unit, West Texas, USA". In: *International Journal of Greenhouse Gas Control* 1.1 (2007), pp. 75–85.

[6] B. Kutchko, B. Strazisar, G. Lowry, D. Dzombak, and N. Thaulow. "Rate of CO_2 Attack on Hydrated Class H Well Cement under Geologic Sequestration Conditions". In: *Environmental Science & Technology* 42.16 (2008), pp. 6237–6242.

[7] J. P. L. Brunet, L. Li, Z. T. Karpyn, B. G. Kutchko, B. Strazisar, and G. Bromhal. "Dynamic evolution of cement composition and transport properties under conditions relevant to geological carbon sequestration". In: *Energy and Fuels* 27.8 (2013), pp. 4208–4220.

[8] T. Maintz. "Digital and Medical Image Processing". In: 10 (2005), pp. 1–341.

[9] H. E. Mason, W. L. Du Frane, S. D. Walsh, Z. Dai, S. Charnvanichborikarn, and S. A. Carroll. "Chemical and mechanical properties of wellbore cement altered by CO_2-rich brine using a multianalytical approach". In: *Environmental Science and Technology* 47.3 (2013), pp. 1745–1752.

[10] S. D. Walsh, W. L. Du Frane, H. E. Mason, and S. A. Carroll. “Permeability of wellbore-cement fractures following degradation by carbonated brine”. In: *Rock Mechanics and Rock Engineering* 46.3 (2013), pp. 455–464.

[11] A. Duguid and G. W. Scherer. “Degradation of oilwell cement due to exposure to carbonated brine”. In: *International Journal of Greenhouse Gas Control* 4.3 (2010), pp. 546–560.

[12] G. W. Scherer, B. Kutchko, N. Thaulow, A. Duguid, and B. Mook. “Characterization of cement from a well at Teapot Dome Oil Field: Implications for geological sequestration”. In: *International Journal of Greenhouse Gas Control* 5.1 (2011), pp. 115–124.

[13] J. P. L. Brunet, L. Li, Z. T. Karpyn, and N. J. Huerta. “Fracture opening or self-sealing: Critical residence time as a unifying parameter for cement-CO_2-brine interactions”. In: *International Journal of Greenhouse Gas Control* 47 (2016), pp. 25–37.

[14] E. A. Chavez Panduro, M. Torsæter, K. Gawel, R. Bjørge, A. Gibaud, Y. Yang, S. Bruns, Y. Zheng, H. O. Sørensen, and D. W. Breiby. “In-Situ X-ray Tomography Study of Cement Exposed to CO_2 Saturated Brine”. In: *Environmental Science and Technology* 51.16 (2017), pp. 9344–9351.

[15] A. Duguid, M. Radonjic, and G. Scherer. “Degradation of Well Cements Exposed to Carbonated Brine”. In: *Fourth Annual Conference on Carbon Capture and Sequestration* May (2005), pp. 1–12.

[16] T. K. T. Wolterbeek and A. Raoof. “Meter-Scale Reactive Transport Modeling of CO_2-Rich Fluid Flow along Debonded Wellbore Casing-Cement Interfaces”. In: *Environmental Science & Technology* (2018).

[17] B. G. Kutchko, B. R. Strazisar, D. A. Dzombak, G. V. Lowry, and N. Thauiow. “Degradation of well cement by CO_2 under geologic sequestration conditions”. In: *Environmental Science and Technology* 41.13 (2007), pp. 4787–4792.

[18] P. Cao, Z. T. Karpyn, and L. Li. “Dynamic alterations in wellbore cement integrity due to geochemical reactions in CO_2-rich environments”. In: *Water Resources Research* 49.7 (2013), pp. 4465–4475.

[19] N. J. Huerta, M. A. Hesse, S. L. Bryant, B. R. Strazisar, and C. L. Lopano. “Experimental evidence for self-limiting reactive flow through a fractured cement core: Implications for time-dependent wellbore leakage”. In: *Environmental Science and Technology* 47.1 (2013), pp. 269–275.

[20] L. Luquot, H. Abdoulghafour, and P. Gouze. “Hydro-dynamically controlled alteration of fractured Portland cements flowed by CO_2-rich brine”. In: *International Journal of Greenhouse Gas Control* 16 (2013), pp. 167–179.

[21] W. Crow, J. W. Carey, S. Gasda, D. Brian Williams, and M. Celia. “Wellbore integrity analysis of a natural CO_2 producer”. In: *International Journal of Greenhouse Gas Control* 4.2 (2010), pp. 186–197.

[22] N. J. Huerta, M. A. Hesse, S. L. Bryant, B. R. Strazisar, and C. Lopano. “International Journal of Greenhouse Gas Control Reactive transport of CO_2 -saturated water in a cement fracture : Application to wellbore leakage during geologic CO_2 storage”. In: 44 (2016), pp. 276–289.

[23] S. Q. Yang, P. G. Ranjith, and Y. L. Gui. “Experimental study of mechanical behavior and X-ray micro CT observations of sandstone under conventional triaxial compression”. In: *Geotechnical Testing Journal* 38.2 (2015), pp. 179–197.

[24] A. Thompson, J. Llacer, L. Campbell Finman, E. Hughes, J. Otis, S. Wilson, and H. Zeman. “Computed tomography using synchrotron radiation”. In: *Nuclear Instruments and Methods in Physics Research* 222.1-2 (1984), pp. 319–323.

[25] I. Børve. “Analysis of micro-CT images of a fractured well cement cylinder exposed to CO_2-brine under high temperature and pressure”. 2017 (Unpublished).

[26] Z. Li, M. Dong, S. Li, and S. Huang. “CO_2 sequestration in depleted oil and gas reservoirs-caprock characterization and storage capacity”. In: *Energy Conversion and Management* 47.11-12 (2006), pp. 1372–1382.

[27] C. M. White, B. R. Strazisar, E. J. Granite, J. S. Hoffman, and H. W. Pennline. “Separation and capture of CO_2 from large stationary sources and sequestration in geological formationscoalbeds and deep saline aquifers”. In: *Journal of the Air and Waste Management Association* 53.6 (2003), pp. 645–715.

[28] European Committe for Standardization. *EN 197-1: Cement - Part 1: Composition, specifications and conformity criteria for common cements*. 2000.

[29] M. Zhang and A. P. Jivkov. “Microstructure-informed modelling of damage evolution in cement paste”. In: *Construction and Building Materials* 66 (2014), pp. 731–742.

[30] A. Neville. *Properties of Concrete*. 5th. Essex, England: Pearson, 2011, pp. 1–100.

[31] S. Bachu. “CO_2 storage in geological media: Role, means, status and barriers to deployment”. In: *Progress in Energy and Combustion Science* 34.2 (2008), pp. 254–273.

[32] J. Rutqvist. “The geomechanics of CO_2 storage in deep sedimentary formations”. In: *Geotechnical and Geological Engineering* 30.3 (2012), pp. 525–551.

[33] S. E. Manahan. *Water Chemistry*. CRC Press, Taylor & Francis Group, 2011, pp. 52–55.

[34] H. Abdoulghafour, L. Luquot, and P. Gouze. “Characterization of the mechanisms controlling the permeability changes of fractured cements flowed through by CO_2-rich brine”. In: *Environmental Science and Technology* 47.18 (2013), pp. 10332–10338.

[35] D. J. Brenner and E. J. Hall. “Computed tomography - An increasing source of radiation exposure”. In: *The New England Journal of Medicine* 357.22 (2007), pp. 2277–2284.

[36] J. Als-Nielsen and D. McMorrow. *Elements of Modern X-ray physics*. 2nd Editio. Chichester, United Kingdom: John Wiley & Sons, Ltd, 2011, pp. 75, 305–310.

[37] B. Weon, J. H. Je, Y. Hwu, and G. Margaritondo. “Phase contrast X-ray imaging Byung”. In: *International Journal of Nanotechnology* 3 (2006), pp. 280–297.

[38] J. T. Bushberg, J. A. Seibert, E. M. Leidholdt jr., and J. M. Boone. *The Essential Physics of Medical Imaging*. Ed. by C. W. Mitchell. 3rd Editio. Philedelphia: Lippincott Williams & Wilkins, a Woltzer Kluwer Business, 2012, pp. 33–60.

[39] A. Burvall, U. Lundström, P. A. C Takman, D. H. Larsson, and H. M. Hertz. “Phase retrieval in X-ray phase-contrast imaging suitable for tomography”. In: *Optics Express* 19.11 (2011), pp. 10359–10376.

[40] J. Lilley. *Nuclear Physics: Principles and Applications*. Ed. by D. J. Sandiford, F. Mandl, and A. C. Phillips. 1st. Chichester: John Wiley & Sons Ltd, 2001, pp. 232–245.
[41] D. Paganin, S. C. Mayo, T. E. Gureyev, P. R. Miller, and S. W. Wilkins. "Simultaneous phase and amplitude extraction from a single defocused image of a homogeneous object". In: *Journal of Microscopy* 206.1 (2002), pp. 33–40.
[42] L. Yu and S. Leng. "Image Reconstruction Techniques". 2016.
[43] G. W. Collins, II. *The Foundations of Celestial Mechanics*. Case Western Reserve University, 2004, pp. 24–25.
[44] M. A. Flower, ed. *Webb's physics of medical imaging*. 2nd Editio. Boca Raton: CRC Press, Taylor & Francis Group, 2012, pp. 97–153.
[45] A. C. Kak and M. Slaney. *Principles of Computerized Tomographic Imaging*. IEEE Press, 1988, pp. 58–70.
[46] D. L. Pham, C. Xu, and J. L. Prince. "Current Methods in Medical Image Segmentation". In: *Annual Review of Biomedical Engineering* 2 (2000), pp. 315–337.
[47] M. Bhat. "Digital Image Processing". In: *International Journal of Scientific & Technology Research* 3.1 (2014), pp. 272–276.
[48] M. Petrou and C. Petrou. *Image Processing: The Fundamentals*. 2nd Editio. John Wiley & Sons Ltd, 2010, pp. 550–560.
[49] MathWorks. *Enhancement Methods in Image Processing*. 2018.
[50] J. Schindelin et al. "Fiji: an open-source platform for biological-image analysis". In: *Nature Methods* 9.7 (2012), pp. 676–682.
[51] G. Gupta. "Algorithm for Image Processing Using Improved Median Filter and Comparison of Mean, Median and Improved Median Filter". In: *International Journal of Soft Computing and Engineering* 1.5 (2011), pp. 304–311.
[52] P. Bakker, L. van Vliet, and P. Verbeek. "Edge preserving orientation adaptive filtering". In: *IEEE Computer Society Conference on Computer Vision and Pattern Recognition* (1999), pp. 535–540.
[53] R. Fisher, S. Perkins, A. Walker, and E. Wolfart. *Gaussian Smoothing*. 2003.
[54] G. Papari, N. Petkov, and P. Campisi. "Artistic edge and corner enhancing smoothing". In: *IEEE Transactions on Image Processing* 16.10 (2007), pp. 2449–2462.
[55] R. L. Easton. "Fundamentals of Digital Image Processing". In: November (2010), p. 216.
[56] S. R. Sternberg. "Biomedical Image Processing". In: *Computer* 16.1 (1983), pp. 22–34.
[57] R. M. Haralick, S. R. Sternberg, and X. Zhuang. "Image Analysis Using Mathematical Morphology". In: *IEEE Transactions on Pattern Analysis and Machine Intelligence* 9.4 (1987), pp. 532–550.
[58] C. A. Glasbey and G. W. Horgan. *Image Analysis for the Biological Sciences*. Chichester: Wiley, 1995.
[59] K. Somasundaram and T. Kalaiselvi. "A Method for Filling Holes in Objects of Medical Images Using Region Labeling and Run Length Encoding Schemes". In: *Image Processing* Ncimp (2010), pp. 110–115.
[60] C. Stover and E. W. Weisstein. *Set*. 2018.

[61] N. R. Pal and S. K. Pal. “A review on image segmentation techniques”. In: *Pattern Recognition* 26.9 (1993), pp. 1277–1294.
[62] R. M. Haralick and L. G. Shapiro. “Image segmentation techniques”. In: *Computer Vision, Graphics, and Image Processing* 29.1 (1985), pp. 100–132.
[63] T. Rohlfing, R. Brandt, R. Menzel, D. B. Russakoff, and C. R. Maurer Jr. “Quo Vadis, Atlas-Based Segmentation?” In: *Handbook of Biomedical Image Analysis, Volume III: Registration Models*. Ed. by J. Suri, D. Wilson, and S. Laxminarayan. 2005. Chap. 11, pp. 435–476.
[64] R. Nock and F. Nielsen. “Statistical region merging”. In: *IEEE Transactions on Pattern Analysis and Machine Intelligence* 26.11 (2004), pp. 1452–1458.
[65] C. Rueden. *Statistical Region Merging*. 2017.
[66] E. A. Chavez Panduro, M. Torsæter, K. Gawel, R. Bjørge, A. Gibaud, Y. Yang, H. O. Sørensen, P. Frykman, C. Kjøller, and D. W. Breiby. “Closing of micro-cavities in well cement upon exposure to CO_2 brine”. In: *Energy Procedia* 114.1876 (2017), pp. 5100–5108.
[67] F. Renard, B. Cordonnier, D. K. Dysthe, E. Boller, P. Tafforeau, and A. Rack. “A deformation rig for synchrotron microtomography studies of geomaterials under conditions down to 10 km depth in the Earth”. In: *Journal of Synchrotron Radiation* 23.4 (2016), pp. 1030–1034.
[68] W. S. Rasband. *ImageJ*. Maryland, USA, 2016.
[69] L. Fabbiano, N. Giaquinto, M. Savino, and G. Vacca. “Observations on the worst case uncertainty”. In: *Journal of Physics: Conference Series* 459.1 (2013).
[70] J. W. Carey, R. Svec, R. Grigg, J. Zhang, and W. Crow. “Experimental investigation of wellbore integrity and CO_2-brine flow along the casing-cement microannulus”. In: *International Journal of Greenhouse Gas Control* 4.2 (2010), pp. 272–282.
[71] V. Barlet-Gouédard, G. Rimmelé, B. Goffé, and O. Porcherie. “Mitigation strategies for the risk of CO_2 migration through wellbores”. In: February (2006), pp. 21–23.
[72] S. Carroll, J. W. Carey, D. Dzombak, N. J. Huerta, L. Li, T. Richard, W. Um, S. D. Walsh, and L. Zhang. “Review: Role of chemistry, mechanics, and transport on well integrity in CO_2 storage environments”. In: *International Journal of Greenhouse Gas Control* 49 (2016), pp. 149–160.
[73] J. Iyer, S. D. Walsh, Y. Hao, and S. A. Carroll. “Incorporating reaction-rate dependence in reaction-front models of wellbore-cement/carbonated-brine systems”. In: *International Journal of Greenhouse Gas Control* 59 (2017), pp. 160–171.
[74] L. Brecevic and D. Kralj. “On Calcium Carbonates : from Fundamental Research to Application”. In: *Croatica Chemica Acta* 80 (2007), pp. 467–484.
[75] G. I. Taylor. “Diffusion by continuous movement”. In: *Proceedings of the London Mathematical Society* s2-20.1,1 (1922), pp. 196–212.
[76] K. You, H. Jeong, and W. Hyung. “Effects of Accelerated Carbonation on Physical Properties of Mortar”. In: *Journal of Asian Architecture and Building Engineering* 13.1 (2014), pp. 217–221.
[77] G. Constantinides and F. J. Ulm. “The effect of two types of C-S-H on the elasticity of cement-based materials: Results from nanoindentation and micromechanical modeling”. In: *Cement and Concrete Research* 34.1 (2004), pp. 67–80.

[78] A. B. Jordan, P. H. Stauffer, D. Harp, J. W. Carey, and R. J. Pawar. “A response surface model to predict CO_2 and brine leakage along cemented wellboreS”. In: *International Journal of Greenhouse Gas Control* 33 (2015), pp. 27–39.

Appendix A

Scripts

A.1 $CaCO_3$ precipitation in the cylindrical cavity

```
for (t=1; t<104; t++){ //t represents time
//Open images and remove surrounding regions:
  for (i=1; i<6; i++){
    start_nr = i*100 + 1;
    run("Image Sequence...", "open=D:images.tif number=100 starting='' +
    start_nr + '' sort");
    rename(i);
    open("D:ROI_'' + i + ''.roi");
    run("Clear Outside", "stack");
    }
  run("Image Sequence...", "open=D:images.tif number=43 starting=494 sort"
    );
  rename("6");
  open("D:ROI_6.roi");
  run("Clear Outside", "stack");
  run("Concatenate...", "  title=[Concatenated Stacks] image1=1 image2=2
    image3=3 image4=4 image5=5 image6=6");
  //Segmentation by intensity thresholding (16-bit images are used for
    this script):
  setThreshold(17000, 65550);
  run("Convert to Mask", "background=Dark");
  //Remove small objects and save statistics:
  run("3D Objects Counter", "threshold=128 slice=268 min.=65 max.=3466848
    objects statistics summary");
  selectWindow("Statistics");
  saveAs("Results", "statistics_t" + t + ".txt");
  selectWindow("Objects map of Concatenated Stacks");
  setMinAndMax(0, 1);
  run("Apply LUT", "stack");
  run("Convert to Mask", "background=Dark");
  //Save images:
```

```
27   run("Image Sequence... ", "format=TIFF name=image" + t +" save=D:\\image
       .tif");
28 }
29 }
```

Listing A.1: *ImageJ* script for segmentation of calcium carbonate in the CO_2 leakage pathway.

A.2 Reacted cement

```
1  for(t=1; t<104; t++){ // t is the time variable
2  //Open and crop image stack:
3    run("Image Sequence...", "open=D:/images''+t+''.tif number=597 sort");
4    open("D:\\ROI.roi");
5    run("Crop");
6    //Image pre-processing:
7    run("Morphological Filters (3D)", "operation=Dilation element=Cube x-
       radius=2 y-radius=2 z-radius=2");
8    run("Gaussian Blur 3D...", "x=5 y=5 z=5");
9    //Image segmentation:
10   run("Connected Threshold Grower ...", "x=340 y=347 z=26 min=85 max=107")
       ;
11   open("D:/ROI_general.roi");
12   run("Clear Outside", "stack");
13   //Split stack into substacks and remove voxels outside regions of
       interest:
14   run("Duplicate...", "title=First_Part duplicate range=1-92");
15   selectWindow("Region");
16   run("Duplicate...", "title=Second_Part duplicate range=93-483");
17   selectWindow("Region");
18   run("Duplicate...", "title=Third_Part duplicate range=484-518");
19   selectWindow("Region");
20   run("Duplicate...", "title=Fourth_Part duplicate range=519-597");
21   selectWindow("Second_Part");
22   open("D:/ROI_1.roi");
23   run("Clear Outside", "stack");
24   selectWindow("Third_Part");
25   open("D:/ROI_2.roi");
26   run("Clear Outside", "stack");
27     //Merge substacks:
28   run("Concatenate...", "  title=New_Region image1=First_Part image2=
       Second_Part image3=Third_Part image4=Fourth_Part image5=[-- None --]")
       ;
29   //Image post-processing:
30   run("Morphological Filters (3D)", "operation=Dilation element=Cube x-
       radius=2 y-radius=2 z-radius=2");
31   selectWindow("New_Region-Dilation");
32   //Remove the voxels corresponding to the cylindrical cavity:
33   run("Image Sequence...", "open=D:/hole.tif sort");
34   imageCalculator("Subtract create stack", "reacted","hole'');
35   //Save images:
36   run("Image Sequence... ", "format=TIFF name=image" + t +" save=D:\\image
       .tif");
37   run("Invert", "stack");
38   //Voxel count:
39   run("Voxel Counter");
```

```
  saveAs("Results", "Statistics.txt");
}
```

Listing A.2: *ImageJ* script for segmentation of reacted cement in the cement sample.

```
rolling = 0; //Parameter used for the subtract background algorithm.
for(t=1; t<104; t++){
  Open images and remove cement outside the region of interest:
  run("Image Sequence...", "open=D:/images''+t+''.tif number=361 starting
    =150 sort");
  open("D:/ROI.roi");
  run("Crop");
  run("Duplicate...", "duplicate");
  //Image pre-processing:
  run("Kuwahara Filter", "sampling=5 stack");
  run("Median 3D...", "x=2 y=2 z=2");
  run("Unsharp Mask...", "radius=50 mask=0.85 stack");
  run("Kuwahara Filter", "sampling=5 stack");
  run("Median 3D...", "x=2 y=2 z=2");
  run("Morphological Filters (3D)", "operation=Opening element=Cube x-
    radius=2 y-radius=2 z-radius=3");
  //Determine the radius of the ''rolling ball'' used in the subtract
    background operation for each t.
  if(t<3){
    rolling = 8;
    }
  else if(t>2 && t<29){
    rolling = 10;
    }
  else if (t>28 && t<49){
    rolling = 20;
    }
  else if (t>48 && t<60){
    rolling = 25;
    }
  else if (t>59 && t<104){
    rolling = 30;
    }
  run("Subtract Background...", "rolling=" + rolling + " sliding stack");
  run("Median 3D...", "x=2 y=2 z=2");
  //Image segmentation by simple linkage region-growing:
  if(t>50){
    run("Connected Threshold Grower ...", "x=175 y=159 z=193 min=55 max
    =255");}
  else{
    run("Connected Threshold Grower ...", "x=175 y=198 z=66 min=55 max=255
    ");}
  //Image post-processing:
  selectWindow("Region");
  run("Morphological Filters (3D)", "operation=Dilation element=Cube x-
    radius=1 y-radius=1 z-radius=2");
  run("Gaussian Blur 3D...", "x=2 y=2 z=2");
  run("Morphological Filters (3D)", "operation=Dilation element=Cube x-
    radius=1 y-radius=1 z-radius=2");
  setThreshold(65, 255);
  run("Convert to Mask", "background=Dark");
```

```
45   run("Fill Holes", "stack");
46   run("Morphological Filters (3D)", "operation=Erosion element=Cube x-
       radius=2 y-radius=2 z-radius=2");
47   run("Morphological Filters (3D)", "operation=Erosion element=Cube x-
       radius=2 y-radius=2 z-radius=3");
48   //Remove the voxels corresponding to the cylindrical cavity:
49   run("Image Sequence...", "open=D:/hole.tif sort");
50   imageCalculator("Subtract create stack", "Region-Dilation-Dilation-
       Erosion","hole'');
51   //Voxel count:
52   selectWindow("Result of Region-Dilation-Dilation-Erosion");
53   run("Voxel Counter");
54   saveAs("Results", "D:/statistics.txt");
55   //Save segmented images:
56   run("Image Sequence... ", "format=TIFF name=reacted_cement" + t +"_ save
       =D:/images.tif");
57 }
```

Listing A.3: *ImageJ* script for segmentation of reacted cement near the cylindrical cavity.

```
1  for(t=1; t<104; t++){
2    //Open images and remove cement outside the region of interest:
3    run("Image Sequence...", "open=D:/images_t" + t + ".tif number=361
       starting=150 sort");
4    open("D:ROI.roi");
5    run("Crop");
6    //Image pre-processing for segmentation of the porous zone:
7    run("Minimum 3D...", "x=1 y=1 z=2"); // A morphological erosion filter.
8    run("Median 3D...", "x=2 y=2 z=2");
9    run("Unsharp Mask...", "radius=90 mask=0.90 stack");
10   run("Gaussian Blur 3D...", "x=2 y=2 z=2");
11   run("Median 3D...", "x=2 y=2 z=2");
12   //Image segmentation:
13   run("Statistical Region Merging", "q=25 showaverages 3d");
14   run("8-bit"); //The resulting images of the ''Statistical Region Merging
       '' algorithm are 32-bit.
15   //Keep only darkest regions of the output images of the ''Statistical
       Region Merging'' algorithm.
16   setThreshold(0, 170);
17   run("Convert to Mask", "background=Dark");
18   run("Invert", "stack");
19   //Image post-processing:
20   //First create a ROI and remove voxels outside the ROI. The ROI depends
       on t as the porous zone grows as a function of time.
21   if (t<36){
22     makeOval(86, 154, 80, 75);
23     run("Clear Outside", "stack");}
24   else if (t>35 && t<41){
25     makeOval(83, 151, 86, 84);
26     run("Clear Outside", "stack");}
27   else if (t>40 && t<50){
28     makeOval(74, 139, 102, 103);
29     run("Clear Outside", "stack");}
30   else if (t>49 && t<60){
31     makeOval(64, 130, 126, 122);
```

```
    run("Clear Outside", "stack");}
  else if (t>59 && t<80){
    makeOval(60, 131, 131, 125);
    run("Clear Outside", "stack");}
  else if (t>79 && t<90){
    makeOval(57, 119, 139, 148);
    run("Clear Outside", "stack");}
  else if (t>89 && t<104){
    makeOval(53, 111, 151, 151);
    run("Clear Outside", "stack");}
  run("Keep Largest Region");
  run("Morphological Filters (3D)", "operation=Closing element=Cube x-
    radius=1 y-radius=1 z-radius=1");
  run("Invert", "stack");
  run("Analyze Particles...", "size=0-2000 show=Masks stack");
  run("Invert", "stack");
  imageCalculator("Add create stack", "Result-largest-Closing","Mask of
    Result-largest-Closing");
  //Remove the voxels corresponding to the cylindrical cavity:
  run("Image Sequence...", "open=D:/hole.tif sort");
  imageCalculator("Subtract create stack", "porous","hole'');
  //Save segmented images:
  run("Image Sequence... ", "format=TIFF name=porous_zone" + t +"_ save=D
    :/images" + t + ".tif");
  //Voxel count:
  run("Voxel Counter");
  saveAs("Results", "D:statistics_t" + t+ ".txt");
}
```

Listing A.4: *ImageJ* script for segmentation of the porous zone near the cylindrical cavity.

A.3 Mechanical deformation of the sample

```
for (t=1; t <104; t++){
  //Open image sequence:
  run("Image Sequence...", "open=D:\\images_t" + t + ".tif number=486
    starting=94 sort");
  //Image pre-processing:
  open("D:/ROI.roi");
  run("Crop");
  run("Unsharp Mask...", "radius=100 mask=0.80 stack");
  run("Subtract Background...", "rolling=30 stack");
  run("Morphological Filters (3D)", "operation=Closing element=Cube x-
    radius=2 y-radius=2 z-radius=2");
  //Image segmentation:
  setThreshold(108, 255);
  run("Convert to Mask", "background=Dark");
  //Image post-processing:
  run("Fill Holes", "stack");
  run("Remove Outliers...", "radius=2 threshold=50 which=Dark stack");
  run("Keep Largest Region");
  run("Morphological Filters (3D)", "operation=Closing element=Cube x-
    radius=2 y-radius=2 z-radius=2");
  //Remove end slices to reduce end artifacts:
  run("Duplicate...", "duplicate range=10-543");
```

```
20   //Remove the voxels corresponding to the cylindrical cavity:
21   run("Image Sequence...", "open=D:/hole.tif sort");
22   imageCalculator("Subtract create stack", "cylinder","hole'');
23   //Voxel count:
24   run("Voxel Counter");
25   saveAs("Results", "D:/statistics_" + t + ".txt");
26 }
```

Listing A.5: *ImageJ* script for segmentation of the cement cylinder.

```
1  for(t=1; t<104; t++){
2    //Open images:
3    run("Image Sequence...", "open=D:/images_t" + t+ ".tif number=361
       starting=150 sort");
4    //Image pre-processing:
5    open("D:/ROI.roi");
6    run("Crop");
7    run("Morphological Filters (3D)", "operation=Closing element=Cube x-
       radius=2 y-radius=2 z-radius=2");
8    run("Median 3D...", "x=2 y=2 z=2");
9    run("Mean 3D...", "x=2 y=2 z=2");
10   //Image segmentation:
11   setThreshold(68, 90);
12   run("Convert to Mask", "background=Dark");
13   //Image post-processing:
14   run("Invert", "stack");
15   makeOval(87, 153, 76, 70);
16   run("Clear Outside", "stack");
17   run("Morphological Filters (3D)", "operation=Closing element=Cube x-
       radius=1 y-radius=1 z-radius=1");
18   run("Keep Largest Region");
19   run("Remove Outliers...", "radius=15 threshold=50 which=Dark stack");
20   run("Morphological Filters (3D)", "operation=Closing element=Cube x-
       radius=2 y-radius=2 z-radius=2");
21   //Voxel count:
22   run("Voxel Counter");
23   saveAs("Results", "D:/statistics_t" + t + ".txt");
24   //Save images:
25   run("Image Sequence... ", "format=TIFF name=cavity" + t +"_ save=D:/
       images_t''+t+''.tif");
26 }
```

Listing A.6: *ImageJ* script for segmentation of the cylindrical cavity.